der Bundeswehr
Universität München

UNIVERSITÄT DER BUNDESWEHR MÜNCHEN
Fakultät für Elektrotechnik und Informationstechnik

Development of innovative thermal plasma and particle diagnostics

Benjamin-Leon Bachmann

Vorsitzender des Promotionsausschusses:	Prof. Dr.-Ing. Klaus Landes, Universität der Bundeswehr München
1. Berichterstatter:	Prof. Dr.-Ing. Jochen Schein, Universität der Bundeswehr München
2. Berichterstatter:	Prof. Javad Mostaghimi Ph.D., University of Toronto

Tag der Prüfung: 20.09.2013

Mit der Promotion erlangter akademischer Grad:
Doktor-Ingenieur
(Dr.-Ing.)

Neubiberg, den 24.09.2013

Acknowledgements

First and foremost I would like to thank my advisor Jochen Schein for giving me the chance to work in his institute. His unwavering support and constant demand encouraged me to pursue and achieve my research goals. I appreciate his intellectual fearlessness and his tireless enthusiasm which highly contributed to my scientific development. It was a real pleasure and great experience to work with Jochen.

I would like to express my gratitude to Klaus Landes who was reading my very first lecture at University. I remember this event as if it was yesterday and since then he was an example for me as a gifted educator with an unshakable scientific integrity, a passion for science and genuine concern for others. Our discussions during my time as a postgraduate were always inspiring.

I am especially indebted to José-Luis Marqués-López who spent a huge amount of time and energy during many fruitful discussions we had. He helped me to break new ground by teaching me new theoretical concepts and how to apply my mathematical skills to solve physical problems. His commitment, encouragement and critical insight propelled my searches and analyses.

Further, I would like to thank Jochen Zierhut, Stephan Zimmermann and Günter Forster who were sparkling sources of ideas for the solution of many technical challenges. They were always encouraging and their guidance helped me in the pursuit of my research goals.

I wish to thank my colleagues Marina Kauffeldt, Mathias Pietzka, Stefan Kirner, Erwan Siewert and Karsten Hartz-Behrendt as well as Ruslan Kozakov and Gregor Gött from the Leibniz Institute for Plasma Science and Technology, Greifswald for the numerous helpful discussions and wish them the best for their future careers.

I owe a special thanks to the whole team of non-scientific staff, Walter Wagner, Günter Haderer, Hermann Karl, Alexander Mai, Martin Goretzki and especially Ulrich Bayrle who provided me with precisely manufactured mechanical components, refreshing discussions and lots of chocolates.

I am happy to thank all undergraduate students who entrusted me with the supervision of their Bachelor and Master theses. I would not want to miss the experience to lead a small team of highly motivated and diligent students in their onset of a scientific career. Their constructive questions helped me to always keep in mind that scientific merit is a result of human curiosity.

The time I spent with my colleagues and advisors was made most enjoyable by the many social activities I could participate in, be it sailing in Italy, skiing in the Alps or just spending time together and talking about everything and anything. I thank them a lot for making me feel part of something great.

Finally I would like to thank my family for their never ending love and support.

Statement of Originality

I, Benjamin-Leon Bachmann, hereby certify that this doctoral thesis is my own work and any work by others is appropriately cited and indicated. All contents of this thesis which have been pre-published in partial fulfillment of the requirements for the doctoral degree (Dr.-Ing.) and with approval of the Faculty of Electrical Engineering of the University of the German Federal Armed Forces have been indicated with quotation marks (‘...’) followed by the particular citation in brackets ([...]). The utilization and publication of pre-published material in this thesis is specifically granted where necessary by copyright agreements which have been made with the particular publisher.

Selbstständigkeitserklärung

Hiermit versichere ich, Benjamin-Leon Bachmann, die vorliegende Arbeit selbstständig und nur unter Verwendung der angegebenen Quellen und Hilfsmittel angefertigt zu haben. Alle Inhalte dieser Arbeit, welche zur Erfüllung der Voraussetzungen zur Erhaltung des Doktortitels (Dr.-Ing.) und durch Genehmigung der Fakultät für Elektrotechnik und Informationstechnit der Universität der Bundeswehr vorveröffentlicht wurden, sind im folgenden Text mit Apostrophen (‘...’) gekennzeichnet auf welche die jeweilige Quelle in Klammern ([...]) folgt. Die Verwendung und Veröffentlichung von vorveröffentlichtem Material in dieser Arbeit ist, wo notwendig, durch das jeweilige *copyright agreement* mit dem entsprechenden Verlag ausdrücklich genehmigt.

List of publications

The following publications arose from work which has been done in partial fulfillment of the requirements for the doctoral degree (Dr.-Ing.) and have been pre-published to this dissertation with approval of the Faculty of Electrical Engineering of the University of the German Federal Armed Forces.

Peer-reviewed:

1. Bachmann B, Kozakov R, Gött G et al.: High-speed three-dimensional plasma temperature determination of axially symmetric free burning arcs, Journal of Physics D: Applied Physics 46, 125203, 2013
2. Bachmann B, Siewert E and Schein J: In situ droplet surface tension and viscosity measurements in gas metal arc welding. Journal of Physics D: Applied Physics 45, 175202, 2012

Patent:

3. Bachmann B, Heinrich P, Krömmer W and Zierhut J: Method for determining e.g. porosity of thermally sprayed heat-insulating layers applied to substrate, involves generating pressure wave at layer and/or substrate surfaces on heat-insulating layer, and detecting portion of pressure wave, EP2495545-A2, DE102011005074-A1, Linde AG

Book contributions:

4. Bachmann B, Siewert E, Schein J: Chapter 2: Development of innovative diagnostics for characterization of material transfer and plasma properties in tungsten inert gas welding (TIG) and gas metal arc welding (GMAW), pp. 18-33, appeared in 'Arc welding - Physics and capabilities of gas metal arc welding' DVS Media, ISBN: 3-87155-273-9, 2012
5. Bachmann B, Marques J-L, Schein J: Chapter 2: Innovative Diagnostik zur Analyse des Werkstoffübergangs im MSG-Schweißprozess, pp. 13-17, appeared in 'Lichtbogenschweißen - Physik und Werkzeug' (in German), Volume 2, ISBN: 978-3-941681-09-5, 2010
6. Bachmann B, Marques J-L, Schein J: Chapter 2: Innovative Diagnostik zur Analyse des Werkstoffübergangs im MSG-Schweißprozess, pp. 11-14, appeared in 'Lichtbogenschweißen - Physik und Werkzeug' (in German), Volume 1, ISBN: 978-3-941681-02-6, 2009

Conference proceedings:

7. Bachmann B and Schein J: Innovative diagnostics for transient plasma processes, NIF and JFL user group meeting, February 10-13, 2013, Livermore, CA, USA
8. Bachmann B, Kozakov R, Gött G et al.: Evaluation of optical methods for the diagnostic of free burning arcs, 19th International Conference on Gas Discharges and Their Applications, GD 2012, September 02 - 07, 2012, Beijing, China

9. Bachmann B, Marques J-L, Schein J and Richter M: Three-dimensional tomographic reconstruction of the electric current density distribution within a transferred plasma arc, 37th IEEE International Conference on Plasma Science, June 20-24, 2010, Norfolk, VA, USA

10. Bachmann B, Siewert E, Schein J: Surface-controlled droplet oscillations in gas metal arc welding, 12th European Plasma Conference, June 24-29, 2012, Bologna, Italy

11. Bachmann B and Schein J: Innovative diagnostics for transient plasma processes, DPG Frühjahrstagung, February 25 - March 01, 2013, Jena, Germany

12. Bachmann B, Marques J-L, Siewert E et al.: Stromdichtemessungen im Lichtbogenschweißprozess, DVS-record 275, ISBN: 978-3-87155-267-0, pp. 527-530, DVS Congress, September 26 - 29, 2011, Hamburg, Germany

13. Siewert E, Bachmann B, Marques, J.-L. et al.: Experimentelle Erkenntnisse zum Werkstoffübergang, DVS-record 275, ISBN: 978-3-87155-267-0, pp. 531-537 DVS Congress, September 26 - 29, 2011, Hamburg, Germany

Abstract

Three original plasma diagnostic systems have been developed to investigate transient three-dimensional plasma processes with high spatial and temporal resolution. The developed diagnostics have been analyzed and tested by increasing the complexity from a stationary free burning Argon arc to a dc pulsed process and finally to a transient gas metal arc including droplet transfer through the plasma. The transient plasma parameters that have been determined include three-dimensional axially symmetric plasma densities (n_e, n_A, n_{A+}, n_{A++}), electron temperatures (T_e), electrical conductivities (σ_{el}), magnetic flux densities (B) and current densities (j_{el}). In the case of a droplet transfer through an arc consisting of an Iron/Argon plasma, the droplet density (ρ_{droplet}), surface tension (σ_{droplet}), viscosity (η_{droplet}) and temperature (T_{droplet}) have been determined.

The first diagnostic system which has been developed accomplishes high-speed three-dimensional measurements of plasma parameters and is based on an experimental setup utilizing interference filters with narrow spectral bands of $487.5 - 488.5\,\text{nm}$ and $689 - 699\,\text{nm}$. With a set of mirrors these spectral bands are imaged simultaneously on a single chip of a high-speed camera providing perfect temporal synchronization. The development of two different Abel inversion methods allows for reconstruction of the original distribution of emission coefficients. The assumed axial symmetry needed for Abel inversion was validated with a modified setup of mirrors which images the arc from two orthogonal directions providing a three-dimensional image. Assuming a local thermodynamic equilibrium and applying the Saha equation, the ideal gas law, the quasineutral gas condition and the NIST compilation of spectral lines, plasma composition calculations have been performed. Additionally, emission coefficients from Bremsstrahlung, emission due to recombination and line emission have been calculated and temperature dependent emission spectra have been simulated. By comparison of measured and simulated ratios of emission coefficients from the two spectral bands the plasma temperature and related parameters have been derived. Stationary free burning Argon arcs have been analyzed at dc currents of 100, 125, 150 and 200 A. Plasma temperatures ranging up to 20000 K have been found in the hot cathode region. The stationary measurements have been tested at selected measurement positions by different techniques utilizing a high-resolution spectrometer. These evaluations make use of a single line and a line ratio method, the Fowler-Milne method and the evaluation of the quadratic Stark broadening of the 696.54 nm Argon atom line. The obtained plasma temperatures agree very well throughout the performed measurements. Moreover, a dc pulsed process of a free burning Argon arc was used to determine three-dimensional transient plasma temperatures with a frame rate of 33000 frames per second. Here the calculated isothermals show the quantitative electrode attachment of an arc and the sensitivity of the measurement.

The second diagnostic developed allows the determination of the three-dimensional current density distribution of an axially symmetric free burning Argon arc in case of a Gaussian distribution of the axial component of the current density. This has been achieved by measuring the magnetic flux density in the outer plasma sheaths. The measurement volume was subdivided into several cross sections which contain different parts of the overall current. Measuring the magnetic flux density along the tangent vector of these cross sections allows the experimental determination of the included current using Ampere's

law. With the assumption of a Gaussian current density distribution the characteristic spatial expansion of the arc was calculated and thus spatial distributions of current densities in axial and radial direction were derived. Current density distributions have been measured for 20 mm and 8 mm long arcs with overall currents of 50, 100, 125 and 150 A. Current densities in axial and radial direction of the 20 mm long arc were determined up to $6 \times 10^5\,\mathrm{A/m^2}$ and $2 \times 10^4\,\mathrm{A/m^2}$, respectively. Axial current densities in the center of the 8 mm long arcs were in the range of $1.5 \times 10^6\,\mathrm{A/m^2}$ to $3.8 \times 10^6\,\mathrm{A/m^2}$ for applied currents of 100 A to 150 A. The axial symmetry of the arcs was validated and results for current densities were compared to results from electrical conductivities obtained with the first diagnostic. An outlook to reconstruct arbitrary current density distributions is given. Furthermore it is experimentally shown how a change of the current density in a cathode of a gas metal arc is affecting the surrounding magnetic flux density. These measurements show the potential to obtain information about the current density in a gas metal arc by magnetic flux density measurements.

Finally an optical diagnostic is introduced which allows for *in situ* measurements of thermophysical properties and temperatures of droplets in gas metal arcs. Surface tension, viscosity, density and temperature have been determined with a drop oscillation technique. The droplet oscillations were recorded during the material transfer through a pulsed Iron/Argon arc. In order to measure the oscillation frequency which was in the low kHz range a high-speed camera recording 30000 frames per second was employed. An image processing algorithm has been developed to extract the edge contour and to calculate oscillation frequencies and damping rates along different droplet dimensions. By including the effect of temperature on the droplet density it was possible to determine values of surface tension. The obtained accuracy of about 1% enables to investigate metals for which density is strongly depending on temperature. Pure liquid iron droplets detaching from a melting wire electrode with a diameter of 1.2 mm were analyzed in a pulsed gas metal arc with a base current of 100 A and pulse currents in the range of $500 - 600$ A. The surface tension of a sample droplet was $1.83 \pm 0.02\,\mathrm{N\,m^{-1}}$. The viscosity of this sample droplet was 2.9 ± 0.3 mPa s. Corresponding droplet temperature and density were 2040 ± 50 K and $6830 \pm 50\,\mathrm{kg\,m^{-3}}$, respectively.

Contents

Abstract i

1 Introduction 1

2 Description of plasma sources used 3

3 High-speed three-dimensional optical plasma temperature determination 5
3.1 Introduction . . . 5
3.2 Experimental approach enabling high-speed spatially resolved optical emission spectroscopy . . . 7
3.2.1 Description of high-speed setup . . . 7
3.2.2 Description of setup employing high-resolution spectrometer . . . 8
3.3 Theory of plasma composition calculations and spectral emission coefficients 9
3.3.1 The Saha equation . . . 9
3.3.2 Solving the Saha equation for monoatomic plasmas in thermodynamic equilibrium . . . 11
3.3.3 Calculation of emission coefficients . . . 14
3.4 Three-dimensional reconstruction of axially symmetric intensity distributions employing inverse Abel transformation . . . 16
3.4.1 Analytical Abel-inversion procedure . . . 17
3.4.2 Alternative Abel inversion algorithm allowing subsequent quantitative comparison of influences on temperature results . . . 17
3.5 Methods for evaluation of emission coefficients . . . 19
3.5.1 Method of ratios of emission coefficients . . . 19
3.5.2 Evaluation of single discrete lines by calibration with a tungsten ribbon lamp . . . 20
3.5.3 Evaluation employing Fowler-Milne method . . . 20
3.5.4 Evaluation of the 696.54 nm Ar-atom line width by quadratic Stark broadening . . . 22
3.6 Results of plasma temperature measurements and comparison with classical optical emission spectroscopy . . . 22
3.7 Results of related plasma parameters and transient plasma processes . . . 26
3.8 Error sources, measurement uncertainties and limits of applicability . . . 27
3.8.1 Random errors . . . 28
3.8.2 LTE consideration . . . 29
3.8.3 Measurement of optical depth . . . 30
3.8.4 Measurement of axial symmetry . . . 31
3.8.5 Errors induced by Abel-inversion . . . 32
3.8.6 Influence of line and continuum emission on overall emission and accuracies of utilized transition probabilities . . . 35
3.8.7 Error sources due to the design of the experimental setups . . . 35
3.8.8 Error summary . . . 36

4 A diagnostic to measure three-dimensional current density distributions in axially symmetric free burning arcs by means of Hall effect devices 39

4.1 Introduction . . . 39
4.2 A general and simplified approach for the reconstruction of current density distributions . . . 40
4.2.1 General approach for the reconstruction of current density distributions . . . 40
4.2.2 Simplified approach for the reconstruction of axially symmetric current density distributions . . . 42
4.3 Experimental setups for measuring magnetic flux density distributions . . . 45
4.3.1 Parameters of free burning arcs . . . 45
4.3.2 Magnetic flux density measurements and data acquisition employing FPGA based hardware real time evaluation . . . 45
4.4 Results of current density measurements employing the simplified reconstruction approach . . . 46
4.4.1 Results for 20 mm arc: magnetic flux densities and three-dimensional current density distribution . . . 46
4.4.2 Results for 8 mm arcs: Three-dimensional current density distributions 47
4.5 Comparison with optical measurements . . . 50
4.6 Discussion of a general method for arbitrary non-intrusive current density measurements utilizing Hall probes . . . 50
4.7 From current density measurements in free burning arcs to possible diagnostics of current phenomena in gas metal arcs . . . 52

5 An *in situ* diagnostic to measure thermophysical droplet properties and droplet temperature in gas metal arcs 62
5.1 Introduction . . . 62
5.2 Experimental setup to visualize droplets in a gas metal arc . . . 66
5.3 Image processing, data evaluation and determination of droplet mass for high temperature melts . . . 67
5.3.1 Image processing and data evaluation by thresholding, morphological erosion and dilation and conversion to a binary image . . . 67
5.3.2 Determination of droplet mass and density . . . 67
5.4 Time- and frequency study of free falling droplets and results of thermophysical droplet parameters and droplet temperature . . . 70
5.5 Sources of error and analysis of uncertainties . . . 75

6 Conclusion and Outlook 77

A Estimation of electrical conductivity 81

B Error propagation in non-linear least squares 83

Bibliography 85

Chapter 1

Introduction

Plasma physics established as a main research field in the last century. The development of this research topic profited, like other fields of physics, from the interaction between theory and experiment. On the one hand, the theory is required to deliver results by calculation and modeling of realistic and applied plasma processes. To accomplish this it is necessary to measure plasma parameters in order to prove the theories which describe the phenomena at work. On the other hand, the measurement of plasma parameters which the discipline *plasma diagnostics* is devoted to, is based on assumptions which are made in accordance to the theory present at this time. Thus many diagnostics have been developed during the establishment of plasma theory.

In this thesis three different diagnostic systems will be described aimed at the characterization of three-dimensional transient plasma processes. A detailed overview of the state-of-the-art in plasma diagnostics will be given in the introduction of each part of this thesis (see section 3.1, 4.1 and 5.1). Therein the research is described which has been done before and which is relevant to the diagnostic systems presented in this thesis.

Nowadays commercial applications of plasmas make use of transient processes for which a lack of theory and understanding is apparent. Those plasmas are used for example in welding, cutting and plasma spraying for the automobile industry, aerospace and construction engineering of e.g. cars, airplanes and buildings [51]. Other fields include lamps and displays, plasma medicine, ion thrusters, plasma enhanced chemistry, fusion energy research and semiconductor fabrication [38]. The partially unmet need to understand the processes occurring in those applications is a result from the requirement to further develop and optimize these processes. One example where the need to understand the physical phenomena at work is evident are arc plasmas containing molten materials (gas metal arcs) which can be found in applications like plasma spraying or gas metal arc welding [91]. While the latter is one of the most applied processes in today's industrial welding, (extensively applied in the sheet metal industry and thus car production) it comprises complex plasma compositions of multi-component gases including metal vapors and material transfer of liquid metals through the plasma [91]. From a diagnostics point of view a further challenge of this and similar processes is the occurrence of transient phenomena caused by e.g. pulsed currents. Since most of the available diagnostic techniques are limited with regard to temporal resolution, it is difficult to analyze transient processes. Indeed, this circumstance is becoming more severe since industrial transient processes become even faster due to ever improving control electronics [12]. Another challenge for existing diagnostics which are for example based on time averaged measurements is that arcs in general are not stationary on a small time scale. Additional phenomena may be involved, like droplets which can be found in gas metal arc welding or wire arc spraying, which make the process more difficult to analyze. Such plasmas are an example where existing plasma diagnostics are limited due to the assumptions which the diagnostic methods are based on (e.g. symmetries of arcs and stationarity of plasma processes).

In this thesis an attempt is made to improve available diagnostics and to use these to an-

alyze multi-dimensional transient plasmas as well as liquid particles which move through plasmas. Three diagnostic systems have been developed to accomplish this starting from a diagnostic based on optical emission spectroscopy which allows to investigate transient three-dimensional axially symmetric plasmas (part 1, chapter 3). This system is based on an experimental setup which analyzes two spectral bands utilizing interference filters and imaging of the plasma through these filters on a single camera chip. Thus a simultaneous acquisition of spatially resolved spectral information with a high-speed camera is made. Different methods of evaluation have been developed and applied on experimental data acquired from transient free burning arcs yielding results for high-speed spatially resolved plasma densities, temperatures and conductivities.

A diagnostic to measure current densities and distributions of currents has been developed and applied to free burning Argon arcs. A method to extend this tool to gas metal arcs will be discussed (part 2, chapter 4). The main idea of this diagnostic is to measure the magnetic flux density of a current carrying plasma and then to reconstruct information about the distribution of the current. This approach allows for the spatially resolved measurement of current densities in free burning arcs as well as to gather information about the distribution of the current in the cathode of a gas metal arc. The results of current densities obtained from the free burning arc will be compared to electrical conductivities which have been determined by other methods. The agreement of results obtained allows for an independent validation of the plasma diagnostic tools which have been introduced.

As was mentioned before, gas metal arcs contain liquid metals which are transferred through the plasma. Hence a diagnostic was established which allows for *in situ* measurements of thermophysical properties of these liquid metals. It is based on the high-speed optical measurement of intrinsic droplet oscillations which arise during the material transfer. Thus an image processing algorithm has been developed and frequency analyses have been carried out yielding droplet densities, surface tension, viscosity and temperature.

These diagnostics may be used for various technical plasma systems like welding, cutting or plasma spraying as long as the assumptions these diagnostics are based on are met.

Chapter 2

Description of plasma sources used

The free burning arcs that have been analyzed in this work make use of a tapered tungsten tip which is used as a cathode (–) and surrounded by a nozzle through which an Argon flow is directed. A copper plate was used as an anode (+). Both electrodes are water cooled and thus not melting. The arcs were driven by DC and transient currents. The experimental parameters of the setup can be found in Table 2.1.

The gas metal arcs that have been investigated in this thesis are created by melting wire electrodes which are continuously supplied through a nozzle. The wire was set as anode (+) in order to increase the melting rate due to the additional energy brought by electrons which results from the work function of the electrode material [91]. The arc was ignited by contact between the wire electrode and a metal sheet which was set as cathode (–). Pulsed currents created with an OTC CPDACR-200 power source are used to detach droplets from the wire electrode making use of the magnetic pinch effect. While traveling through the plasma, the droplets perform damped oscillations until they reach the cathode. Different configurations of the cathode geometry have been used. Either the metal sheet was continuously moved on a linear translation stage or a perforated cathode was employed through which the droplets can fall. An overview of the employed parameters can be found in Table 2.1.

arc parameters	free burning Ar arcs	Al/Ar arcs	Fe/Ar arcs
Gas flow	Ar, 12 slpm	Ar, 12 slpm	Ar, 12 slpm
Inner nozzle diameter	11 mm	14 mm	14 mm
Cathode stick-out	5 mm	–	–
Anode stick-out	–	up to 5 mm	up to 5 mm
Arc length	8 mm	–	–
Distance nozzle-cathode	13 mm	10 mm	10 mm
Wire diameter	–	1.2 mm	1.2 mm
Anode material	water-cooled Cu-plate	Al	Fe
Cathode diameter	4 mm	–	–
Cathode material	WL20 (ISO class)	Al	steel
Cathode point angle	45	–	–
DC currents	50, 100, 125, 150, 200 A	–	–
Base / Peak current	–	20 A / 220 A	100 A / 500 – 600 A
Pulse frequency	–	40 Hz	60 – 100 Hz
Base time	–	0.02 s	0.007 – 0.008 s

Table 2.1: Experimental parameters for free burning Argon arcs and gas metal arcs.

PART 1

Chapter 3

A non-intrusive diagnostic to determine plasma temperature, densities and conductivity of axially symmetric free burning arcs with a high temporal and spatial resolution

3.1 Introduction

'The determination of the local temperature distribution within a free burning arc is important in order to evaluate the thermal impact on the electrodes. Numerous techniques exist to determine local plasma temperature, like Thomson scattering or Langmuir probe measurements, but these techniques might influence the parameters being measured [41, 95]. Thus non-intrusive approaches are better suited to accomplish this goal. Optical emission spectroscopy (OES) is a widely accepted and commonly used tool in the analysis of thermal plasmas and plasmas in general. The measurements of temperature and particle density profiles by means of OES have a long history (see for example [9, 10]). A review of early applications for arc diagnostics can be found for example in [78] and for low temperature plasmas in [103]. Some of the methods described therein are applicable for arc plasmas. They are based on the assumption of local thermodynamic equilibrium (LTE) which allows the calculation of the temperature dependence of densities of plasma components (by the Saha equation - section 3.3.1) and thus the intensity of plasma radiation (see section 3.3.3).

In some cases when the temperature in arcs exceeds the value at which the atomic line, ion line or continuum has its maximal emission coefficient it is possible to determine the plasma temperature. The theoretical approach for this method was given in papers of Fowler and Milne [31, 32] for stellar atmospheres and adopted for electric arcs by Larenz [60]. It is often cited as Fowler-Milne method. The simplicity of this method accompanied with no necessity of an absolute calibration explains its wide use in diagnostics. This method was used for example for diagnostics of stationary and pulsed free burning arcs in [100, 63, 106]. However some assumptions made by the deduction of this method are not completely met in free burning Argon arcs as was shown in [30] where deviations of emitted radiation from LTE assumptions in the outer regions of arc were noted (see also section 3.8.2).

In other cases the absolute intensity of plasma radiation measured in a small spectral interval is compared with the calculated intensity to provide a value for temperature. This is known as classical OES technique and sometimes called 'absolute line' or 'single line' method. Usually a spectroscopic system with a sub-nm spectral resolution is used. Calibration of these absolute measurements are obtained by comparison of the plasma radiation intensity with that of a calibrated radiation source, for example a tungsten ribbon lamp [42]. In general this method allows the separation of line and continuum radiation and provides accurate results. The drawback is that only one-dimensional temperature profiles

can be determined. This is due to the imaging of the side-on position on one dimension of a camera chip and the evolution of the wavelengths on the second dimension of the camera chip. This limits the possibility of high-speed diagnostics for classical spectrometers to a one dimensional analysis. For two-dimensional profiles several single line measurements at different positions are necessary. In principle the single line method can also be evaluated with the high-speed diagnostics presented in this work (using interference filters), however it is less robust than the developed high-speed method (see e.g. section 3.8.2). An implementation of the 'single-line' method utilizing a tomographic approach can be found in [47].

Still another approach consists in measuring the relative intensity in lines or bands of plasma radiation (see for example [88]). This method is sometimes called 'two line' or 'Boltzmann' method. By an appropriate model the relation between two or more spectral bands as a function of temperature can be calculated. Comparing the measured relation with the calculated one, a temperature distribution is obtained. An advantage of this method is that even if a departure from 'single temperature LTE' to 'two temperature LTE' occurs this method is still able to yield correct values for the electron temperature if appropriate lines are selected for the evaluation (section 3.8.2). Here the difference between 'single temperature LTE' and 'two temperature LTE' is that in the latter case the temperature of electrons and the heavy species can be different, although a population of Energy levels according to a Boltzmann distribution and ionization equilibrium is present in both cases.

Due to the increase of highly dynamic plasma processes e.g. in welding, cutting and plasma spraying, the determination of transient plasma temperatures and related parameters like densities of atomic species or electrical conductivity gains importance. Thus pulsed electric currents are for example applied in gas metal arc welding to control the process of droplet formation. Another example would be the pulsed admixture of special gases which have positive effects on treated materials where a continuous addition of these partly expensive gases would be too costly. Hence diagnostics are needed which can be used to optimize these processes. In this thesis a technique that accomplishes these goals is presented and meets the demand for a non-intrusive, high-speed and three-dimensional plasma diagnostic, which is the adaption of the 'two line' method using high-speed camera imaging.

This method is validated using different spectroscopic techniques to compare the results during a stationary process. For simplicity a restriction to the free burning arc with pure Argon as shielding gas is made. The approach is organized as follows: Plasma temperature is derived by the comparison of the detected plasma radiation with a calculated plasma emission assuming optically thin plasma (see section 3.8.3) and a single local temperature for all plasma species. The spectral emission coefficient ε_λ is calculated for the spectral bands defined by the used filter characteristics, based on the emission of lines and continuum (section 3.3.3). Plasma radiation is subsequently measured by means of a high-speed camera for the two short spectral bands simultaneously at high speed and spatially reconstructed by an Abel inversion procedure. The ratio of local emission coefficients from the two spectral intervals measured with the filter based setup is compared to the calculated emission spectra and thereby correlated with temperature (Method 1, Table 3.1). In order to validate the results obtained by this technique, measurements are performed with a spectrometer (side on - 1D) using different methods: The first method employs the same evaluation procedure as performed with the camera based setup (see Method 2, Table

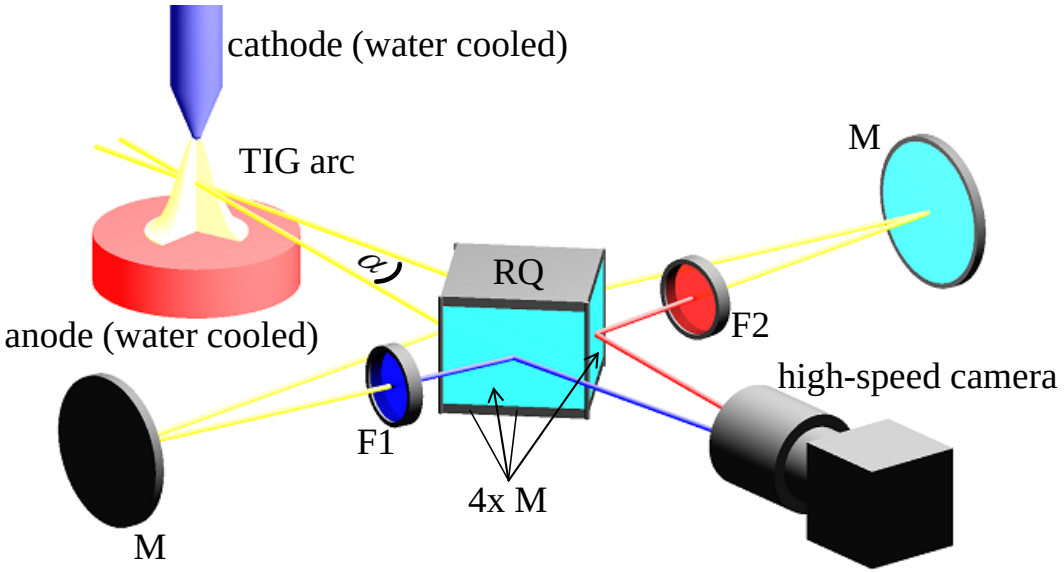

Figure 3.1: Experimental setup for high-speed three-dimensional determination of transient temperature profiles. (M: mirror, F1: filter: 488 nm, F2: filter: 694 nm, RQ: reflecting cube with 4 mirrors.)

3.1). The next method investigated is a single line method where the measured line emission coefficient is compared to the emission of a calibrated tungsten ribbon lamp (Method 3, Table 3.1). The third method is known as Fowler-Milne method (also known as normal temperature method) (Method 4, Table 3.1). The last method is based on the evaluation of the spectral broadening of the 696.54 nm Argon-atom line due to the quadratic Stark effect (Method 5, Table 3.1).' [4]

3.2 Experimental approach enabling high-speed spatially resolved optical emission spectroscopy

3.2.1 Description of high-speed setup

'A schematic drawing of the setup enabling non-intrusive high-speed three-dimensional measurements of thermophysical plasma parameters is shown in Figure 3.1. The main idea of this setup is to simultaneously image same plasma sections of different wavelength intervals of the plasma on a single camera chip. Hence plasma radiance, which is emitted from two paths separated by negligible small angle α is guided through the setup of mirrors and two narrow bandpass dichroic filters with appropriate center wavelengths and bandwidths before being imaged to the high-speed camera chip. The selected center wavelengths which have been employed for the analysis of Argon plasmas are 488 nm (left) and 694 nm (right) with a *full width at half maximum* (FWHM) of 1 nm and 10 nm, respectively. Thus through the blue wavelength window mainly Argon ion lines with continuum radiation is transmitted while mainly Argon atom lines and continuum radiation is transmitted through the red wavelength window. These center wavelengths have been chosen for analysis due to optical thickness measurements which were carried out and show that plasma generated with the described plasma source (see section 2) is optically thin at these two spectral windows (see section 3.8.3). The optical thin plasma is nec-

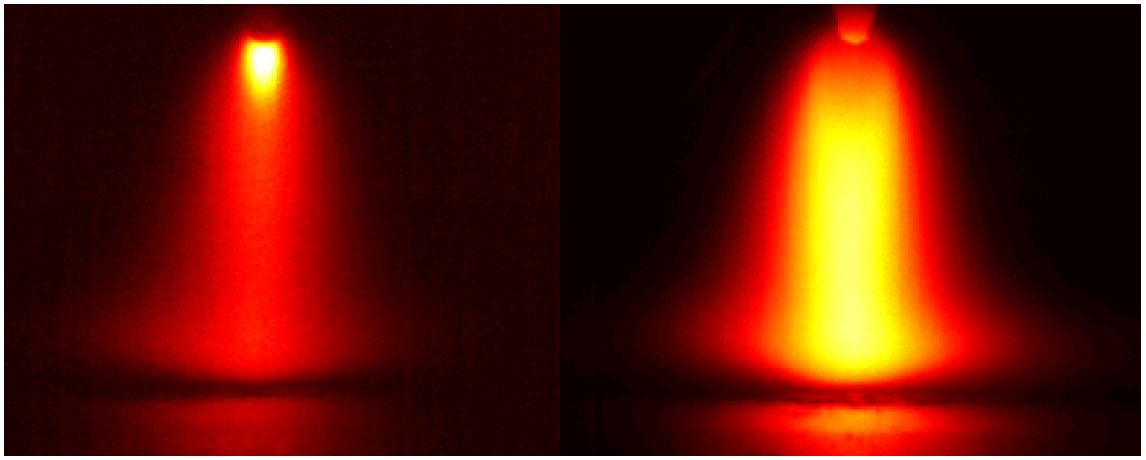

Figure 3.2: Plasma emission measured with setup from Figure 3.1 on a single camera chip. (The bottom part of the picture shows reflections from the anode.) Left: Plasma emission from 488 nm. Right: Plasma emission from 694 nm. (In order to approximate the appearance of the original 12 bit image, color conversion and tone mapping was applied before compression to 8 bit.)

essary in order to calculate the three-dimensional emission coefficients from the side-on measurements by the Abel inversion introduced in section 3.4. Each FWHM was selected to yield similar intensity on the camera chip by providing a wider wavelength window for the red filter. Thus the higher radiance in the blue spectral window at temperatures around 20000 K (where most atoms are already ionized) can be compensated. This allows for a maximum utilization of the conversion quantum efficiency of the camera chip without having areas of saturation. The employed 12 bit monochrome high-speed camera (PCO.dimax) is equipped with a macro-planar lens (Zeiss T* 2/100mm ZF) and provides up to 33000 *frames per second* (fps) with resolution of 1100x300 pixel and 110 μm/pixel. Exposure times were 25, 20, 15 and 12 μs for stationary plasma currents of 100, 125, 150 and 200 A, respectively and 25 μs for transient plasma currents. The high-speed setup has been calibrated and adjusted (see section 3.8.7) and setup dependent transfer functions have been included in the evaluation. A typical image acquired with the employed setup is shown in Figure 3.2.

3.2.2 Description of setup employing high-resolution spectrometer

In order to validate results obtained with the high-speed setup, measurements of stationary Argon plasmas have been evaluated with a high-resolution optical emission spectrometer. Therefore the setup of the spectrometer which is located at INP Greifswald, Germany will be briefly described in the following. The spectroscopy system (Acton-750mm) is equipped with an intensified charged coupled device (iccd: PI-Max2, Roper scientific) and provides two-dimensional information of side-on position (one dimension) and wavelength (second dimension). A schematic of the setup is shown in Figure 3.3. The wavelength resolution is 3 pm and intervals from 485.195 to 490.780 nm and 694.311 to 697.650 nm have been evaluated in successive experiments assuming reproducibility of the stationary plasma process. The resolution of the side-on position is 11.4 μm/pixel. Plasma radiance is focused on the entrance slit of the spectrometer employing an optical system and spectrally resolved by the diffraction grating before being imaged on the iccd. Two different side-on positions (1 mm and 7 mm below the tungsten electrode) have been eval-

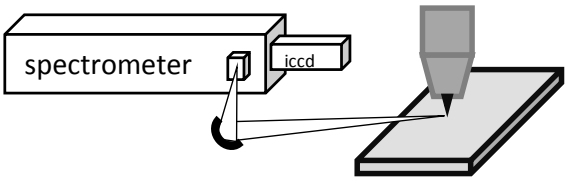

Figure 3.3: Experimental spectrometer setup for validation of measurement results.

uated for comparison of results obtained from the high-speed setup. The spectrometer setup has been calibrated and setup dependent transfer functions have been included in the evaluation.' [4]

3.3 Theory of plasma composition calculations and spectral emission coefficients

In this section the theory and implementation of plasma composition calculations and spectral emission coefficients that were utilized for the evaluation will be described. Therefor a condensed derivation of the employed equations will be performed. For a more detailed description of the theory the reader is referred to e.g. [105, 42, 75, 24].

3.3.1 The Saha equation

Ionization of A_i ($i = 0$ for neutral atom, $i > 0$ for ion species) and recombination of A_{i+1} with a free electron occurring in a plasma can be described by the following equation:

$$A_i + \left\{ \begin{array}{c} e^- \\ \gamma \\ B \end{array} \right\} \underset{\text{recombination}}{\overset{\text{ionization}}{\rightleftharpoons}} A_{i+1} + e^- + \left\{ \begin{array}{c} e^- \\ \gamma \\ B \end{array} \right\} \tag{3.1}$$

where e^-, γ and B denote electron, photon and another atom/ion, respectively. Note that for the recombination the three-body interaction is in general necessary for conservation of momentum and energy. From this it follows that a change in the particle density $n_{A,i}$ yields

$$\frac{dn_{A,i}}{dt} = -n_{A,i} \cdot n_{\{e,\gamma,B\}} \cdot \alpha_{\text{ion}} + n_{A,i+1} \cdot n_e \cdot n_{\{e,\gamma,B\}} \cdot \beta_{\text{rec}}, \tag{3.2}$$

where α_{ion} and β_{rec} are ionization and recombination rates and n_e is the density of free electrons. In a stationary state $dn_{A,i}/dt = 0$ an ionization equilibrium exists which yields the Saha equation:

$$\frac{\alpha_{\text{ion}}}{\beta_{\text{rec}}} = \frac{n_{A,i+1} n_e}{n_{A,i}} = K_i(T_e), \tag{3.3}$$

where $K_i(T_e)$ is a function of the electron temperature T_e (for the free electrons in the plasma). Since the probability for ionization is proportional to $\exp(-E_{\text{ion}} k_B^{-1} T^{-1})$, it follows for the ratio of $n_{A,i+1}/n_{A,i}$:

$$\frac{n_{A,i+1}}{n_{A,i}} \propto \exp\left(-\frac{E_{\text{ion}}}{k_B T_e}\right), \tag{3.4}$$

where k_B is the Boltzmann constant. The contribution of n_e to the Saha equation follows from the relation between uncertainty in position Δx and momentum Δp which are connected via the Planck constant h:

$$\Delta x \Delta p \propto h. \tag{3.5}$$

A free electron exhibits only kinetic energy E due to its translational movement,

$$E = \frac{1}{2} m_e v^2 = \frac{p^2}{2m_e}, \tag{3.6}$$

where m_e is the electron mass and this kinetic energy is in the order of $k_B T_e$. Thus the uncertainty in momentum is given by $\Delta p \propto \sqrt{m_e k_B T_e}$ and the uncertainty in position is $\Delta x \propto h/\sqrt{m_e k_B T_e}$. The corresponding uncertainty in volume is

$$\Delta V \propto (\Delta x)^3 \propto \left(\frac{h^2}{m_e k_B T_e} \right)^{3/2}, \tag{3.7}$$

within which only one free electron is located. Finally the electron density scales as

$$n_e \propto \left(\frac{m_e k_B T_e}{h^2} \right)^{3/2}. \tag{3.8}$$

Electrons, atoms and ions can be in more than one state at a given energy level. This degeneracy of states is taken into account by introducing the partition functions Z_i, which for a system with discrete energy levels read:

$$Z_i = \sum_j g_{i,j} \exp\left(-\frac{E_{i,j}}{k_B T_e} \right). \tag{3.9}$$

The partition functions represent the average value of the degree of degeneracy $g_{i,j}$ with electronic state j. Since the electron can be in the two states spin up or spin down, the partition function of the electron is 2. Following from equations 3.4, 3.8 and 3.9, the complete Saha equation can be written:

$$\frac{n_e n_{A,i+1}}{n_{A,i}} = \frac{2Z_{i+1}}{Z_i} \left(\frac{2\pi m_e k_B T_e}{h^2} \right)^{\frac{3}{2}} \exp\left(-\frac{E_{i,ion} - \Delta E_{i,ion}}{k_B T_e} \right), \tag{3.10}$$

where $\Delta E_{i,ion} = ie^2/(4\pi\varepsilon_0\lambda_D)$ is the decrease of the ionization energy resulting from the Coulomb force of surrounding ions, with ε_0 the vacuum permittivity and λ_D the Debye length. The latter follows from the equilibrium between thermal energy $k_B T$ and electric energy (the solution of the line integral $\int dx$ over the Coulomb force $e|\vec{E}|$ where e is the electron charge and $|\vec{E}|$ is the absolute value of the electric field strength):

$$e|\vec{E}|x = k_B T_e. \tag{3.11}$$

The electric field strength of a surface charge density is

$$|\vec{E}| = \frac{1}{\varepsilon_0} \frac{Q}{A}, \tag{3.12}$$

where $Q = Axn_e e$ is the charge density on the surface A multiplied by a small length x. Hence it follows for the Debye length:

$$e\left(\frac{en_e x}{\varepsilon_0}\right)x = k_B T_e \Leftrightarrow x = \lambda_D = \sqrt{\frac{\varepsilon_0 k_B T_e}{e^2 n_e}}. \tag{3.13}$$

Considering the different plasma species, the Debye length writes

$$\lambda_D = \left(\frac{\varepsilon_0 k_B}{e^2\left(\frac{n_e}{T_e} + \sum_{i=1}^{N}\frac{n_{A,i}}{T_e/\theta}\right)}\right)^{1/2}, \tag{3.14}$$

where $\theta = T_e/T_h$ is the ratio of electron and heavy species temperature and N is the highest degree of ionization.

3.3.2 Solving the Saha equation for monoatomic plasmas in thermodynamic equilibrium

Solving the Saha equation for a monoatomic plasma (e.g. Argon) means to find solutions for the densities of the atomic species $n_{A,i}$ and the electron density n_e. For a plasma consisting of N degrees of ionization this means to find solutions for $N+2$ unknown densities. This can be achieved by solving a system of $N+2$ equations which consists of N of Saha equations K_1 to K_N and two additional equations. One of these additional equations is the ideal gas law:

$$P = k_B T_e n_e + k_B T_h\left(n_{A,0} + n_{A,1} + ...\right) = k_B T_e\left(n_e + \frac{1}{\theta}\sum_{i=0}^{N} n_{A,i}\right), \tag{3.15}$$

where P is the gas pressure. The other equation follows from the fact that the number of free electrons must be equal to the sum of i times the number of ions with degree of ionization i. This quasineutral gas condition yields an equation for the densities of atomic species for a quasineutral plasma as long as the densities are calculated with respect to volumes of a length scale larger than the Debye length:

$$n_e = \sum_{i=1}^{N} i\, n_{A,i}. \tag{3.16}$$

For this work the Saha equation was solved for Argon plasmas with maximum degree of ionization $N = 2$. The corresponding four equations yield:

$$K_1 = \frac{n_e n_{A,1}}{n_{A,0}} \tag{3.17}$$

$$K_2 = \frac{n_e n_{A,2}}{n_{A,1}} \tag{3.18}$$

$$n_e = n_{A,1} + 2n_{A,2} \tag{3.19}$$

$$\frac{P}{k_B T_e} = n_e + \frac{1}{\theta}\left(n_{A,0} + n_{A,1} + n_{A,2}\right). \tag{3.20}$$

They can be combined to the following equation for the density of free electrons:

$$\begin{aligned}\frac{P}{k_B T_e} &= n_e + \frac{1}{\theta}\left(n_{A,0} + n_{A,1} + n_{A,2}\right) \\ &= n_e + \frac{1}{\theta} n_{A,0}\left(1 + \frac{K_1}{n_e} + \frac{K_1 K_2}{n_e^2}\right) \\ &= n_e + \left[1 + \frac{1}{\theta}\frac{1 + \frac{K_1}{n_e} + \frac{K_1 K_2}{n_e^2}}{\frac{K_1}{n_e} + \frac{2K_1 K_2}{n_e^2}}\right] \end{aligned} \tag{3.21}$$

$$\Rightarrow n_e^3 + n_e^2\left(1+\theta\right)K_1 + n_e K_1\left(\left(1+2\theta\right)K_2 - \theta\frac{P}{k_B T_e}\right) - 2\theta K_1 K_2 \frac{P}{k_B T_e} = 0. \tag{3.22}$$

Although such a cubic algebraic equation has an analytic solution, the implementation was performed by linearizing and iteratively refining the solution:

$$\left(n_e^{(k+1)}\right)^3 \approx \left(n_e^{(k)}\right)^3 + 3\left(n_e^{(k)}\right)^2\left(n_e^{(k+1)} - n_e^{(k)}\right) \tag{3.23}$$

$$\begin{aligned}\Rightarrow \left(n_e^{(k)}\right)^3 + \left(n_e^{(k)}\right)^2\left(1+\theta\right)K_1 + n_e^{(k)} K_1\left(\left(1+2\theta\right)K_2 - \theta\frac{P}{k_B T_e}\right) - 2\theta K_1 K_2 \frac{P}{k_B T_e} + \\ \left[3\left(n_e^{(k)}\right)^2 + 2n_e^{(k)}\left(1+\theta\right)K_1 + K_1\left(\left(1+2\theta\right)K_2 - \theta\frac{P}{k_B T_e}\right)\right]\left(n_e^{(k+1)} - n_e^{(k)}\right) \approx 0.\end{aligned} \tag{3.24}$$

This equation has the following solution for the next step of iteration:

$$n_e^{(k+1)} = n_e^{(k)} - \frac{\left(n_e^{(k)}\right)^3 + \left(n_e^{(k)}\right)^2\left(1+\theta\right)K_1 + n_e^{(k)} K_1\left(\left(1+2\theta\right)K_2 - \theta\frac{P}{k_B T_e}\right) - 2\theta K_1 K_2 \frac{P}{k_B T_e}}{3\left(n_e^{(k)}\right)^2 + 2n_e^{(k)}\left(1+\theta\right)K_1 + K_1\left(\left(1+2\theta\right)K_2 - \theta\frac{P}{k_B T_e}\right)}. \tag{3.25}$$

As a start approximation of $n_e^{(1)}$ the solution for a weak ionization is employed:

$$n_e^2 + n_e\left(1+\theta\right)K_1 - \theta\frac{P}{k_B T_e}K_1 = 0 \Rightarrow n_e = -\frac{1+\theta}{2}K_1 + \sqrt{\left(\frac{1+\theta}{2}K_1\right)^2 + \theta\frac{P}{k_B T_e}K_1}. \tag{3.26}$$

This iterative method converges already after 4 iterations. After calculating the electron density it is possible to calculate the densities of the other atomic species:

$$n_{A,0} = \frac{n_e}{\frac{K_1}{n_e} + 2\frac{K_1 K_2}{n_e^2}},\ n_{A,1} = n_A\frac{K_1}{n_e} \text{ and } n_{A,2} = n_{A,1}\frac{K_2}{n_e}. \tag{3.27}$$

However, since the density of charged particles does modify the Saha factors K_1 and K_2 through the corresponding ionization energies, a further iterative cycle is required. Hence the calculation of n_e, $n_{A,0}$, $n_{A,1}$, $n_{A,2}$, λ_D, $E_{\text{ion},1}$, $E_{\text{ion},2}$, K_1 and K_2 was done with iterative refinement in a nested for-loop with $k = 5$ and $l = 5$ iterations. While equation 3.25 is iteratively solved in the inner for-loop, the Debye length λ_D, the ionization energies $E_{\text{ion},1}$ and $E_{\text{ion},2}$ and the Saha factors K_1 and K_2 are recalculated based on their values from the previous iteration in an outer for loop. The implementation has been done with Matlab and is shown in what follows:

```
KI=(2.*Z2./Z1).*((2.*pi.*m_e.*k_B.*Te./h.^2)).^1.5.*...
        exp(-EIion0.*e./(k_B.*Te));
KII=(2.*Z3./Z2).*((2.*pi.*m_e.*k_B.*Te./h.^2)).^1.5.*...
        exp(-EIIion0.*e./(k_B.*Te));
%Start approximation for electron density:
ne=-0.5.*(1+theta).*KI+(0.25.*(1+theta).^2.*KI.^2+theta.*KI.*P_out.*...
    1e5./(k_B.*Te)).^0.5;
%Calculation of electron density and related parameters
%with iterative refinement:
k=5;
l=5;
for i=1:l,
    for j=1:k,
        ne=ne-((ne.^3+ne.^2.*(1+theta).*KI+ne.*KI.*...
            ((1+2.*theta).*KII-theta.*(P_out.*1e5./(k_B.*Te)))...
            -2.*theta.*KI.*KII.*(P_out.*1e5./(k_B.*Te))))./...
            (3.*ne.^2+2.*ne.*(1+theta).*KI+KI.*((1+2.*theta).*...
            KII-theta.*(P_out.*1e5./(k_B.*Te)))));
    end
    nAI=ne./((KI./ne)+2.*(KI.*KII./ne.^2));
    nAII=nAI.*KI./ne;
    nAIII=nAII.*KII./ne;
    lambda_D=sqrt(eps0.*k_B./(e.^2.*(ne./Te+theta.*nAII./...
        Te+theta.*4.*nAIII./Te)));
    EIion=EIion0-(e./(4.*pi.*eps0.*lambda_D));
    EIIion=EIIion0-(2.*e./(4.*pi.*eps0.*lambda_D));
    KI=(2.*Z2./Z1).*((2.*pi.*m_e.*k_B.*Te./h.^2)).^1.5.*...
        exp(-EIion.*e./(k_B.*Te));
    KII=(2.*Z3./Z2).*((2.*pi.*m_e.*k_B.*Te./h.^2)).^1.5.*...
        exp(-EIIion.*e./(k_B.*Te));
end
```

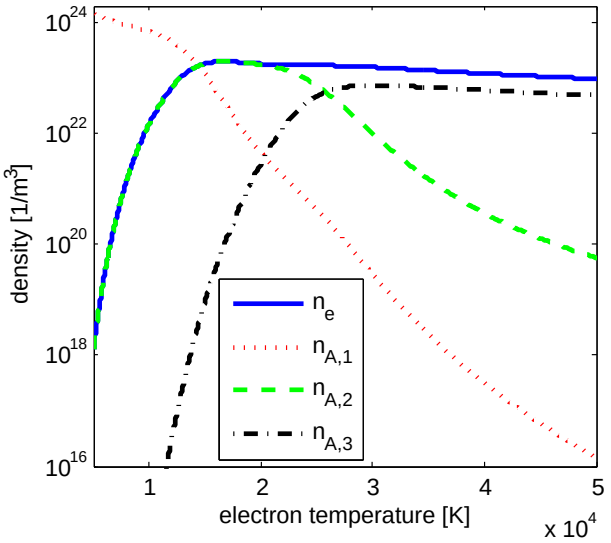

Figure 3.4: Calculated electron density (n_e) and densities of atoms and ions ($n_{A,1}$, $n_{A,2}$ and $n_{A,3}$).

Figure 3.4 shows calculated densities of electrons and atomic species for a temperature interval of 5000 K to 50000 K.

3.3.3 Calculation of emission coefficients

'One well-known way to determine plasma temperature is optical emission spectroscopy (OES). It has been established as a widely used method to analyze arc radiation, e.g. to determine profiles of species temperature and density in free burning arcs. Therefor the emitted radiance is spectrally resolved, analyzed and can be compared to emission coefficients calculated at certain temperatures. The analysis of the emitted radiance consists usually of different steps. If radiance is measured from one side-on position, the first step comprises the reconstruction of the spatial distribution of the radiance by Abel inversion which is described in section 3.4. Subsequently different methods for evaluation of measured emission coefficients are possible which are described in section 3.5. Emission coefficients can also be calculated in parallel with the analysis of experimental parameters. Since these calculated emission coefficients are functions of temperature, comparison of measured and calculated emission coefficients allow an estimation of the plasma temperature. The calculation of emission coefficients will be described in what follows. In this work three main processes resulting in plasma emission are considered:

- Bremsstrahlung $\varepsilon_\lambda^{ffi}$ of free electrons at ions (free $\rightarrow$ free ion)
- Emission due to recombination of free electrons with ions ε_λ^{fb} (free $\rightarrow$ bound)
- Line emission of bound electrons within atoms and ions ε_λ^{bb} (bound $\rightarrow$ bound)

The latter results from a change of an electron state from an excited bound state E_u to a bound state with lower energy E_d. This change results in the emission of a photon with energy $E_u - E_d$ and wavelength $\lambda_0 = hc/(E_u - E_d)$. This process has a transition probability rate equal to A_{ud}. The resulting emission coefficient as the energy emitted per unit solid angle 4π, time and volume within a narrow spectral window between λ and $\lambda + \Delta\lambda$ is given by the density $n_{u,i}$ of atoms or ions which are in the excited state E_u, the transition probability A_{ud} and the emitted photon energy hc/λ_0:

$$\varepsilon_\lambda^{bb}\Delta\lambda = \frac{1}{4\pi}\frac{hc}{\lambda_0}A_{ud}n_u P(\lambda-\lambda_0)\Delta\lambda. \tag{3.28}$$

Due to the interaction with other electrons, atoms or ions the resulting line emission coefficients are spectrally broadened. This effect results in a spectral line profile $P(\lambda-\lambda_0)$, where

$$\int_{\lambda_0-\Delta\lambda/2}^{\lambda_0+\Delta\lambda/2} P(\lambda-\lambda_0)\,d\lambda = 1. \tag{3.29}$$

Note that if line radiation is measured with a spectral filter, the filter width should be wide enough so that the complete spectral profile is contained within the transmitted wavelength window. The atom or ion density $n_{u,i}$ can be calculated from the Boltzmann factor in thermodynamic equilibrium:

$$n_{u,i} = \frac{g_u}{g_{\text{ground}}}n_{\text{ground}}\exp\left(-\frac{E_u}{k_B T_e}\right) = \frac{g_u}{g_{\text{ground}}}\frac{g_{\text{ground}}}{Z_i}n_i\exp\left(-\frac{E_u}{k_B T_e}\right) = \frac{g_u}{Z_i}n_i\exp\left(-\frac{E_u}{k_B T_e}\right), \tag{3.30}$$

where n_i is the total density of atoms ($i=0$) or ions ($i>0$).' [4]

Radiance is emitted when a free electron is accelerated by an ion. The spectral emission coefficient $\varepsilon_f \Delta f$ which is emitted within a spectral window $\Delta\lambda = c/\Delta f$ is the energy E per volume, per time and per solid angle. This energy can be estimated by the electric field at distance r of a dipole:

$$|\vec{E}_{\mathrm{rad}}| \propto \frac{e}{4\pi\varepsilon_0}\frac{1}{r}\frac{a_e}{c^2}, \tag{3.31}$$

where a_e is the acceleration of electrons and c the speed of light. It follows for the energy:

$$E \propto \underbrace{\frac{\varepsilon_0}{2}|\vec{E}_{\mathrm{rad}}|^2}_{\text{energy density}} \underbrace{4\pi r^2 c\Delta t}_{\text{volume}}. \tag{3.32}$$

The resulting emission coefficient $\varepsilon_f \Delta f$ writes:

$$\varepsilon_f \Delta f \propto \frac{1}{4\pi} n_e \left(\frac{\varepsilon_0}{2}|\vec{E}_{\mathrm{rad}}|^2 4\pi r^2 c\Delta t\right) \cdot \underbrace{n_{A+}\sigma_{e-A+}\underbrace{\Delta x}_{v_e\Delta t}}_{\substack{\text{probability for acceleration of free electrons}}} \cdot \frac{1}{\Delta t}\frac{1}{f}\Delta f. \tag{3.33}$$

With the following four approximations,

$$F = m_e a_e \approx \frac{e^2}{4\pi\varepsilon_0}\frac{1}{b^2}, \tag{3.34}$$

$$\sigma_{e-A+} \approx \pi b^2, \text{ where } bf \approx v_e, \tag{3.35}$$

$$v_e \approx \sqrt{\frac{k_B T_e}{m_e}}, \tag{3.36}$$

$$\Delta t \approx \frac{1}{f}. \tag{3.37}$$

the emission coefficient reads in terms of frequency:

$$\begin{aligned}\varepsilon_f \Delta f &\propto \frac{1}{4\pi} n_e n_{A+} \left(\frac{\varepsilon_0}{2}\left(\frac{e}{4\pi\varepsilon_0}\right)^2\left(\frac{e^2}{4\pi\varepsilon_0}\right)^2 \frac{1}{m_e}\frac{1}{b^4}\frac{1}{r^2 c^4} 4\pi r^2 c \frac{1}{f}\right) \pi b^2 \sqrt{\frac{k_B T_e}{m_e}}\frac{1}{f}\Delta f \\ &\propto \frac{1}{8} n_e n_{A+}\left(\frac{e^2}{4\pi\varepsilon_0}\right)^3 \frac{1}{m_e^2 c^3}\frac{1}{f^2}\frac{1}{b^2}\sqrt{\frac{k_B T_e}{m_e}}\Delta f\end{aligned} \tag{3.38}$$

and in terms of wavelength for a spectral window of $\Delta\lambda$:

$$\varepsilon_\lambda \Delta\lambda \propto \frac{1}{8} n_e n_{A+}\left(\frac{e^2}{4\pi\varepsilon_0}\right)^3 \frac{1}{m_e c^2}\frac{1}{\lambda^2}\frac{1}{\sqrt{m_e k_B T_e}}\Delta\lambda. \tag{3.39}$$

'In the case of Argon with a maximum degree of ionization of two, the complete equations for the emission coefficients $\varepsilon_\lambda^{ffi}$ and ε_λ^{fb} of a wavelength interval $\Delta\lambda$ write in SI units [105]:

$$\varepsilon_\lambda^{ffi} = 1.63\cdot 10^{-43}\frac{\Delta\lambda}{\lambda^2} n_e \frac{n_{Ar+} + 4n_{Ar++}}{\sqrt{T}} \exp\left(\frac{-hc}{\lambda k_B T}\right)\xi_\lambda^{ffi}, \tag{3.40}$$

$$\varepsilon_\lambda^{fb} = 1.63\cdot 10^{-43}\frac{\Delta\lambda}{\lambda^2} n_e \frac{n_{Ar+} + 4n_{Ar++}}{\sqrt{T}} \left(1 - \exp\left(\frac{-hc}{\lambda k_B T}\right)\right)\xi_\lambda^{fb}, \tag{3.41}$$

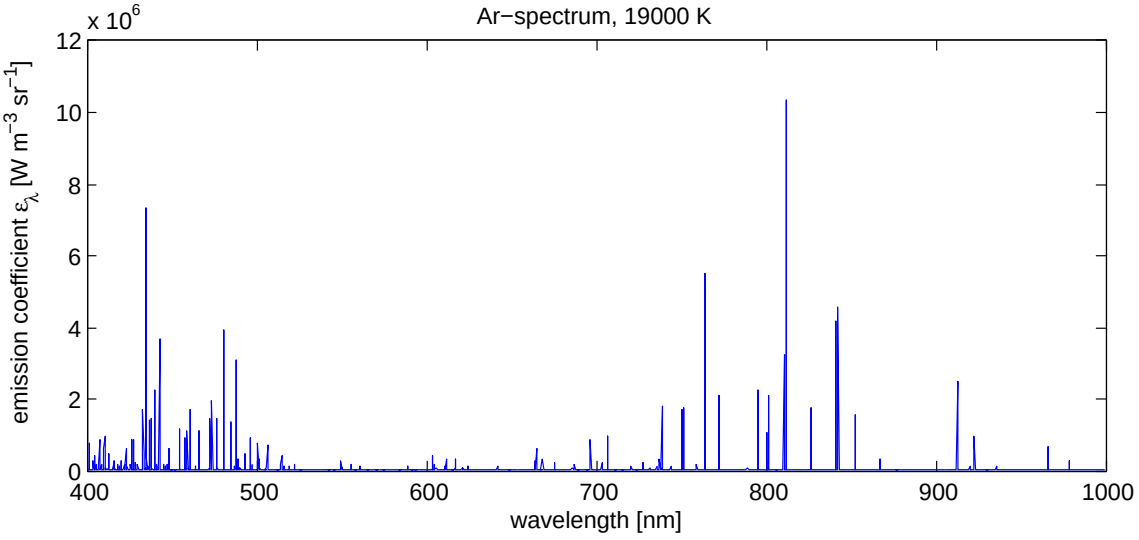

Figure 3.5: Calculated emission spectrum of Argon at 19000 K.

where $\xi_\lambda^{ffi} \approx 1.23$ and $\xi_\lambda^{fb} \approx 2$ is the Biberman factor for Bremsstrahlung and recombination, respectively. One can easily see, that in the case where the Biberman factors are set equal to 1, the sum of both continuum contributions (equations 3.40 and 3.41) no longer contains any Boltzmann factor $\exp(-hc/\lambda k_B T_e)$ and displays the same form and order of magnitude as derived in equation 3.39. An example of a calculated emission spectrum of Argon at 19000 K including line- and continuum radiation is shown in Figure 3.5. The Argon atom lines in the range from 600 nm to 1000 nm and the Argon ion lines in the range from 400 nm to 600 nm are clearly visible. The continuum ranges from $1 \times 10^4\,\mathrm{W\,m^{-3}\,sr^{-1}}$ at 770 nm to $3 \times 10^4\,\mathrm{W\,m^{-3}\,sr^{-1}}$ at 420 nm.

3.4 Three-dimensional reconstruction of axially symmetric intensity distributions employing inverse Abel transformation

Measurements of the side-on position performed as described in section 3.2 collect information of the so called radiance $I(y)$ in terms of $[\mathrm{W\,m^{-2}\,sr^{-1}}]$. In order to reconstruct the emission coefficient ε_λ $([\mathrm{W\,m^{-3}\,sr^{-1}}])$ an inversion of the measured side-on profile has to be performed. When the side on profile is axially symmetric and the plasma is not self-absorbing in the considered spectral region, this inversion can be performed utilizing the well known Abel transformation:

$$I(y) = \int_{-X(y)}^{X(y)} \varepsilon_\lambda\left(\sqrt{x^2+y^2}\right) dx = 2\int_y^R \frac{\varepsilon_\lambda(r)r}{\sqrt{r^2-y^2}} dr. \tag{3.42}$$

The corresponding inversion formula yields

$$\varepsilon_\lambda(r) = \frac{1}{\pi}\int_r^R \frac{I'(y)}{\sqrt{y^2-r^2}} dy \tag{3.43}$$

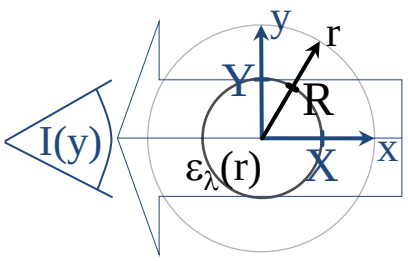

Figure 3.6: Geometrical interpretation of the Abel transformation.

for the emission coefficient, where a geometric interpretation is shown in figure 3.6. The implementation of the Abel inversion is usually not performed employing equation 3.43 since the numeric calculation of the derivative of the radiance deals with substantial noise amplification. Thus different alternative methods have been developed [34, 40, 17, 13, 23, 83, 64] which make use of spline or polynomial approximations followed by analytical inversion and setting additional constraints on e.g. non-negativity or an implied physical model of the plasma emission.

3.4.1 Analytical Abel-inversion procedure

In this work two different Abel inversion methods have been performed in order to show influences on the results which are due to each inversion procedure. The first method (*Abel inversion 1*) assumes a Gaussian distribution multiplied with a second order polynomial for the emission coefficient:

$$\varepsilon_\lambda(r) = A\left(1+c_1 r^2\right)\exp\left(-\frac{r^2}{2\sigma^2}\right), \tag{3.44}$$

where A, c_1 and σ are the fit parameters. From this assumption the profile of the radiance can be calculated:

$$I(y) = \int_{-\infty}^{+\infty} A\left(1+c_1 y^2 + c_1 x^2\right)\exp\left(-\frac{x^2+y^2}{2\sigma^2}\right)dx \tag{3.45}$$

$$\Rightarrow I(y) = A'\left(1+c_1' y^2\right)\exp\left(-\frac{y^2}{2\sigma^2}\right), \tag{3.46}$$

where $A' = A\sqrt{2\pi\sigma^2}\left(1+c_1\sigma^2\right)$ and $c_1' = c_1/\left(1+c_1\sigma^2\right)$. By employing a non-linear least squares fit procedure with model function 3.46 to the measured side-on profiles, an analytic function for the radiance is obtained. The subsequently performed analytic inversion yields the unknown fit parameters A, c_1 and σ. Figure 3.7 shows three different radiances for three different side-on positions along an 8 mm long Argon arc and the corresponding results of the fit procedures. The errors resulting from this inversion method result only from the confidence interval of the non-linear least squares fit.

3.4.2 Alternative Abel inversion algorithm allowing subsequent quantitative comparison of influences on temperature results

The second Abel inversion (*Abel inversion method 2*) that has been performed makes us of spline interpolation without an assumption on the implied physical model. The inverted

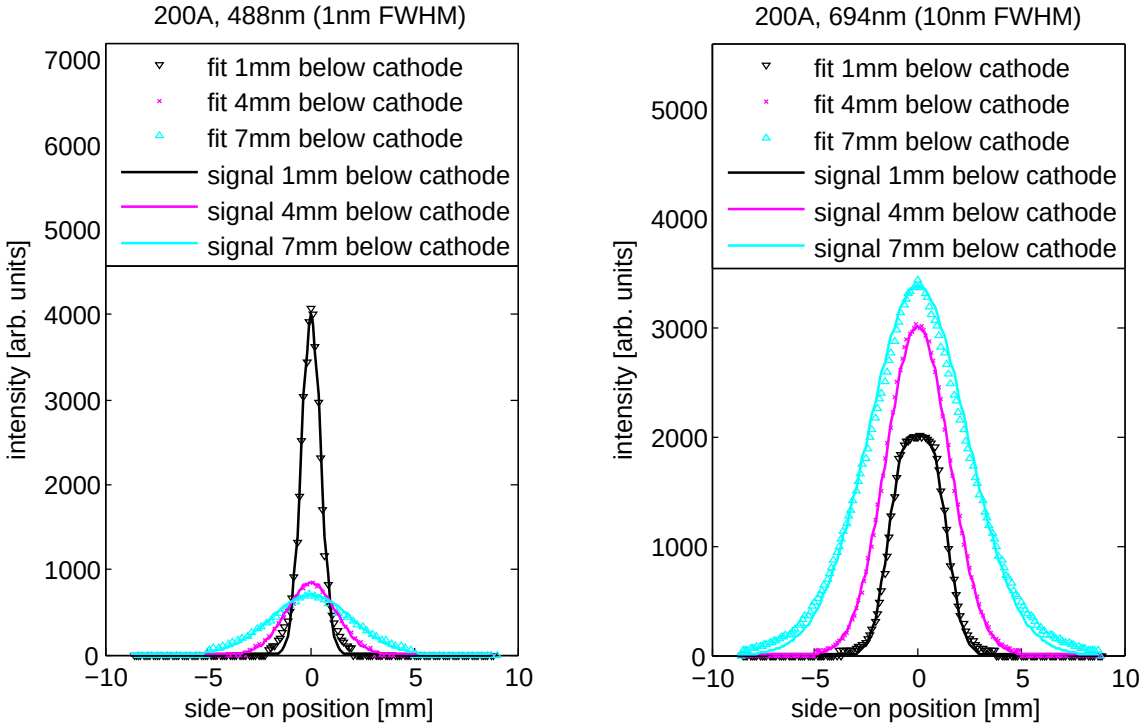

Figure 3.7: Comparison of fits and original intensities for the 488 nm interval at three different side-on positions (left). Comparison of fits and original intensities for the 694 nm interval at three different side-on positions (right).

profile is represented as

$$\varepsilon_{\lambda,k}(r) = \sum_{j=0}^{3} b_{jk}\,(r - r^*)^j \tag{3.47}$$

in the interval $r \in [r_k, r_{k+1}]$, where b_{jk} are the polynomial coefficients and r^* is the midpoint of the interval $[r_k, r_{k+1}]$. The coefficients b_{jk} can be found from the solution of the following equation:

$$\begin{pmatrix} (r_k - r^*)^3 & (r_k - r^*)^2 & (r_k - r^*) & 1 \\ 3(r_k - r^*)^2 & 2(r_k - r^*) & 1 & 0 \\ (r_{k+1} - r^*)^3 & (r_{k+1} - r^*)^2 & (r_{k+1} - r^*) & 1 \\ 3(r_{k+1} - r^*)^2 & 2(r_{k+1} - r^*) & 1 & 0 \end{pmatrix} \begin{pmatrix} b_{3k} \\ b_{2k} \\ b_{1k} \\ b_{0k} \end{pmatrix} = \begin{pmatrix} a_k \\ a'_k \\ a_{k+1} \\ a'_{k+1} \end{pmatrix} \tag{3.48}$$

The parameters a_i and a'_i are the values of the spline function and their derivatives where $i \in [0, K-1]$, and K is number of spline knots. With values for a_i and a'_i the thus obtained emission coefficient $\varepsilon_\lambda(r)$ can be used to calculate the side-on radiance profile $I_c(y)$ utilizing the Abel transformation from equation 3.42. A non-linear least squares method is subsequently employed to optimize values of a_i and a'_i by minimizing the squared sum of the deviation between the calculated radiances $I_c(y)$ and measured $I(y)$:

$$S = \sum_{i=0}^{N} [I_i - I_c(y_i)]^2, \tag{3.49}$$

where N is the number of measuring points. While *Abel inversion method 1* has the advantage of numerical stability, *Abel inversion method 2* can be used to fit arbitrary radiances.

Method #	Experimental setup	Evaluation of spectral data	Abel inversion algorithm # section 3.4
1, section 3.5.1	high-speed setup	ratio of emission coefficients	1
2, section 3.5.1	spectrometer	ratio of emission coefficients	1
3, section 3.5.2	spectrometer	single line method	2
4, section 3.5.3	spectrometer	Fowler-Milne method	1 and 2
5, section 3.5.4	spectrometer	quadratic Stark broadening	1

Table 3.1: Overview of employed measurement techniques and evaluation methods.

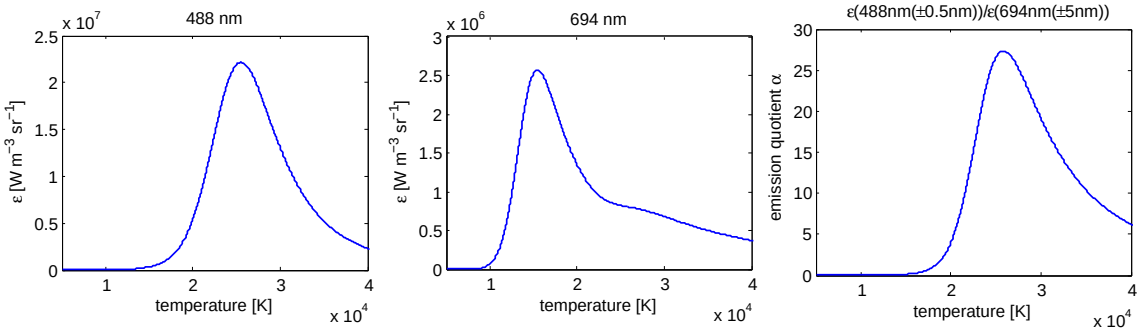

Figure 3.8: Emission coefficient within spectral window 487.5 nm - 488.5 nm (left), within spectral window 689 nm - 699 nm (centre) and corresponding α (right).

3.5 Methods for evaluation of emission coefficients

The methods for evaluation of emission coefficients are based on their dependence on wavelength and temperature. For emission coefficients obtained with the high-speed setup shown in Figure 3.1 a line ratio method has been employed (*Method 1*, Table 3.1). In order to validate experimental results obtained from *Method 1*, experimental data from measurements with a classical spectrometer (section 3.2.2) have been evaluated with four different methods (*Method 2-5*, Table 3.1). Details on the evaluation with the different methods are described subsequently.

3.5.1 Method of ratios of emission coefficients

The line ratio *Method 1* and *Method 2* (see Table 3.1) make use of the temperature dependence of the emission coefficients which are measured in the spectral region of 488 nm and 694 nm (Figure 3.8). While the maximum of emission coefficients is reached at 15500 K and 25600 K at the 488 nm and 694 nm intervals, respectively, the maximum of the emission quotient $\alpha(T)$:

$$\alpha(T) = \frac{\varepsilon_{[488]}(T)}{\varepsilon_{[694]}(T)} \tag{3.50}$$

is reached at 26000 K (Figure 3.8). This means that measured values of $\alpha(T)$ can be uniquely connected to plasma temperatures below 26000 K. Additionally, the relatively large gradient of $\alpha(T)$ in the temperature range of 15000 K to 25000 K allows for accurate temperature measurements in this region due to lower amplification of errors induced by error propagation of measured emission quotients $\alpha(r,z)$. The latter are obtained

point-by-point by superimposing and dividing measured emission coefficient distributions $\varepsilon_{[\lambda 1]}(r,z)$ and $\varepsilon_{[\lambda 2]}(r,z)$ of the simultaneously acquired (section 3.2) and inverted (section 3.4) side-on radiance profiles $I(y,z)$. While *Method 1* analyzes spectral intervals of 487.5 nm - 488.5 nm and 689 nm - 699 nm to obtain a two-dimensional axially symmetric temperature profile $T(r,z)$, *Method 2* analyzes spectral intervals of $\lambda_1 = [485.2, 490.8]$ nm and $\lambda_2 = [694.4, 697.6]$ nm with a resolution of 3 pm in order to obtain a one-dimensional axially symmetric temperature profile $T(r)$. The results of both methods can be compared where possible deviations are depending on experimental parameters only (section 3.6).

3.5.2 Evaluation of single discrete lines by calibration with a tungsten ribbon lamp

A raw image obtained from the spectrometer located at the INP Greifswald is shown in Figure 3.9 (a). The vertical axis represents the side-on position and the horizontal axis represents the wavelength. The resulting two dimensional image displays the radiance. An absolute intensity calibration allows to assign values in terms of $[\mathrm{W\,m^{-2}\,nm^{-1}\,sr^{-1}}]$ to the emission coefficient by the comparison of the radiance with the one of a calibrated tungsten ribbon lamp (*Method 3*, Table 3.1). A resulting spectral profile of one selected side-on position is depicted in Figure 3.9 (b). Here the broadening of the line is clearly visible. In general this broadening can be described by a Voigt profile which is a convolution of a Gaussian profile and a Lorentzian profile. The former is a result of the Doppler broadening which is in the range of 0.01 nm for Argon at atmospheric pressure at a temperature of 20000 K. The latter results from the quadratic Stark effect (interaction of a free electron with the electric dipole which is induced in an Argon atom by a foregoing interaction with other free electrons). Since the quadratic Stark broadening is dominant in the described case for atmospheric pressure Argon, the radiance can be described by a Lorentz profile:

$$I_\lambda = I_0 + \frac{I}{\pi}\frac{2}{\Delta\lambda}\frac{1}{1+\left(\frac{\lambda-\lambda_0}{\Delta\lambda/2}\right)^2}, \tag{3.51}$$

where I_0 is the background radiation, λ_0 is the line centre, I is the total line intensity and $\Delta\lambda$ is the FWHM. Hence the total line intensity of atomic transition $I(y)$ can be obtained by fitting the Lorentz profile for each side-on position to the measurement data. The thus obtained radiance $I(y)$ can be inverted by the Abel inversion (see section 3.4) and yields the emission coefficient $\varepsilon_\lambda(r)$ in terms of $[\mathrm{W\,m^{-3}\,sr^{-1}}]$ (see Figure 3.9 (c)). The latter can be used to determine the plasma temperature by calculations performed as described in section 3.3.3.

3.5.3 Evaluation employing Fowler-Milne method

The Fowler-Milne method (*Method 4*, Table 3.1) is based on the fact that the emission coefficient experiences a maximum with increasing temperature (see e.g. Figure 3.8) [31, 32]. This maximum is called *normal maximum* or *norm maximum*. This means that the observed radiance at a certain spectral interval is scaling down if temperature goes above this maximum. In the case of a free burning Argon arc where the maximum temperature occurs on the arc axis, a maximum in emission coefficient observed off-axis corresponds to the *normal maximum*. Hence the emission coefficient on an off-axis peak corresponds

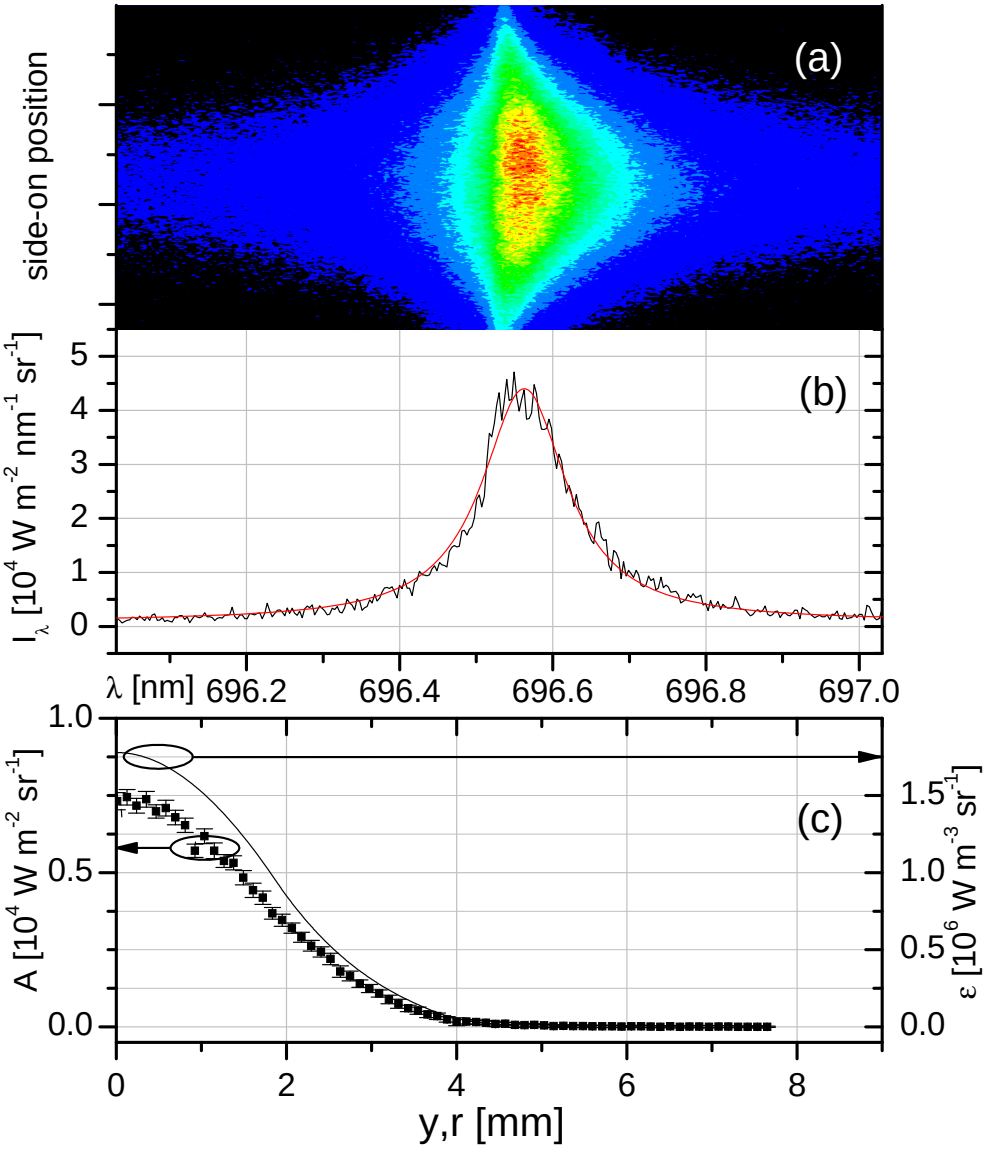

Figure 3.9: Example of the measurement for Method 3. (a) I_λ at different y positions plotted with a linear color scale; (b) same at one y position with a fit by Lorentz profile; (c) Wavelength-integrated radiance as function of side-on positions (left scale) and corresponding emission coefficient as function of radial position (right scale).

to a temperature of about 15000 K for a wavelength of 696.54 nm. In this work, measured radiances have been inverted according to section 3.4 yielding the emission coefficient $\varepsilon_\lambda(r)$. Subsequently measured $\varepsilon_\lambda(r)$ and calculated emission coefficients $\varepsilon_\lambda(T)$ have been integrated over a wavelength interval of 1 nm in order to average out noise induced by the spectroscopic system. Then measured emission coefficients $\varepsilon_{[\Delta\lambda]}(r)$ in terms of gray scale values have been scaled by their off-axis maximum and the calculated emission coefficients $\varepsilon_{[\Delta\lambda]}(T)$ in order to yield emission coefficients $\varepsilon_{[\Delta\lambda],\mathrm{new}}(r)$ in terms of $[\mathrm{W\,m^{-3}\,sr^{-1}}]$:

$$\varepsilon_{[\Delta\lambda],\mathrm{new}}(r) = \varepsilon_{[\Delta\lambda]}(r)\frac{\max\left(\varepsilon_{[\Delta\lambda]}(T)\right)}{\max\left(\varepsilon_{[\Delta\lambda]}(r)\right)}. \tag{3.52}$$

Finally the local plasma temperature distribution can be calculated by comparison of $\varepsilon_{[\Delta\lambda],\mathrm{new}}(r)$ with $\varepsilon_{[\Delta\lambda]}(T)$.

3.5.4 Evaluation of the 696.54 nm Ar-atom line width by quadratic Stark broadening

As mentioned in section 3.5.2 the quadratic Stark effect in atmospheric pressure Argon arcs at temperatures around 20000 K is the dominant effect contributing to line broadening [84]. In order to evaluate the line broadening (*Method 5*, Table 3.1), the spectroscopic data have been inverted in a first step according to section 3.4. Subsequently a Lorentz profile which has been fitted to the 696.54 nm Argon atom line yields the FWHM $\Delta\lambda$ which is uniquely connected to the electron density [84, 89, 107]:

$$\text{FWHM}\,\Delta\lambda\,[\text{nm}] = 0.0814\frac{n_e\,[\text{m}^{-3}]}{10^{23}}\left(\frac{T_e\,[\text{K}]}{13000}\right)^{0.3685}. \tag{3.53}$$

Note that this equation can only be employed for the 696.54 nm Ar-atom line for $n_e < 2\cdot10^{23}\,\text{m}^{-3}$ and $13000\,\text{K} < \text{T} < 24000\,\text{K}$. Assuming *single temperature LTE* the plasma temperature can be subsequently determined from the plasma composition calculations (section 3.3).

The line broadening also results in a shift of the line center which can be observed from Figure 3.9 (a) where an asymmetry of the profile is visible. This is due to the line-of-sight integration of the radiation. In general, the evaluation of the proportions of the coupled line width and line shift (which are higher in hotter regions of the arc) can be used to validate the existing theoretical models of Stark broadening but is not part of this work.

3.6 Results of plasma temperature measurements and comparison with classical optical emission spectroscopy

Figure 3.10 shows radial plasma temperature distributions of stationary free burning Argon arcs at currents of 100, 125, 150 and 200 A. These temperatures were obtained using the high-speed setup (Figure 3.1) employing a line ratio method (*Method 1*, Table 3.1). Each displayed surface color corresponds to a temperature interval of 1000 K. Maximum temperatures were measured in the hot cathode region of the 200 A arc. There the plasma temperature reaches a value of 20000 K. From the cathode region the temperature decreases in axial and radial direction until the anode region, where temperature increases again due to radial constriction of the arc. The results shown in Figure 3.10 have been validated with different methods employing a high-resolution spectrometer (section 3.2.2). The evaluation has been performed employing a line ratio method (*Method 2*) similar to the original method, a single line method (*Method 3*), the Fowler-Milne method (*Method 4*) and the quadratic Stark effect (*Method 5*). The results are displayed in Figures 3.11, 3.12, 3.13 and 3.14 for measurement positions 1 mm below the cathode and 1 mm above the anode, where the error bars are displayed for *Method 1*. The latter were calculated by error propagation of the 68.3% confidence intervals of the employed *Abel inversion method 1*. In general the results show very good agreement. In the outer regions of the arcs, temperatures obtained with single line methods (*Methods 3-5*) are higher than temperatures obtained with line ratio methods (*Methods 1-2*). This might be due to a departure from '*single temperature LTE*' and leads to overestimation of the temperature in the displayed cases, while the line ratio methods still show the correct electron temperatures provided that the plasma is in a '*two temperature LTE*' (see section 3.8.2). Since the amount of

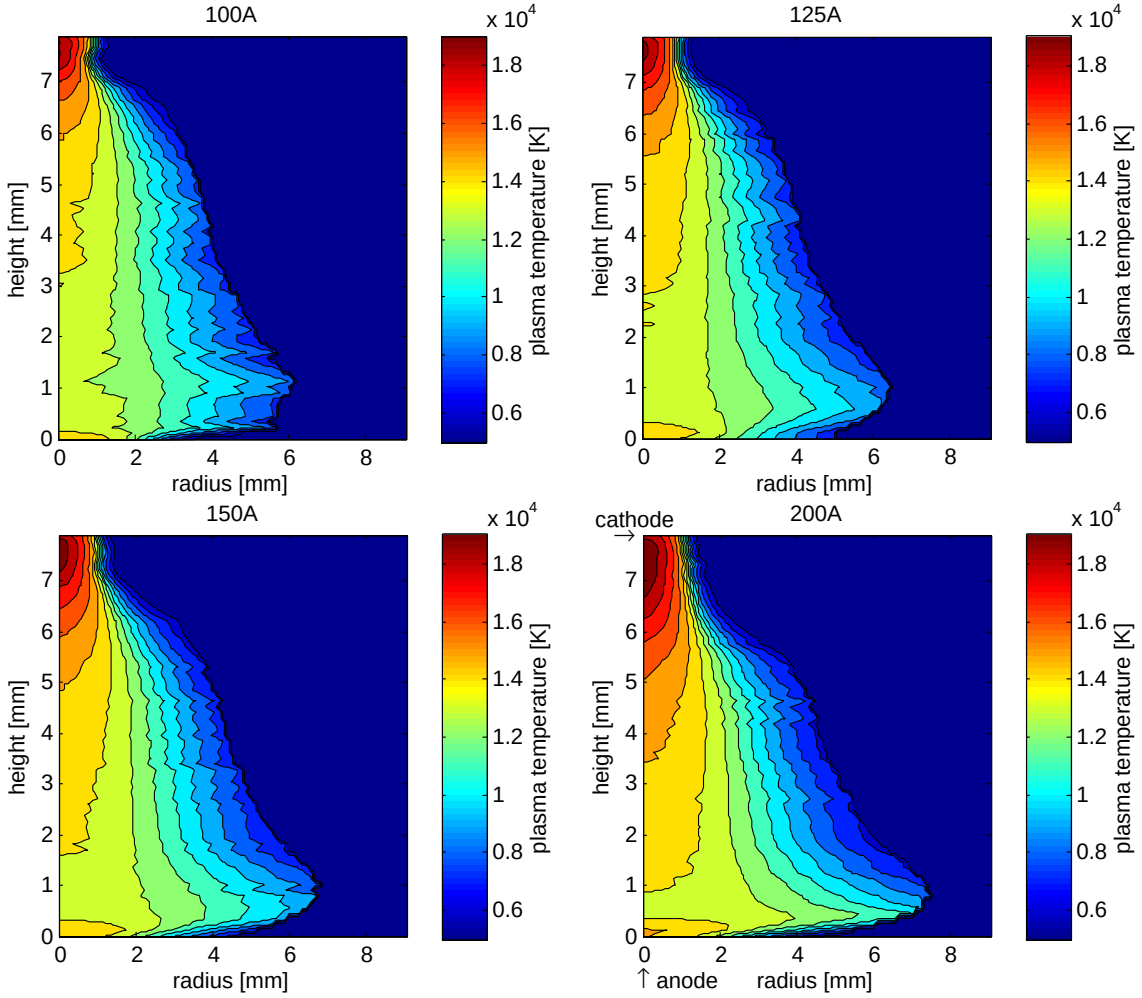

Figure 3.10: Plasma temperature distribution of a free burning Argon arc operated from 100 to 200 A. Each surface color indicates a temperature interval of 1000 K. The highest temperature occurs at a current of 200 A in the cathode region which is in the range of 19000 to 20000 K

atomic Argon is diminishing in the cathode region, the quadratic Stark broadening of the 696.54 nm line was not evaluated in this region. Section 3.4 introduces two different procedures for the inversion of side-on radiances. In order to show the influences of these two methods, Figure 3.11 displays their results for the Fowler-Milne method (*Method 4*). While in general the two temperature profiles show small deviations, note that results can differ by up to 5% which can be seen in the cathode region. The accuracy of Abel inversion procedures is inherently minimal at the center of the inverted profile. This follows from the fact that radiation from the central part of the arc column contributes only to the limited radial range of the recorded side-on radiance profile. Therefore the discrepancies in the center of the temperature profiles between two Abel inversion algorithms can be attributed to the systematic differences in approximation of the central value of emission coefficient made by the inversion procedures.' [4]

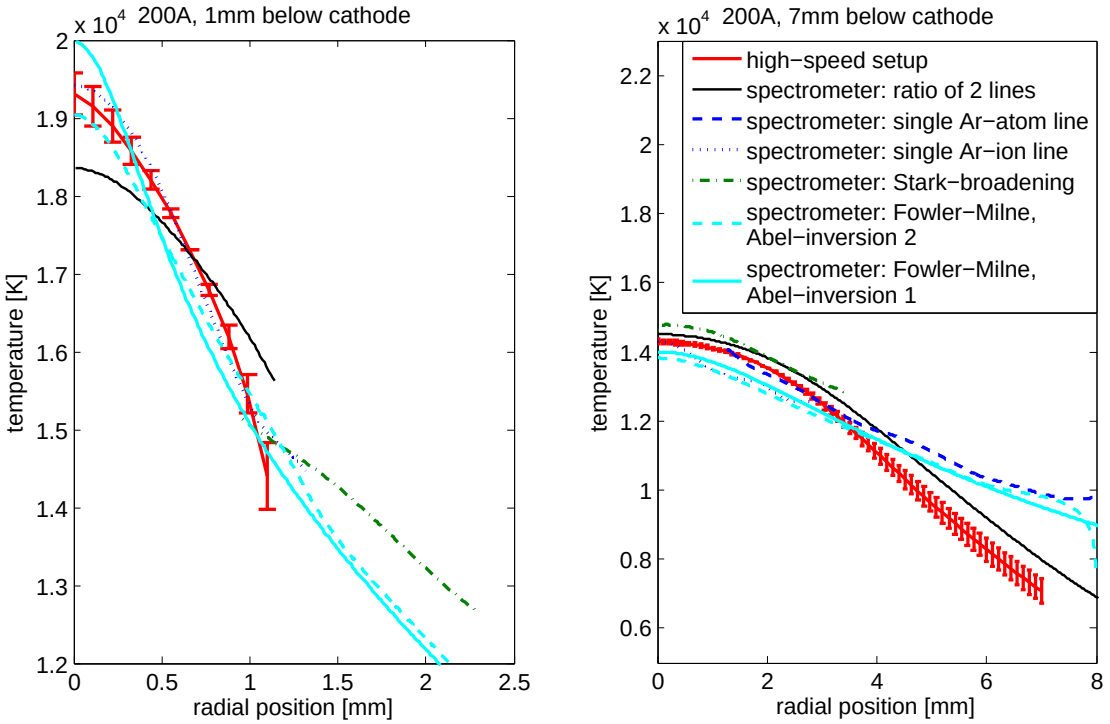

Figure 3.11: Comparison of plasma temperature measurements of a stationary free burning Argon arc operated at $200\,\mathrm{A}$ evaluated with *Methods 1 to 5* (Table 3.1). Error bars are given for results from *Method 1*. Results are shown at $1\,\mathrm{mm}$ and $7\,\mathrm{mm}$ below the cathode.

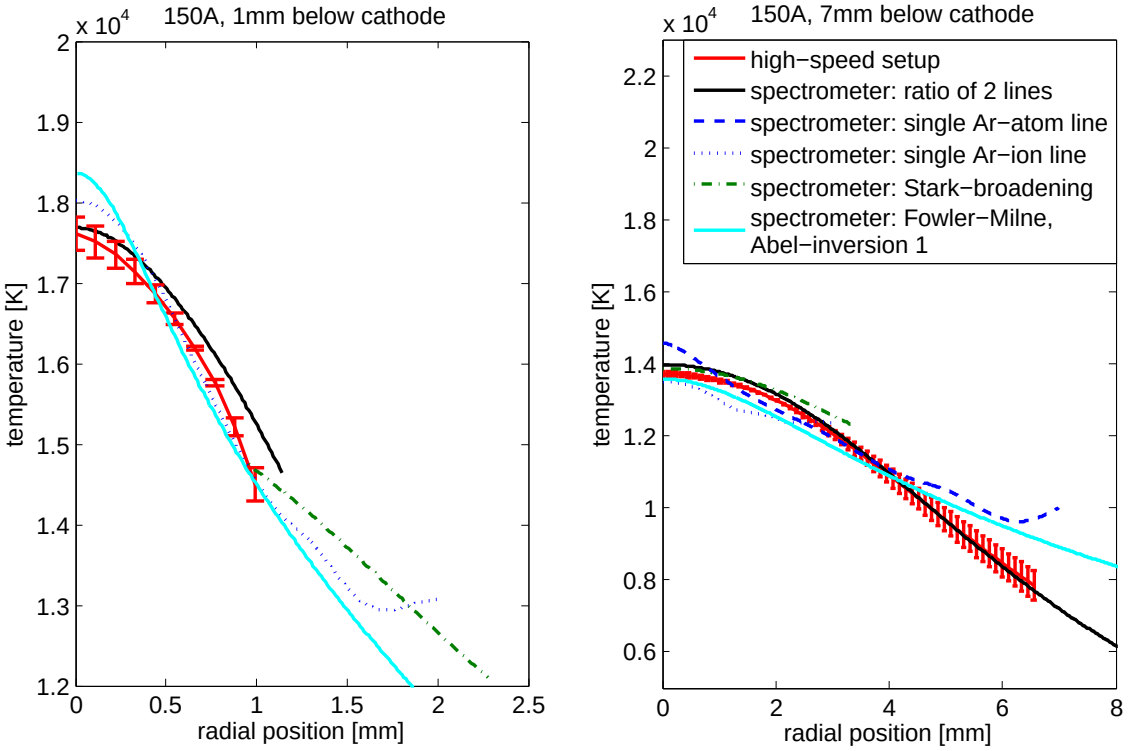

Figure 3.12: Comparison of plasma temperature measurements of a stationary free burning Argon arc operated at $150\,\mathrm{A}$ evaluated with *Methods 1 to 5* (Table 3.1). Error bars are given for results from *Method 1*. Results are shown at $1\,\mathrm{mm}$ and $7\,\mathrm{mm}$ below the cathode.

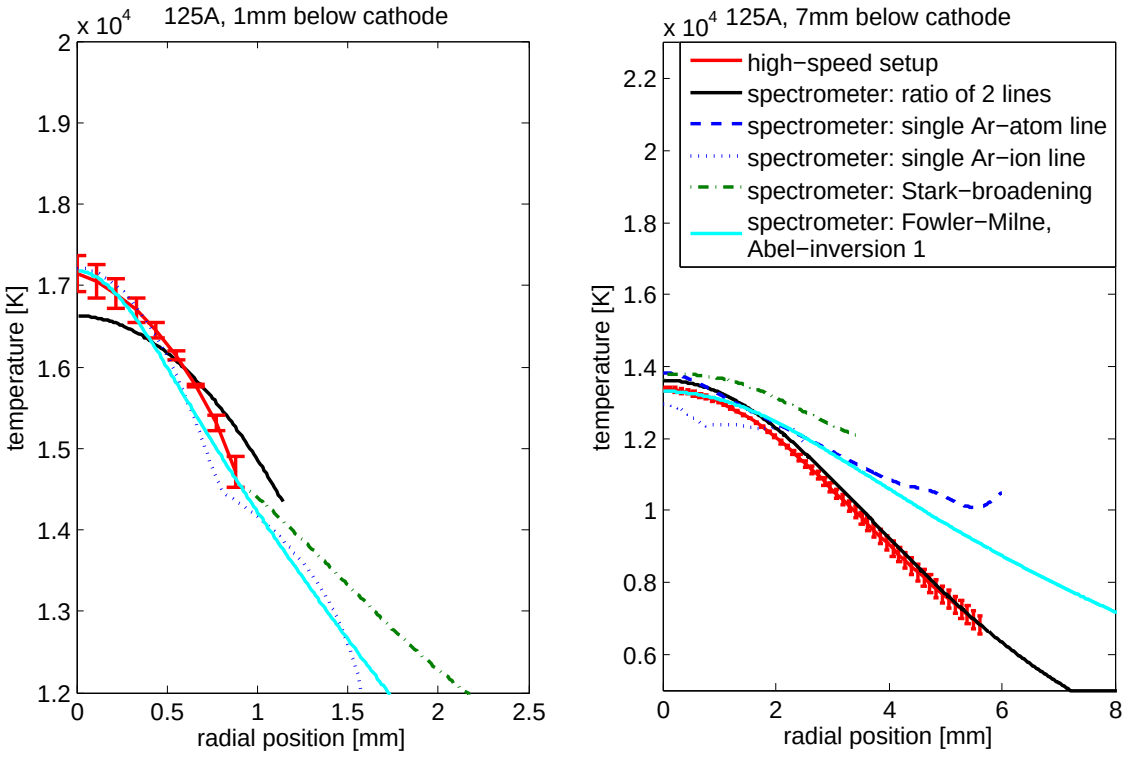

Figure 3.13: Comparison of plasma temperature measurements of a stationary free burning Argon arc operated at $125\,\mathrm{A}$ evaluated with *Methods 1 to 5* (Table 3.1). Error bars are given for results from *Method 1*. Results are shown at $1\,\mathrm{mm}$ and $7\,\mathrm{mm}$ below the cathode.

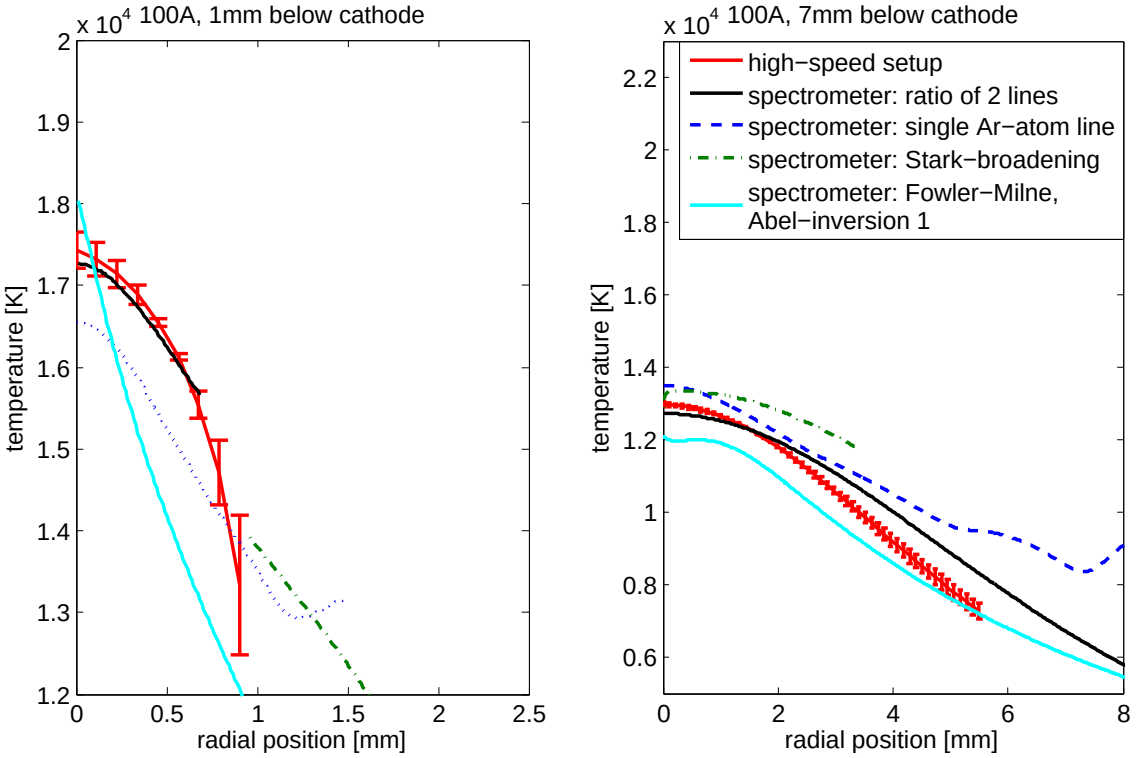

Figure 3.14: Comparison of plasma temperature measurements of a stationary free burning Argon arc operated at $100\,\mathrm{A}$ evaluated with *Methods 1 to 5* (Table 3.1). Error bars are given for results from *Method 1*. Results are shown at $1\,\mathrm{mm}$ and $7\,\mathrm{mm}$ below the cathode.

3.7 Results of related plasma parameters and transient plasma processes

It is also possible to measure three-dimensional density and conductivity distributions with the introduced high-speed setup (Figure 3.1) and evaluation with *Method 1* (Table 3.1): Figure 3.15 shows electron densities and densities of atomic species for currents of 100 to 200 A. The corresponding electrical conductivities for each el. current can be found in Figure 3.16. A brief summary of how to estimate the order of magnitude of the electrical conductivity is given in Appendix A. However, for this work the derivations given by Boulos *et al.* [15] have been employed for calculating the electrical conductivity.

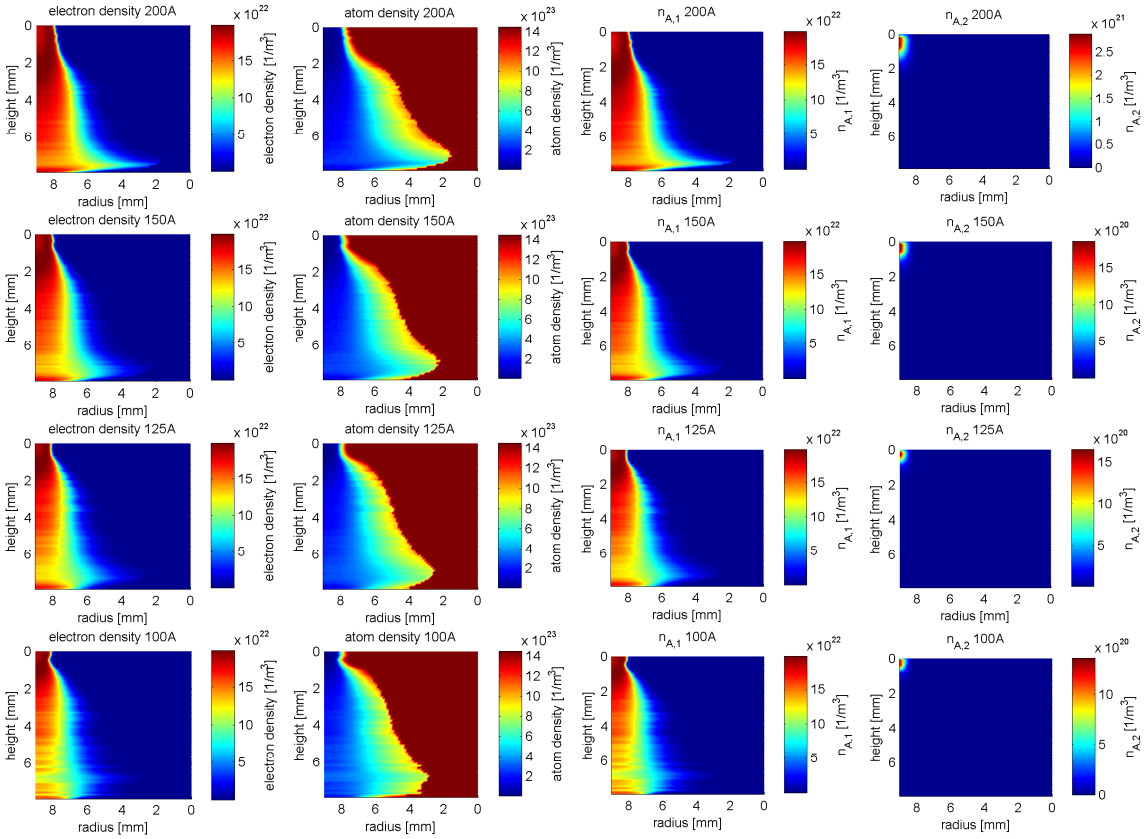

Figure 3.15: Plasma density distributions of a free burning Argon arc operated from 100 to 200 A.

'A transient plasma process was investigated with the high-speed setup and evaluated with *Method 1*. The process was started with a current of 75 A which was then increased to 200 A and subsequently reduced to 100 A. The current was measured with a calibrated Hall-effect device (Honeywell SS94A1F) and is displayed qualitatively in Figure 3.17 together with the quantitative plasma temperature evolution 2 mm below the cathode on the arc axis. The arc was recorded with a frame rate of 33000 fps in this experiment. The evolution of the plasma temperature shows that transient plasma temperature measurements are possible with the introduced setup featuring a low noise of around ± 20 K above 16000 K. An evaluation of isothermals shows the quantitative impact of the electrical current on the arc radius as a function of time (displayed in Figure 3.18). This displayed radial and temporal evolution of the plasma temperature allows to measure the modulation of the arc. This determines the arc footprint which - e.g. in the case of welding processes - is an

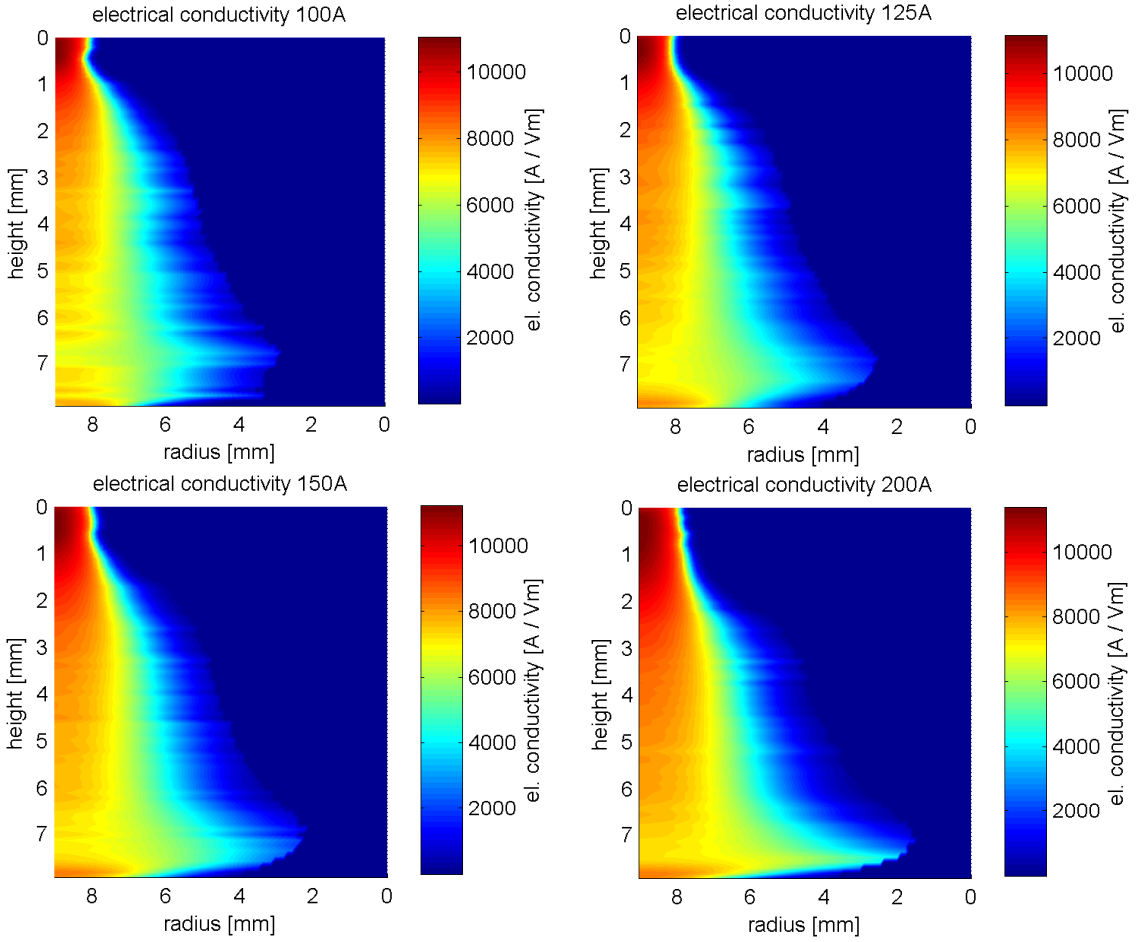

Figure 3.16: Electrical conductivity distribution of a free burning Argon arc operated from 100 to 200 A.

important measure for the weld pool heating as well as the weld pool geometry.

3.8 Error sources, measurement uncertainties and limits of applicability

Every measurement is accompanied with uncertainties. The errors resulting from these uncertainties can be grouped in two categories: random errors and systematic errors. The former are e.g. due to noise of the electronic equipment, namely the discretization error made by the camera when an analog value of radiation gets discretized and converted to a gray scale value. The latter can be for example due to incorrect model assumptions. A departure of the plasma from LTE or strong absorption of the analyzed wavelengths would lead to systematic errors. Random and systematic errors that were considered in this work will be discussed subsequently and show also the limits of applicability of the introduced diagnostic.

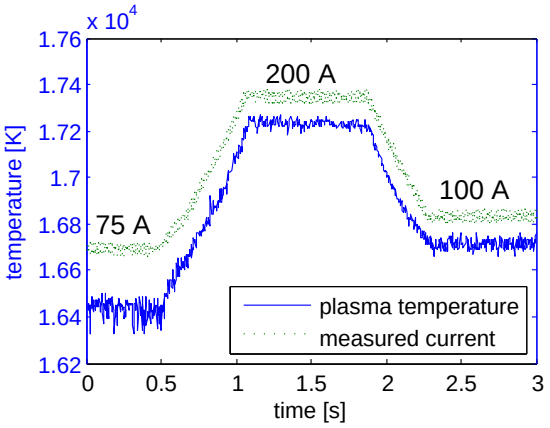

Figure 3.17: Plasma temperature evolution of an unsteady free burning Argon arc 2 mm below the cathode on the arc axis and corresponding electrical current signal.

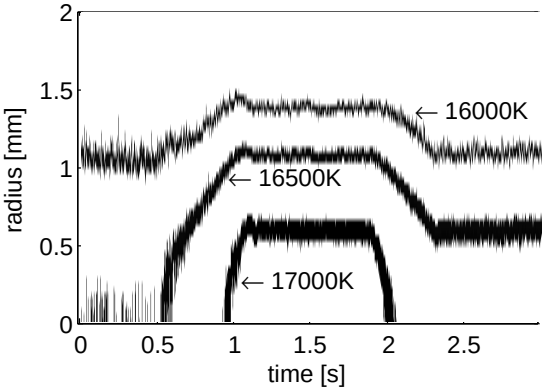

Figure 3.18: Radial plasma temperature changes 2 *mm* below the cathode show impact on arc radius.

3.8.1 Random errors

The discretization error made by digital cameras leads to an error of the measured radiance $I_\lambda(y)$. The resulting error on measured plasma temperatures can be calculated by error propagation through the employed Abel inversion algorithms (introduced in section 3.4) and the performed plasma composition calculations as well as calculations of emission coefficients (introduced in section 3.3). (An additional error can occur due to the employed Abel inversion algorithm itself when e.g. a non-linear least squares fit is applied on measured radiance profiles (see section 3.8.5).) The uncertainty in temperature ΔT due to an uncertainty in emission coefficient $\Delta\varepsilon_\lambda$ which is directly correlated with the uncertainty in the excited atom density Δn_u (equation 3.28) will be derived subsequently. The temperature uncertainty ΔT which is a non-linear function of n_u (equation 3.30) writes:

$$\Delta T = \frac{dT}{dn_u}\Delta n_u = \left(\frac{dn_u}{dT}\right)^{-1}\Delta n_u, \tag{3.54}$$

where dn_u/dT follows from equation 3.30:

$$\frac{dn_u}{dT} = n_u\left(\frac{1}{n_A}\frac{dn_A}{dT} + \frac{E_u}{kT^2} - \frac{1}{Z_A}\frac{dZ_A}{dT}\right). \tag{3.55}$$

Thus the uncertainty in temperature is proportional to the uncertainty in the excited atom density:

$$\Delta T = \left(\frac{1}{n_A}\frac{dn_A}{dT} + \frac{E_u}{kT^2} - \frac{1}{Z}\frac{dZ_A}{dT}\right)^{-1}\frac{\Delta n_u}{n_u}. \tag{3.56}$$

Considering for example the 696.54 nm Argon atom line, the sum in parenthesis in equation 3.56 changes from $\approx 2\times10^{-3}\,\mathrm{K}^{-1}$ to $\approx 2\times10^{-4}\,\mathrm{K}^{-1}$ if temperature changes from 8000 K to 14000 K. Thus an uncertainty in emission coefficient of $\pm10\%$ would yield an uncertainty of e.g. ±50 K at a temperature of 8000 K and an uncertainty of ±500 K at a temperature of 14000 K.

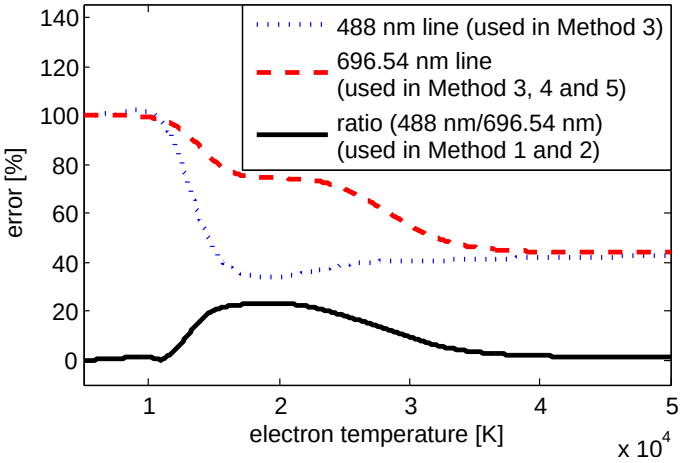

Figure 3.19: Error of calculated emission coefficients and ratios if LTE changes from *single temperature LTE* ($\theta = 1$) to a *two temperature LTE* with $\theta = 2$.

3.8.2 LTE consideration

As already mentioned, a deviation from local thermodynamic equilibrium (LTE) is a source of systematic error. To quantify the nature of this error a definition of LTE is given subsequently by distinguishing between '*single temperature LTE*' and '*two temperature LTE*'. The former means:

- single local temperature for all atomic species (atoms and ions) and electrons,
- ionization equilibrium (Saha equation),
- population of each discrete energy level according to a Boltzmann distribution with a single temperature.

The difference to *two temperature LTE* is that in the latter case the plasma exhibits an electron temperature T_e and an heavy species temperature T_h which are connected via $\theta = T_e/T_h$. However an ionization equilibrium and a Boltzmann distributed energy population remains. In a *single temperature LTE* plasma the value for θ equals 1. If the value for θ changes to e.g. $\theta = 2$ the systematic error that is induced in the calculation of emission coefficients (section 3.3.3) can be calculated by computing the deviation of resulting emission coefficients from original ones. This has been done for the wavelengths utilized in *Methods 1-5* (Table 3.1) where the errors are displayed in Figure 3.19. In the temperature regime below 10000 K, which can be found in the outer regions of an arc, a departure from *single temperature LTE* very likely may occur [30, 29, 19, 7]. While the error of the methods which evaluate only a single spectral interval or line (*Methods 3-5*) is in the range of 100% in this region, the error of *Methods 1-2* (line-ratio methods) is less than 2% in this case. Hence the developed high-speed setup yields accurate electron temperatures (assuming a *two temperature LTE*) by experimentally enabling the evaluation with a line ratio method as against in *Methods 3-5*, where a departure from *single temperature LTE* leads to an over- or under-estimation of the electron temperature. More precisely the electron temperature is overestimated if it is lower than 25000 K or 15000 K for the 488 nm Argon ion line or the 696.54 nm Argon atom line, respectively, which follows from Figure 3.8. This overestimation of temperatures is also visible in Figures 3.11-3.14 for the outer regions of the arc which are around 10000 K and lower.

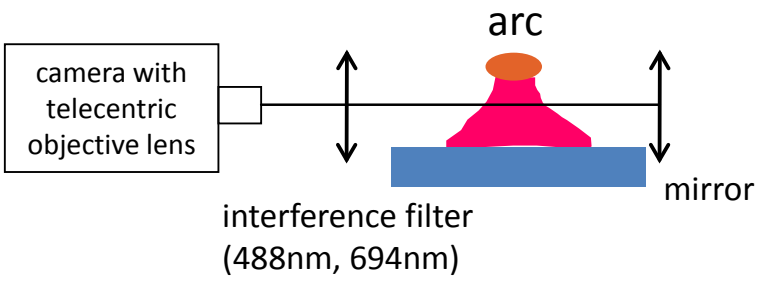

Figure 3.20: Experimental setup for test of optical thickness.

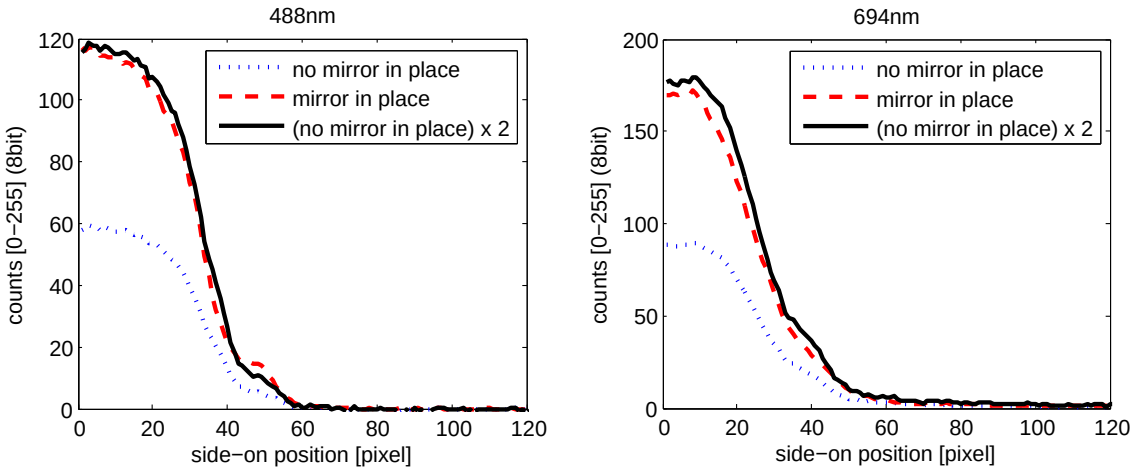

Figure 3.21: Comparison of measured intensities at 488 nm (left) and 694 nm (right). The solid line corresponds to twice the radiation measured without a mirror.

3.8.3 Measurement of optical depth

Another systematic error source is the assumption of optical transparency of the arc plasma in the utilized wavelength regimes. An optically thick plasma would lead to errors in calculation of measured emission coefficients because the Abel inversion is based on the assumption of optical transparency. For most cases in free burning Argon arcs the 696.54 nm Argon atom line can be considered to be optically thin [78]. The same applies also for the 488 nm Argon ion line. The optical transparency of the wavelength intervals which are transmitted through the employed filters of the high-speed setup (Figure 3.1) has been experimentally verified. A camera equipped with a telecentric lens was utilized to measure horizontal arc radiation passing through each bandpass dichroic filter. In a next step a mirror is placed in the line-of-sight of the camera / filter and reflects arc radiation back through the plasma on the camera chip. What is to be expected is that if the radiation measured with a mirror in place is twice as high as without, the plasma can be considered to be optically thin. A schematic of the setup is displayed in Figure 3.20. Accounting for the reflectivity of the mirror, the discretization noise of the camera and a maximum magnification error, the transparency of the arc can be calculated subsequently. Figure 3.21 shows a comparison of measured radiations for both filters. In order to determine the absolute transmittance, radiation emitted by the center point of the arc which is coinciding with the center of the telecentric lens is evaluated. In this manner remaining aberrations are minimized. The resulting values for the optical transparency of the plasma are $96 \pm 5\%$ for the 488 nm filter and $94 \pm 5\%$ for the 694 nm filter.

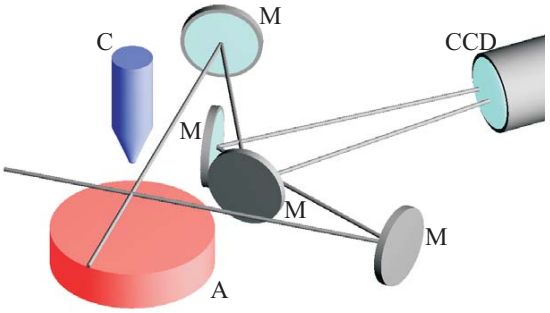

Figure 3.22: Experimental setup for validation of axial symmetry (C: cathode, A: anode, M: mirror, CCD: charge-coupled device).

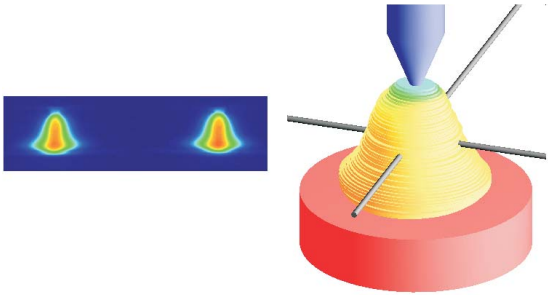

Figure 3.23: False color photography of a typical arc from two orthogonal directions (left); reconstructed three-dimensional image of the arc (right).

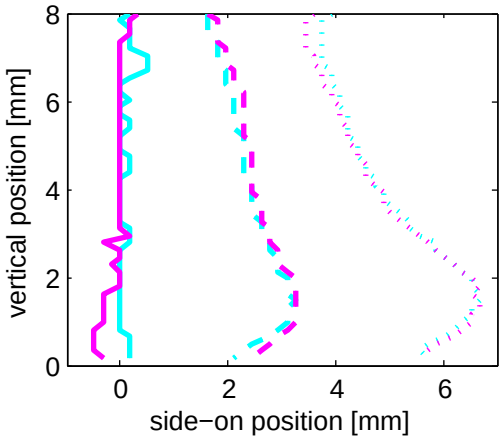

Figure 3.24: Data evaluated from the left (cyan) and the right image of the arc (magenta): locations of the axial intensity maxima (solid lines), arc width at 68.3 % and 25 % of the axial intensity maxima (dashed and dotted lines, respectively).

3.8.4 Measurement of axial symmetry

Another assumption which is made in order to apply an Abel inversion is axial symmetry of the arc plasma. More precisely if the arc is subdivided in arbitrary horizontal layers, each layer has to be axially symmetric. (Note that this is a slight attenuation of an overall axial symmetry since in this case the maximum of intensity can deviate from the central arc axis to some degree without disturbing the axial symmetry of each horizontal layer.) The axial symmetry of the investigated arcs has been validated with a modified setup of mirrors and a camera. Figure 3.22 shows a schematic of this setup which allows imaging the arc from two orthogonal lines-of-sight simultaneously on a single camera chip. For each horizontal pixel row the deviation from the arc axis can be calculated. Additionally, ellipses can be calculated from the two orthogonal views and a three-dimensional image of the arc can be reconstructed (see Figure 3.23). A quantitative evaluation of the raw images is displayed in Figure 3.24 where the isoline of the maximum of intensity (solid line) is plotted for the left (cyan) and the right (magenta) side-on position. Here the arc widths at 68.3% (dashed) and 25% (dotted) of the maximum intensity show the axial symmetry of the arc.

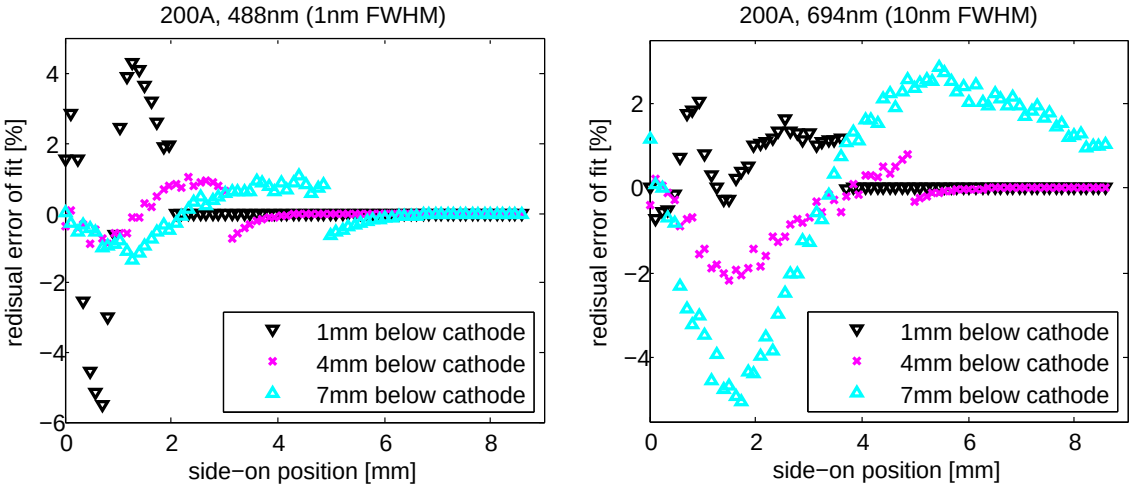

Figure 3.25: Comparison of residuals for the $488\,\mathrm{nm}$ interval at three different side-on positions (left). Comparison of residuals for the $694\,\mathrm{nm}$ interval at three different side-on positions (right).

3.8.5 Errors induced by Abel-inversion

Abel inversion method 1

The first introduced method for the employed Abel inversion makes use of a non-linear least squares fit in order to fit measured radiances to an implied physical model function (section 3.4). Since the subsequent inversion is analytical, the error which occurs during calculation of emission coefficients is only due to error propagation of the confidence interval of the fit result. 68.3% confidence intervals and the discretization error of the 12 bit monochrome high-speed camera have been used for the error propagation and yield error bars for the resulting plasma temperatures as depicted in Figures 3.11 to 3.14. Here error bars on the central arc axes for all evaluated plasma currents yield maximum values of $\pm 270\,\mathrm{K}$ (1 mm below the cathode) and $\pm 70\,\mathrm{K}$ (1 mm above the anode). Error bars which are calculated off-axis and in the outer regions of the arc yield higher values. This has mainly two reasons: First, since temperatures decrease towards the outer regions of the arc, the gradient $d\varepsilon_\lambda/dT$ also decreases (compare Figure 3.8) which reduces accuracy. Second, the residuals of the non-linear least squares fits decrease which can be seen in Figure 3.25. Errors due to the fit procedure were minimized by optimizing bounds to the fit parameters in order to yield minimum residuals in the outer regions of the arc and on the central arc axis (see Figure 3.25). An upper and lower bound was calculated for each wavelength window for the error propagation of the line ratio method employed with the high-speed measurements. Those bounds yielding a maximum error were selected for the calculation of emission ratios $\alpha(r,z)$ in order to prevent error compensation.' [4]

Abel inversion method 2

Abel inversion method 2 makes use of spline interpolation [17] with a third order piecewise polynomial which is subsequently projected to the radiance by inversion (equation 3.42). Therefore a test procedure was developed which is described in what follows. Several test profiles for the emission coefficient were chosen. The side-on profiles were calculated according to equation 3.42. A random noise signal with 10% amplitude was added to

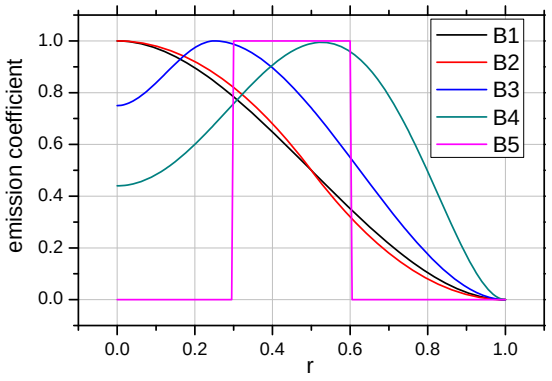

Figure 3.26: Test profiles for the inversion procedure.

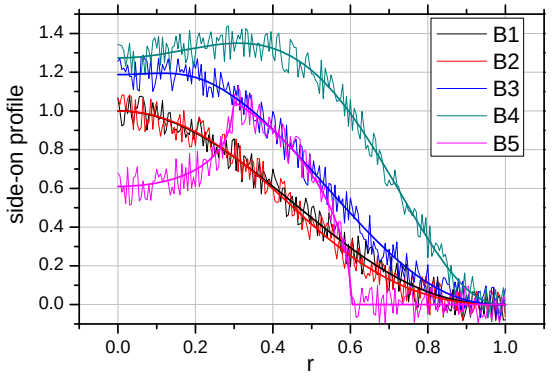

Figure 3.27: Side-on profiles calculated from emission coefficient according to equation 3.42 (thick lines) and those with added random noise 10% in amplitude (thin lines).

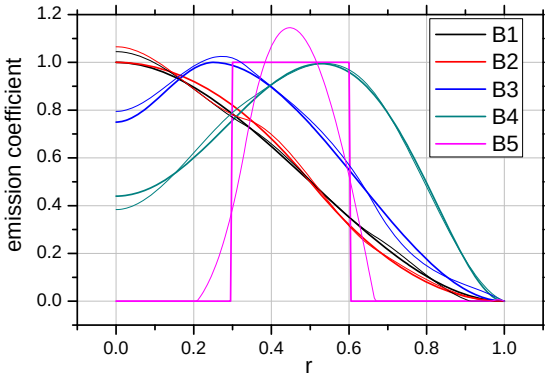

Figure 3.28: Results of Abel inversion.

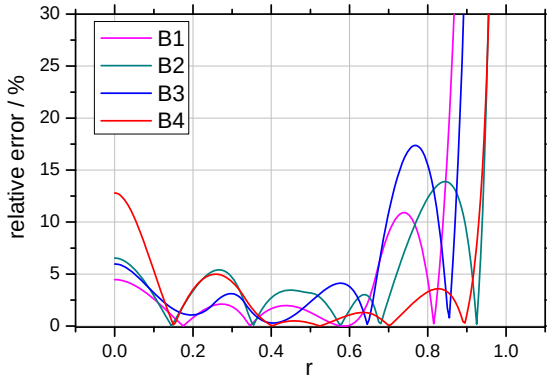

Figure 3.29: Relative error between real and restored profiles expressed in $\%$.

these profiles. The result was inverted by the procedure described in section 3.4.2 and the restored emission coefficient profiles were obtained. Five test profiles of emission coefficients were chosen for test purposes. Four of them (B1 – B4) are taken from [64]. One additional hollow-shell profile (B5) was also used. The emission coefficient profiles are shown in Figure 3.26. The corresponding side-on profiles with and without noise are shown in Figure 3.27. Results of inversion procedures using four spline knots and their comparison with the initial profiles are shown in Figure 3.28. The relative error calculated as difference between restored and initial profile related to the initial profile is plotted in Figure 3.29. The difference between initial and restored profiles is smaller than 20% up to a radius of 0.8. In the outer regions the absolute error remains the same, but due to the smaller amplitude the relative error increases. An important feature of the inversion procedure described in section 3.4.2 is the ability to propagate the uncertainties and calculate error bars (see Figure 3.30). The error calculation in non-linear least squares will be briefly described in Appendix B.

'Employing the error propagation during the non-linear least squares procedure, uncertainties of the model parameters δa_i and $\delta a_i'$ can be obtained which will be named $\Delta\vec{a}$ in the following. These uncertainties are connected to the coefficients of the polynomial $\vec{b_k}$ through the linear equation 3.48 with the solution $\vec{b_k} = \hat{R_k}^{-1}\vec{a}$. The polynomial coefficient b_{jk} which is defined between the spline knots k and $k+1$ is a linear combination of a_i and

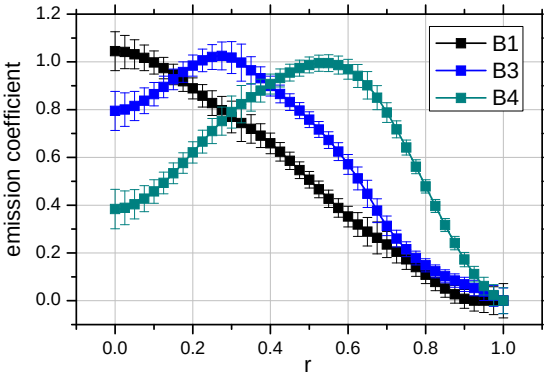

Figure 3.30: Restored profiles with error bars

a'_i:

$$b_{jk} = d_{j0}a_k + d_{j1}a'_k + d_{j2}a_{k+1} + d_{j3}a'_{k+1}, \tag{3.57}$$

where d_{ji} are the elements of matrix $\hat{R}_k^{-1}$, $j \in [0,3]$. The uncertainty of b_{jk} follows from the connection with uncertainties of $\vec{a}$:

$$\Delta b_{jk} = \sqrt{(d_{j0}\Delta a_k)^2 + \left(d_{j1}^2\Delta a'_k\right)^2 + \left(d_{j2}^2\Delta a_{k+1}\right)^2 + \left(d_{j3}^2\Delta a'_{k+1}\right)^2}. \tag{3.58}$$

Finally the uncertainties of the emission coefficients can be calculated from the uncertainties of the polynomial coefficients $\Delta\vec{b}_k$:

$$\Delta\varepsilon_{\lambda,k}(r) = \sqrt{(r-r^*)^6\Delta b_{3k}^2 + (r-r^*)^4\Delta b_{2k}^2 + (r-r^*)^2\Delta b_{1k}^2 + \Delta b_{0k}^2}. \tag{3.59}$$

' [4].

The introduced *Abel inversion method 2* unites two steps generally used in Abel inversion algorithms – smoothing and inverse transformation. This is achieved by using smooth functions as the least squares model. Nevertheless this model does not put strict limitations on the profile types. Almost any profile could be restored. The data in Figures 3.28 and 3.29 show that the inversion procedure gives good results in restoring smooth profiles (B1–B4) while only qualitatively acceptable result for rectangular profile B5 is obtained. It should be noted that the number of spline knots was kept constant (4 knots). On the one hand the larger number of knots gives the possibility to restore the profiles with steeper changes but on the other hand it diminishes the smoothing ability of the method. Thus empirically optimal minimal number of knots should be chosen based on the quality of experimental data. Another option would be to increase the number of knots starting from the minimal number of 2 until the stop criterion, like for example minimal successive reduction of squared differences S (equation 3.49) is not fulfilled. Another possibility of further improvement of the algorithm is a non-uniform knots distribution. One would place more knots there, where the curvature of the measured profile is higher. The non-linear least squares technique used in the algorithm allows conditioning on the fitted parameters. This gives the possibility to use physically based conditions like for example non-negativity of the emission coefficient or zero derivative at the center.

λ	A_{ud}	Acc.	$\varepsilon_\lambda = \varepsilon_\lambda^{fb} + \varepsilon_\lambda^{ffi} + \varepsilon_\lambda^{bb}$			$\varepsilon_\lambda^c = \varepsilon_\lambda^{fb} + \varepsilon_\lambda^{ffi}$			$\frac{\varepsilon_\lambda^{bb}}{\varepsilon_\lambda}$		
		[55]	10kK	15kK	20kK	10kK	15kK	20kK	10kK	15kK	20kK
[nm]	[s^{-1}]		[$Wm^{-3}sr^{-1}$]			[$Wm^{-3}sr^{-1}$]			[%]		
487.6261	7.8e5	D	1.6e3	1.2e5	7.8e4	2.0e2	2.4e4	2.1e4	88	80	73
487.9863	8.23e7	A	2.0e2	1.5e5	5.3e6	2.0e2	2.3e4	2.1e4	2.55	84.0	99.6
688.7088	1.3e5	D+	5.1e2	3.5e4	2.4e4	9.9e1	1.2e4	1.1e4	81	65	52
688.8174	2.5e5	D+	6.8e2	4.4e4	2.9e4	9.9e1	1.2e4	1.1e4	85	72	60
692.5009	1.2e5	D+	2.4e2	2.0e4	1.6e4	9.8e1	1.2e4	1.1e4	58	40	28
693.7664	3.08e6	C	2.0e3	1.1e5	6.0e4	9.8e1	1.2e4	1.1e4	95	89	81
695.1477	2.2e5	D	6.0e2	4.0e4	2.6e4	9.8e1	1.2e4	1.1e4	84	70	57
696.0250	2.4e5	D	6.5e2	4.3e4	2.8e4	9.7e1	1.2e4	1.1e4	85	71	59
696.5430	6.39e6	C	5.8e4	1.7e6	6.8e5	9.7e1	1.2e4	1.1e4	99.8	99.3	98.4

Table 3.2: Overall emission coefficients ε_λ, continuum emission coefficients ε_λ^c, contribution of line emission ε_λ^{bb} to overall emission and accuracies of line transition probabilities (Acc.) for utilized wavelengths according to NIST. The emission coefficients are given for a spectral interval of $\Delta\lambda = 0.2\,\mathrm{nm}$ around each wavelength λ.

3.8.6 Influence of line and continuum emission on overall emission and accuracies of utilized transition probabilities

'The plasma composition and emission coefficient calculations (section 3.3) are prone to uncertainties due to model assumptions. A systematic error involved in these calculations is based on the accuracy of values for the transition probability provided by the NIST compilation of lines [55]. The wavelengths of line radiation employed in this work are shown together with their accuracies in Table 3.2. In order to evaluate the impact of these accuracies on the overall emission coefficient ε_λ the influence of the line emission coefficient ε_λ^{bb} to the overall emission coefficient ε_λ has been analyzed with respect to the continuum emission coefficient $\varepsilon_\lambda^c = \varepsilon_\lambda^{ffi} + \varepsilon_\lambda^{fb}$. Table 3.2 shows emission coefficients for three different temperatures (10000, 15000 and 20000 K) and each employed wavelength of line radiation as well as the contribution of line emission coefficient to the overall emission coefficient ($\varepsilon_\lambda^{bb}/\varepsilon_\lambda$) for a spectral interval of $\Delta\lambda = 0.2\,\mathrm{nm}$. For spectroscopic measurements or simulations with a different spectral resolution the continuum emission coefficient ε_λ^c can be recalculated for other spectral intervals $\Delta\lambda_{\mathrm{new}}$ by the following formula:

$$\varepsilon_{\lambda\mathrm{new}}^c = \varepsilon_\lambda^c \cdot \frac{\Delta\lambda_{\mathrm{new}}}{\Delta\lambda}. \tag{3.60}$$

The influence of the line emission coefficient on the overall emission coefficient has been analyzed also for the filters employed in this work. Here the spectral intervals of filter transmission are $\Delta\lambda_{488\mathrm{nm}} = 1\,\mathrm{nm}$ and $\Delta\lambda_{694\mathrm{nm}} = 10\,\mathrm{nm}$. Figure 3.31 shows the ratio of ε_λ^{bb} to ε_λ where higher values of $\varepsilon_\lambda^{bb}/\varepsilon_\lambda$ result in a higher impact of uncertainties of A_{ud} on ε_λ than zones of lower values of $\varepsilon_\lambda^{bb}/\varepsilon_\lambda$.

3.8.7 Error sources due to the design of the experimental setups

An error source which has already been mentioned is the discretization error occurring when a camera converts radiance to a gray scale value. This discretization error has been evaluated for the 12 bit camera (PCO.dimax) by changing the measured gray scale values by one and recalculating the plasma temperature with these altered values. As a result

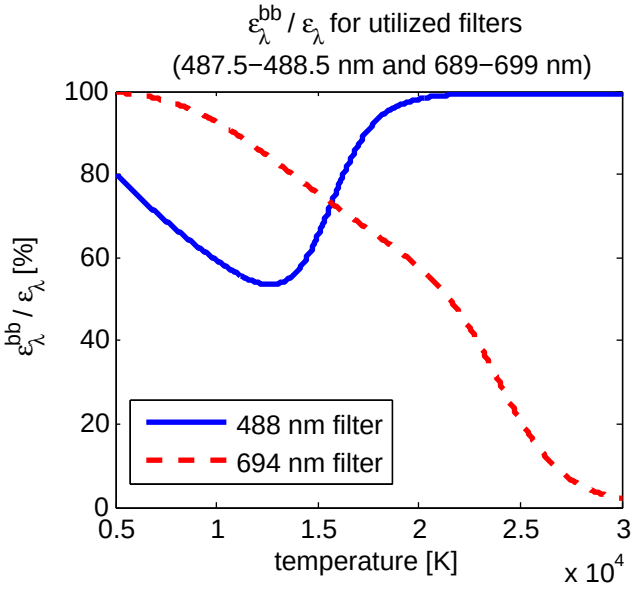

Figure 3.31: Contribution of line emission for the spectral filters utilized in the experimental setup of Method 1 (see Figure 3.1).

the influence of the discretization error can be neglected since deviations from original plasma temperatures are not visible (below calculated resolution of 10 K).

Another possible error source that could affect results obtained with the high-speed setup is due to the wavelength dependence of the utilized interference filters. The filters' central wavelengths are sensitive to the angle between the filter surface and the optical path direction. Hence the optical setup was adjusted by aligning the partial reflection and transmission of a laser beam with the optical path of the setup.

Measurements of plasma parameters were performed in a non-controlled ambient laboratory atmosphere. Possible mixing of the Argon plasma with ambient air was not considered in this work. However such a mixing and resulting dissociation/ionization of air molecules and atoms would lead to additional radiation which would affect the plasma composition calculations.

3.8.8 Error summary

Another classification of errors which affect the plasma temperature measurements is a division in errors due to model assumptions and errors leading to variations of emission coefficients. A list of the latter that have been analyzed in this work is provided below:

- Abel inversion
- Optical depth
- Axial symmetry
- Transition probabilities
- Experimental design

While these error sources can result in uncertainties up to several tens of per cent in the emission coefficient, errors caused by model assumptions can be mainly induced by deviations of an LTE plasma. Here the introduced three-dimensional high-speed method (*Method 1*) has the advantage that deviations of *single temperature LTE* to *two temperature LTE* with $\theta = 2$ still yield correct electron temperatures (with respect errors shown in Figure 3.19) while *Methods 3 - 5* are prone to larger errors. Finally, the exponential dependency between emission coefficient and temperature (see section 3.3.3) yields a significant reduction of the relative error induced in the plasma temperature calculations (see equation 3.56).' [4]

PART 2

Chapter 4

A diagnostic to measure three-dimensional current density distributions in axially symmetric free burning arcs by means of Hall effect devices

4.1 Introduction

'Numerous plasma technologies, especially those employed for material treatment purposes, like welding or plasma spraying are based on a reproducible application of electric arcs. Such arcs are nevertheless prone to instabilities, the control of which requires better understanding of the interaction between the arc and several operating parameters like electric current, gas flow and electrode condition. This goal can only be achieved if detailed diagnostic techniques are available, which preferable do not modify the arc to be investigated.

One of the key parameters inside a current conducting plasma, which is especially interesting for material science as well as fusion application is the current density. Knowledge of the current density close to the electrodes in a transferred arc has a direct impact on controlling material treatment. The first requirement for developing a diagnostic tool to measure current density in an industrial environment is that the process should not be disturbed; therefore a non-intrusive system is needed. So far various non-intrusive methods to determine the current density inside a plasma have been developed [11, 16, 74, 77, 93, 94, 96] and most of them could be applied to technical thermal plasmas as well. These techniques include Thomson scattering, magnetic probe, Langmuir probe, Faraday rotation and gas pressure measurements, as well as the measurement of the current through a split electrode. However, some of these like Thomson Scattering, where a localized measurement of electron density and drift velocity results in direct measurement of current density through $j = nev$ [11], require fairly stable plasma conditions due to the small scattering cross section [41]. Others like the measurement of the B-field induced Faraday rotation using FIR lasers are significantly faster [16, 65] but require an optically thin plasma. Such optical thin plasmas can only be found in some applications with the restriction to certain optical thin wavelength intervals, like in the free burning Argon arc (see section 3.8.3 of the first part of this thesis).

Another possibility would be the use of electric or magnetic probes inside the plasma which involves several advantages compared to the other named methods. Such probing techniques allow a closer evaluation of parameters like the electric current density inside a plasma [50]. However, these direct probing techniques have other limitations. One obvious drawback is the perturbation occurring by moving the probe inside the plasma. Thermal cooling effects that change the energy properties of the plasma and the possibility of probe-injected impurities are major concerns. Langmuir probes can be manufactured with diameters in the micrometer range but are delicate to handle and require a lot of experience if reasonable and reproducible results are needed. Additionally, the use of

such probes in thermal plasmas is challenging due to the high atom and ion temperatures. Those temperatures which reach values above 5000 K easily destroy the probes if not handled with precautions such as short exposure times. Thus the most frequently used diagnostic so far is the spatially resolved spectroscopic measurement of the electron temperature and subsequent conversion into resistivity [4, 97, 101]. This application is limited due to its highly sensitive experimental apparatus and the quite involved analysis of the selected line shapes, which requires detailed information about the plasma medium, which is not easily obtainable for gas compositions used in industry or even metal vapor. Another limitation of optical emission spectroscopy is the availability of optically thin spectral bands, or at least knowledge about their absorption characteristics.

This chapter deals with another measurement principle, which utilizes magnetic probes to map the B-field outside the main plasma. While this technology has been used in the past mostly for Tokamak plasmas employing B-dot probes [93, 94] this section will introduce the use of Hall probes to measure the magnetic field and determine the current density close to a free burning arc by application of Ampere's law. The magnetic flux density measurements were made in the vicinity of the main plasma column where the current density did not vanish to zero yet. The results obtained will be compared to optical measurements verifying the axial symmetry of the resulting current density.' [5] Additionally, measured current density distributions will be compared to the electrical conductivity measurements which have been presented in Chapter 3. This comparison validates the newly developed diagnostics and confirms the physical phenomena at work.

4.2 A general and simplified approach for the reconstruction of current density distributions

A direct relation between the magnetic flux density $\vec{B}$ and the electric current density distribution $\vec{j}$ is given by Maxwell's equations. More precisely Ampere's circuital law connects $\vec{B}$ and $\vec{j}$ in the absence of a displacement current [1]. In the following a discretization of Ampere's law will be derived since $\vec{B}$ will be measured on discrete positions. Hence an approach will be deduced to isolate arbitrary intersections of current (Figure 4.1). Subsequently a simplified approach for axially symmetric systems will be discussed. Therefore a Gaussian profile for j_z will be assumed and a model will be developed to relate $\vec{B}$ to the standard deviation σ of the Gaussian profile. This relation can be employed to derive the components of the electric current density distribution j_z and j_r.

4.2.1 General approach for the reconstruction of current density distributions

'The general approach is based on the integral form of Ampere's law:

$$\frac{1}{\mu_0} \oint_{\text{contour}} \vec{B} \cdot d\vec{s} = \iint_{\text{surface}} \vec{j} \cdot d\vec{A}, \tag{4.1}$$

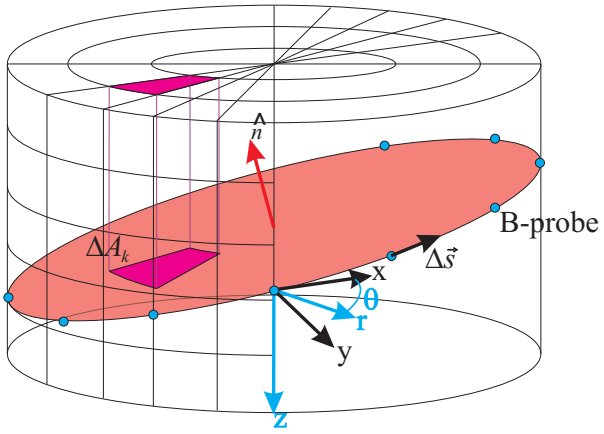

Figure 4.1: Measurement volume with orientation vector $\hat{n}$, tangent vector $\Delta\vec{s}$ and surface area ΔA_k of a tile of the k^{th} cross section.

with μ_0 the vacuum permittivity, $\vec{B}$ the magnetic flux density and $\vec{j}$ the current density distribution. A discretization of the left hand side of equation 4.1 yields:

$$\frac{1}{\mu_0}\oint_{\text{contour}} \vec{B}\cdot d\vec{s} \approx \frac{1}{\mu_0}\sum_{\text{circulation}} \vec{B}\cdot\Delta\vec{s}. \tag{4.2}$$

This sum can be evaluated experimentally by measuring the magnetic flux density $\vec{B}$ on a closed loop along the tangent vector $\Delta\vec{s}$. Thus the integrated current density distribution can be obtained within the cross section:

$$\frac{1}{\mu_0}\sum_{\text{circulation}} \vec{B}\cdot\Delta\vec{s} \approx \iint_{\text{surface}} \vec{j}\cdot d\vec{A}. \tag{4.3}$$

This integrated current density distribution can be also calculated by discretization:

$$\iint_{\text{surface}} \vec{j}\cdot d\vec{A} \approx \sum_{\substack{\text{tiles}\in k^{th}\\ \text{cross section}}} \vec{j}\cdot\hat{n}\Delta A_k, \tag{4.4}$$

where $\hat{n} = \begin{pmatrix}\sin\theta\cos\phi\\ \sin\theta\sin\phi\\ \cos\theta\end{pmatrix}$ is the orientation vector of the cross section and ΔA_k the surface area of the tiles which are defined by the intersection of the cross section and the corresponding volume element of the cylinder displayed in Figure 4.1. Hence a discretized form of Ampere's law is obtained:

$$\frac{1}{\mu_0}\sum_{\text{circulation}} \vec{B}\cdot\Delta\vec{s} \approx \sum_{\substack{\text{tiles}\in k^{th}\\ \text{cross section}}} \vec{j}\cdot\hat{n}\Delta A_k. \tag{4.5}$$

By experimentally collecting different cross sections across the current carrying plasma a linear system of such discretized Ampere's equations can be built. In order to be able to solve such a system of equations it has to be linearly independent. This means that each equation adds additional information to the system in such a way that the whole system has only one solution. A resulting open question is which kind of cross sections should be collected to solve this problem. Once a linearly independent system of equations with one

solution can be written, there exist several methods to solve it in a way that the solution converges towards the real solution. These are for example algorithms for linear equations or computed tomography. An outlook for this general approach will be given in section 4.6. However a relatively large number of measurements would be necessary for such a *B-probe tomograph*: Let's consider a transient arc and a tomographic setup with a radius of 30 mm and a height of 20 mm, as well as a sensor size of 4 mm. In order to measure the magnetic flux density at 40 positions around the arc (very 9 degrees) and at 5 heights per angle a total amount of $5 \cdot 40 = 200$ B-probes would be necessary to yield similar results to a simplified setup which is described in section 4.3.1. This favors the development of a simplified approach in order to show the feasibility and the suitability of this novel idea. Such a simplified approach will be discussed in what follows.

4.2.2 Simplified approach for the reconstruction of axially symmetric current density distributions

A simplification of the just described general approach can be made without loss of generality by assuming an axially symmetric arc and thus an axially symmetric current density distribution which can be written:

$$\vec{j}(r,\theta,z) = \begin{pmatrix} j_r(r,\theta,z) \\ j_\theta(r,\theta,z) \\ j_z(r,\theta,z) \end{pmatrix} = \begin{pmatrix} j_r(r,z) \\ 0 \\ j_z(r,z) \end{pmatrix}. \tag{4.6}$$

A relationship between such a current density and the magnetic flux density $\vec{B}$ is given by the law of Biot-Savart [14]. Their relation is defined by the magnitude, length, direction and distance of the vectorfield which describes the electric current density distribution. Defining $\vec{x} = (r,\theta,z)^{\mathrm{T}}$ to be the vector where the magnetic flux density is measured and $\vec{x}'$ the vector of the current density $\vec{j}(\vec{x}')$, the following vector product $\vec{j}(\vec{x}') \times (\vec{x} - \vec{x}')$ writes:

$$\vec{j}(\vec{x}') \times (\vec{x} - \vec{x}') = \vec{j}(\vec{x}') \times \left\{ \left[r - r' \cos(\theta - \theta') \right] \hat{r} + r' \sin(\theta - \theta') \, \hat{\theta} + (z - z') \, \hat{z} \right\} \tag{4.7}$$

$$\Rightarrow \vec{j}(\vec{x}') \times (\vec{x} - \vec{x}') = \begin{pmatrix} j_\theta (z - z') - j_z r' \sin(\theta - \theta') \\ -j_r (z - z') + j_z r - j_z r' \cos(\theta - \theta') \\ -j_\theta r + j_\theta r' \cos(\theta - \theta') + j_r r' \sin(\theta - \theta') \end{pmatrix}, \tag{4.8}$$

where, $\hat{r}$, $\hat{\theta}$ and $\hat{z}$ are the unit vectors of r, θ and z, respectively. This expression reduces in the case of axial symmetry to the following form:

$$\vec{j}(\vec{x}') \times (\vec{x} - \vec{x}') = \begin{pmatrix} -j_z r' \sin(\theta - \theta') \\ -j_r (z - z') + j_z r - j_z r' \cos(\theta - \theta') \\ j_r r' \sin(\theta - \theta') \end{pmatrix}. \tag{4.9}$$

Thus the Biot-Savart law can be applied yielding the magnetic flux density at each position $\vec{x}$ for an axially symmetric current density distribution:

$$\vec{B} = \mu_0 \iiint\limits_{\text{volume}} \frac{\vec{j}(\vec{x}') \times (\vec{x} - \vec{x}')}{4\pi \left|\vec{x} - \vec{x}'\right|^3} dV' \tag{4.10}$$

$$\Rightarrow \vec{B} = \begin{pmatrix} B_r \\ B_\theta \\ B_z \end{pmatrix} = \begin{pmatrix} -\frac{\mu_0}{4\pi} \iiint\limits_{\text{volume}} \frac{j_z r' \sin(\theta - \theta')}{\left[r^2 + r'^2 - 2rr'\cos(\theta - \theta') + (z - z')^2\right]^{\frac{3}{2}}} r' dr' d\theta' dz' \\ \frac{\mu_0}{4\pi} \iiint\limits_{\text{volume}} \frac{j_z (r - r'\cos(\theta - \theta')) - j_r (z - z')}{\left[r^2 + r'^2 - 2rr'\cos(\theta - \theta') + (z - z')^2\right]^{\frac{3}{2}}} r' dr' d\theta' dz' \\ \frac{\mu_0}{4\pi} \iiint\limits_{\text{volume}} \frac{j_r r' \sin(\theta - \theta')}{\left[r^2 + r'^2 - 2rr'\cos(\theta - \theta') + (z - z')^2\right]^{\frac{3}{2}}} r' dr' d\theta' dz' \end{pmatrix}. \tag{4.11}$$

The integration over θ can be performed immediately in the first and third integral because each component of $\vec{j}$ is independent of θ. The integration has been performed by using the fact that the integrand is a periodic function and by multiplying it with -1 so that the variable of integration θ can be replaced by $(\theta - \theta')$:

$$-\int_0^{2\pi} \frac{\sin(\theta - \theta')}{\left[r^2 + r'^2 - 2rr'\cos(\theta - \theta') + (z - z')^2\right]^{\frac{3}{2}}} d(\theta - \theta') =$$

$$-\frac{1}{rr'} \left[\frac{1}{\sqrt{r^2 + r'^2 - 2rr'\cos(\theta - \theta') + (z - z')^2}} \right]_0^{2\pi} = 0. \tag{4.12}$$

Thus $B_r = B_z = 0$ and $\vec{B}(r, \theta, z)$ can be written as:

$$\vec{B}(r, \theta, z) = \begin{pmatrix} B_r(r, \theta, z) \\ B_\theta(r, \theta, z) \\ B_z(r, \theta, z) \end{pmatrix} = \begin{pmatrix} 0 \\ B_\theta(r, z) \\ 0 \end{pmatrix}. \tag{4.13}$$

In general, this result is only valid for $r' \neq 0$. In the case that $r' = 0$ the integrand does not add to the integral. This is not true in general if the current density at $r' = 0$ diverges stronger than $1/(r'^2)$. However, this circumstance has to be considered only for tilted cross sections which are discussed in section 4.6. If only horizontal cross sections are considered, B_θ is the only component contributing to $\frac{1}{\mu_0} \oint\limits_{\text{contour}} \vec{B} \cdot d\vec{s}$.

For this simplified approach an important assumption is made about the current density distribution in z-direction. Since both modeling [62, 73] and experimental [74, 49] results indicate a Gaussian profile for the current density, a Gaussian profile for j_z is assumed:

$$j_z(r, z) = \frac{I_0}{2\pi (\sigma(z))^2} \exp\left(-\frac{r^2}{2(\sigma(z))^2} \right). \tag{4.14}$$

Here $\sigma(z)$ is the standard deviation which represents the characteristic spatial expansion of the arc and I_0 is the overall electric current through the arc. This assumption makes sense supposing a radial diffusion profile with electrical conductivity as approximately constant diffusion parameter. Hence the current density distribution j_z can be determined by calculating $\sigma(z)$. Since current is conserved ($\operatorname{div} \vec{j} = 0$), j_r can be calculated in the case of axial symmetry as follows:

$$\operatorname{div} \vec{j} = 0 \Leftrightarrow \frac{1}{r} \frac{\partial}{\partial r} (r j_r) + \frac{\partial}{\partial z} j_z = 0. \tag{4.15}$$

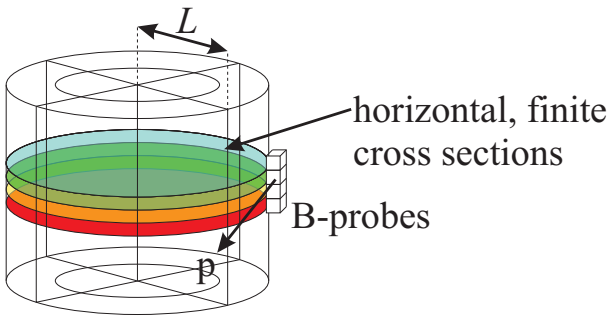

Figure 4.2: Horizontal cross sections with B-probes separated by L from the arc center.

Thus it follows for j_r:

$$j_r(r,z) = \frac{I_0}{2\pi(\sigma(z))^2}\frac{d\sigma(z)}{dz}\frac{r}{\sigma(z)}\exp\left(-\frac{r^2}{2(\sigma(z))^2}\right). \tag{4.16}$$

With these assumptions it is sufficient to measure the magnetic flux density along the tangent vector p of horizontal cross sections to calculate the current density distribution (see Figure 4.2). For these horizontal cross sections, the shortest distance L between the arc axis and the B-probes is constant. Thus, for an axially symmetric arc, the contour integral over the magnetic flux density simplifies as follows:

$$\frac{1}{\mu_0}\oint \vec{B}\cdot d\vec{s} = \frac{1}{\mu_0}\int_0^{2\pi} B_\theta L d\theta = \frac{1}{\mu_0}B_\theta 2\pi L. \tag{4.17}$$

On the other hand, the finite surface integral over the current density which crosses such horizontal cross sections yields

$$\iint_{\text{surface}} \vec{j}\cdot d\vec{A} = \int_0^L \frac{I_0}{2\pi(\sigma(z))^2}\exp\left(-\frac{r^2}{2(\sigma(z))^2}\right)2\pi r dr = I_0\left[1-\exp\left(-\frac{L^2}{2(\sigma(z))^2}\right)\right]. \tag{4.18}$$

With equations 4.17 and 4.18 $\sigma(z)$ can be calculated for each measured cross section:

$$\frac{1}{\mu_0}B_\theta 2\pi L = I_0\left[1-\exp\left(-\frac{L^2}{2(\sigma(z))^2}\right)\right] \tag{4.19}$$

$$\Rightarrow \sigma(z) = \frac{L}{\sqrt{-2\ln\left(-\frac{\Delta B_\theta}{B_0}\right)}}, \tag{4.20}$$

where $\Delta B_\theta = B_\theta(r=L,z) - B_0$ and $B_0 = \frac{\mu_0 I_0}{2\pi L}$. If ΔB_θ is negative and $|\Delta B_\theta| \leq B_0$, the expression for $\sigma(z)$ is well-defined and can be applied to determine the current density distribution at any point in space.' [5]

4.3 Experimental setups for measuring magnetic flux density distributions

4.3.1 Parameters of free burning arcs

The experimental setup of the free burning arc is described in section 2. In the first experiments that have been performed the arc length was set to 20 mm and the current was set to 50 A. Experiments subsequently performed make use of a 8 mm long arc and currents of 100 A, 125 A and 150 A. During every experiment the axial symmetry of the arc was validated by simultaneously observing the arc with the stereo-optical setup described in section 3.8.4.

4.3.2 Magnetic flux density measurements and data acquisition employing FPGA based hardware real time evaluation

'Since the experimental realization is a bottleneck for a successful conduction of the subsequently performed measurements (yielding the current density distribution inside a plasma arc), the setup for measuring magnetic fields near plasmas with a temperature range of a few tens of thousands of Kelvin will be described here in some detail. The magnetic flux density was measured employing Hall-effect devices which are placed along a vertical axis with distance L from the arc center. There are certain requirements the Hall-effect devices have to fulfill in order to be useful for such an environment. The Hall probes must be

- electrically temperature compensated in the temperature range they experience near the hot plasma.
- mechanically robust and small in size.
- insensitive to electrical noise.
- sensitive enough to measure magnetic fields in the μT range, since the magnetic flux in this case decays proportional to approximately $1/r$.

Furthermore, the signal acquisition should enable a reliable and fast measurement of magnetic fields at a defined point in time. In order to fulfill these requirements a HAL®855-A Hall-effect device manufactured by Micronas was put into operation. The HAL®855-A is temperature compensated in a wide range of -40° C to $+170^\circ$ C. A few layers of Kapton® foil provide additional temperature shielding. The actual temperature during the experiments was monitored employing a thermo couple and was always less than 140° C. The HAL®855-A is embedded in a standard transistor package, thus small and relatively robust. Due to the defined position of the chip inside the package the measurement of the magnetic field is possible at a small and known place. The Hall voltage is pre-amplified and converted to a TTL based pulse-width modulated signal that can be collected at one of the pins for further signal processing. Thus, the signals are hardly prone to electrical noise and disturbances. The range of measurable magnetic fields is programmable from ± 30 mT to ± 150 mT with a vertical resolution of 12 bit. This permits to measure magnetic fields as small as $15\,\mu$T which is adequate for currents in the range of $I_0 = 50$ A and distances in the range of $L = 20$ mm to $L = 30$ mm. These achievements enable the utilization of Hall-effect

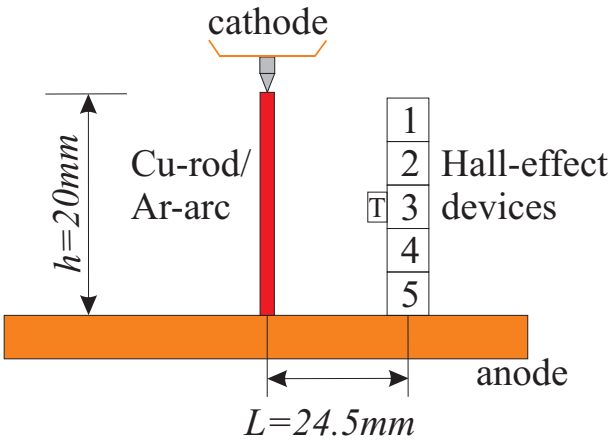

Figure 4.3: Schematic of arc setup with hall-effect devices; A copper rod is placed in between the electrodes during calibration. T: position of thermocouple for temperature measurement.

devices in such harsh environments. A schematic shows the setup of the Hall-effect devices (Figure 4.3). In order to facilitate simultaneous signal processing capable of processing up to 30 Hall probes at the same time, a FPGA (Field Programmable Gate Array) based data evaluation was developed. The utilized FPGA is a Virtex-II 1M Gate FPGA mounted on a R Series reconfigurable I/O PCI board from National Instruments. The application of a FPGA circumvents the necessity of multiplexing and allows a reliable, fast and coincidental calculation of magnetic fields based on hardware employing a parallel clock frequency of 40 MHz.

The procedure for measuring ΔB_θ is as follows: For a given electrode distance a copper rod with the same radius of the cathode r_0 is sandwiched in between the electrodes and a direct current I_0 is applied (see Figure 4.3). The Hall-effect devices which are placed at distance L from the z-axis are calibrated while the magnetic field is present. Next, the current is switched off and the copper rod is replaced by the arc ignited between the electrodes which remain at the same position. Now the measured magnetic flux density of the Hall-effect devices is equal to ΔB_θ. Note that this procedure has the advantage that any magnetic offset that is constant with time, e.g. the earth magnetic field or the field of the supply cables of the setup, can be neglected.' [5]

4.4 Results of current density measurements employing the simplified reconstruction approach

4.4.1 Results for 20 mm arc: magnetic flux densities and three-dimensional current density distribution

'The previously made assumption that $B_r = 0$ was verified in a preliminary experiment. Therefor B_r was measured 4 mm below the cathode at a radial distance of 22.5 mm. The mean value of $n = 100$ measurements was $B_r(r = 22.5\,\text{mm}, z = 4\,\text{mm}) = 0.005\,\text{mT}$. The standard deviation of this measurement was 0.01 mT. The first experiment that was carried out made use of the 20 mm long arc with a current of 50 A. The magnetic flux densities have been measured at a distance of $L = 24.5$ mm from the arc axis and the sensitive area of the Hall-effect devices have been separated by a distance of 4 mm, respectively, as shown

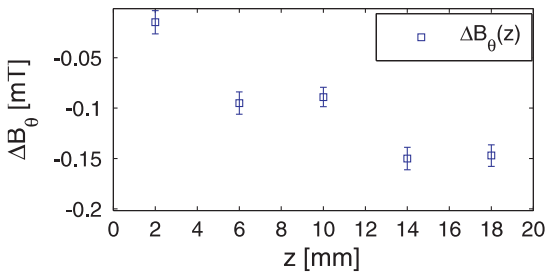

Figure 4.4: ΔB_θ measured simultaneously at five positions along the z-axis at a distance of 24.5 mm from the arc center.

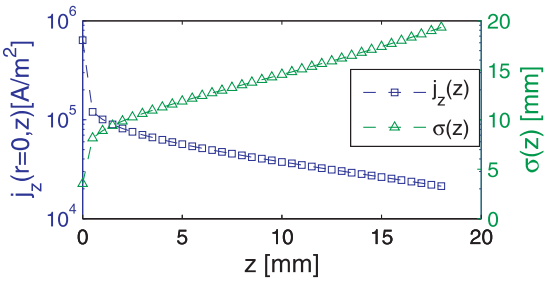

Figure 4.5: Characteristic spatial expansion of the arc $\sigma(z)$ and current density distribution $j_z(r=0)$ at the center of the arc; $I_0 = 50\,\mathrm{A}$.

in Figure 4.3. The results for ΔB_θ which have been measured at the five positions indicated in Figure 4.3 are displayed in Figure 4.4. This data was fitted to the following expression, enhancing the resolution of the measurements along the z-axis by assuming that $\Delta B_\theta(r = L, z = 0) \approx 0$ ($r = 0$, $z = 0$ is the position of the cathode):

$$-\frac{\Delta B_\theta(r = L, z)}{B_0} = A z^m. \tag{4.21}$$

Values for A and m are determined by fitting $\ln\left(-\frac{\Delta B_\theta(r=L,z)}{B_0}\right)$ to a straight line as a function of $\ln(z)$:

$$\ln\left(-\frac{\Delta B_\theta(r = L, z)}{B_0}\right) = a \ln z + b, \tag{4.22}$$

such that $m = a$ and $b = \ln A$. Hence $\sigma(z)$ and its corresponding axial derivative can be calculated as follows:

$$\sigma(z) = \frac{L}{\sqrt{-2m\ln z - 2\ln A}}, \tag{4.23}$$

$$\frac{d\sigma}{d(\ln z)} = \frac{mL}{(-2m\ln z - 2\ln A)^{3/2}} = z \cdot \frac{d\sigma}{dz}. \tag{4.24}$$

For $z = 0$ a value of $\sigma(z = 0) = r_0 \cdot \sqrt{2}$ is assumed. As a result, the current density distribution $j_z(r = 0)$ along the arc axis for $I_0 = 50\,\mathrm{A}$ and the characteristic spatial expansion of the arc $\sigma(z)$ are displayed in Figure 4.5. Isosurfaces showing the evolution of several constant current density profiles are depicted in Figures 4.6 and 4.7. Two isosurfaces are shown for j_z with particular current densities of $3 \times 10^4\,\mathrm{A\,m^{-2}}$ and $5 \times 10^5\,\mathrm{A\,m^{-2}}$ (Figure 4.6). Three isosurfaces are shown for j_r with particular current densities of $1 \times 10^3\,\mathrm{A\,m^{-2}}$, $1 \times 10^4\,\mathrm{A\,m^{-2}}$ and $2 \times 10^4\,\mathrm{A\,m^{-2}}$ (Figure 4.7). Here, j_z is about one order of magnitude larger than j_r.' [5]

4.4.2 Results for 8 mm arcs: Three-dimensional current density distributions

A series of current density measurements for different electric currents and constant arc length were performed. The parameters of the setup are listed in Table 2.1 of section 2. The results for the current density j_z for a total electric current of 100 A, 125 A and 150 A

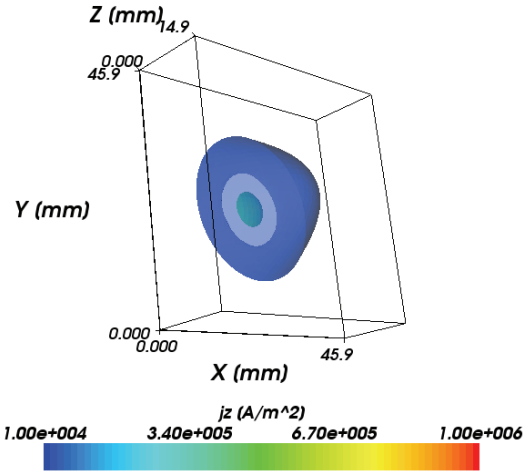

Figure 4.6: Isosurfaces for current density distribution j_z.

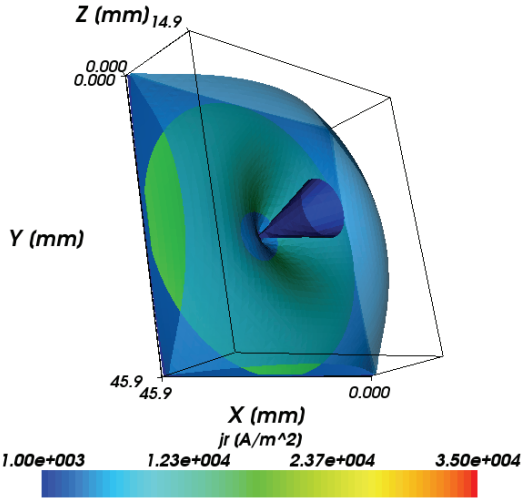

Figure 4.7: Isosurfaces for current density distribution j_r.

are shown in Figure 4.8. A photograph showing the corresponding radiation is depicted in Figure 4.9. Above are intensity lineouts showing the optical emission of the arcs. Note that a direct comparison of these lineouts with the obtained current densities is not easily possible. The radial decay of the intensities depends strongly on the spectral transfer function of the utilized camera. This can be seen for example in the hot cathode region of the 125 A and 150 A arcs. As was shown in the first part of this thesis, here the spectrum shifts towards blue wavelengths for which the camera chip is less sensitive. Further, the camera does not allow to visualize the outer zones of the arc due to the limited dynamic range of the camera chip. Additionally, the measured intensity profiles have to be Abel inverted for a direct comparison to the current density measurements. Thus an evaluation of the plasma emission similar to the evaluations of the first part of this thesis is necessary. This has been done in the subsequent section 4.5. The optical diagnostic to validate the axial symmetry (see section 3.8.4) yields three-dimensional plots for 100 A, 125 A and 150 A, respectively (Figure 4.10) and confirms axial symmetry. The current density shows an increase, both for higher currents and reduced distance to the cathode. Comparing the current densities 1 mm above the anode, the 100 A arc shows the highest current density despite the least total current is present here. This can be explained by examination of the photographs from Figure 4.9. Hence the smaller current can yield a higher current density if the radius of the arc close to the anode is smaller. This is comparable with observations of other authors where a current density of up to $30\,\mathrm{A\,mm^{-2}}$ was derived from arc pressure measurements for a current carrying arc radius of about 2 mm and total current of 100 A [77].

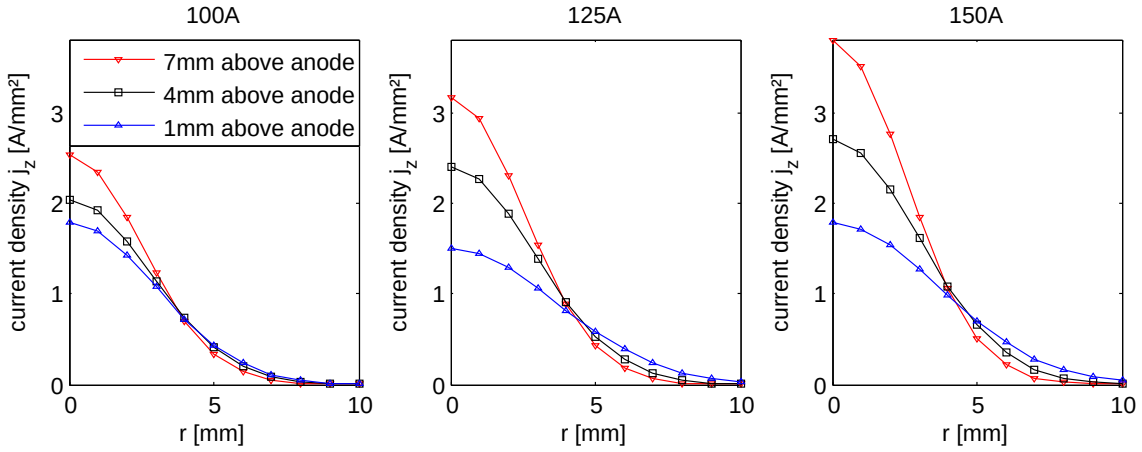

Figure 4.8: Electric current densities j_z for $100\,\mathrm{A}$ (left), $125\,\mathrm{A}$ (center) and $150\,\mathrm{A}$ (right), measured $1\,\mathrm{mm}$ ($\triangle$), $4\,\mathrm{mm}$ ($\square$) and $7\,\mathrm{mm}$ ($\triangledown$) above the anode.

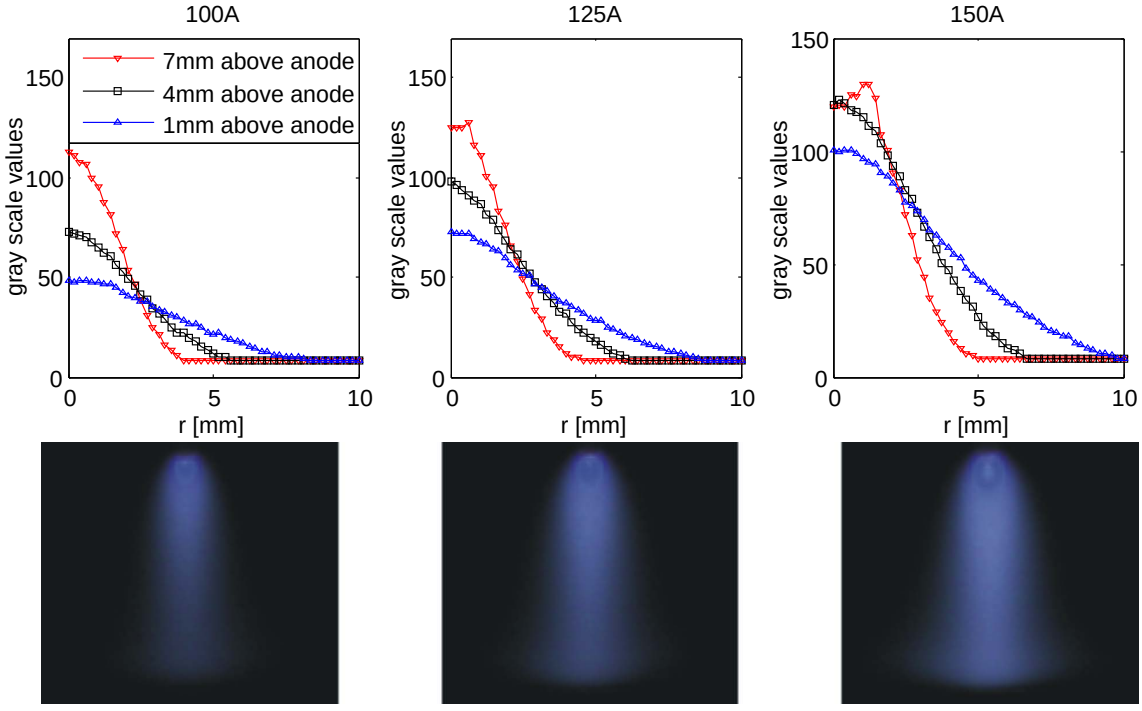

Figure 4.9: Photographs of electric arcs with total electric currents (bottom) and lineouts of intensities $1\,\mathrm{mm}$ ($\triangle$), $4\,\mathrm{mm}$ ($\square$) and $7\,\mathrm{mm}$ ($\triangledown$) above the anode (top) of $100\,\mathrm{A}$ (left), $125\,\mathrm{A}$ (center) and $150\,\mathrm{A}$ (right).

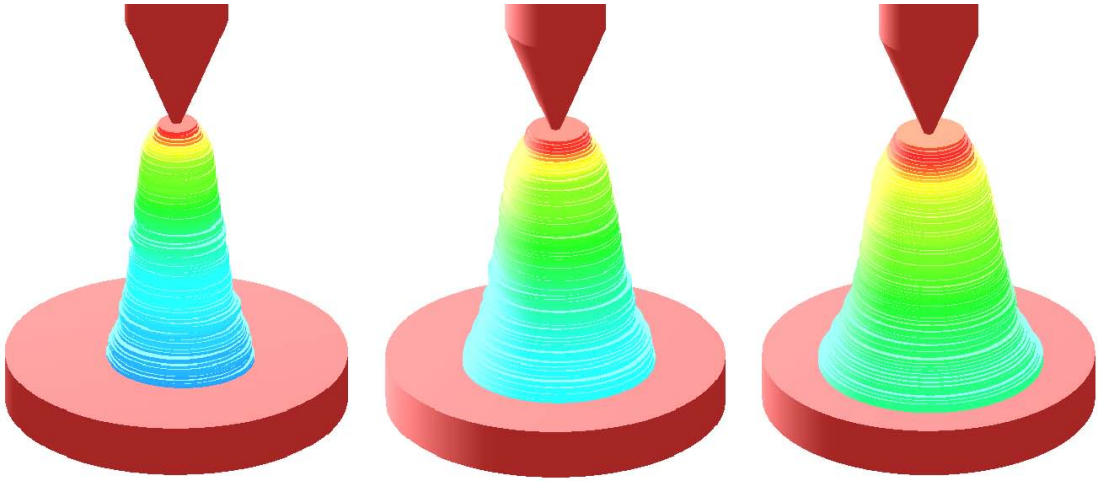

Figure 4.10: Optical 3D reconstruction of electric arcs utilized to verify axial symmetry as introduced in section 3.8.4 with total electric currents of $100\,\mathrm{A}$ (left), $125\,\mathrm{A}$ (center) and $150\,\mathrm{A}$ (right).

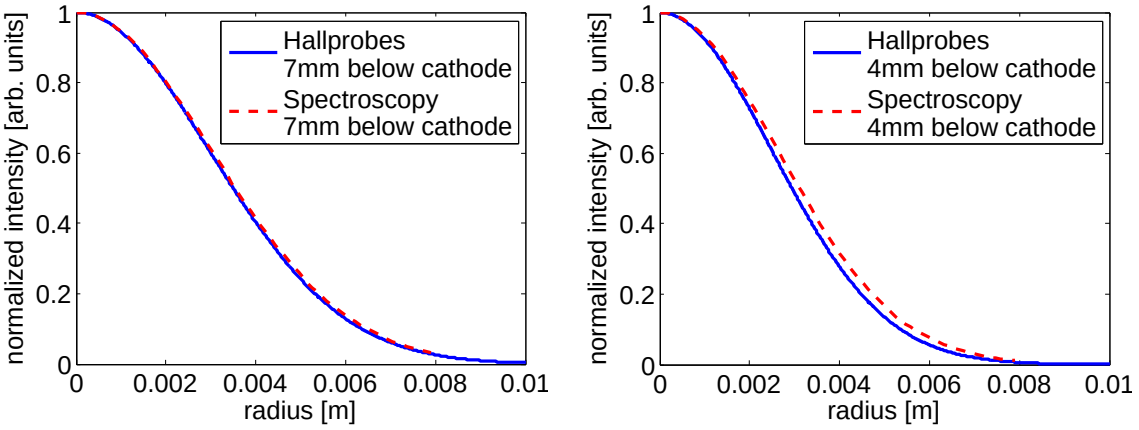

Figure 4.11: Comparison of results from magnetic and optical measurements of a 150 A argon arc.

4.5 Comparison with optical measurements

The results of current density measurements obtained with Hall-effect devices can be compared to the results from the optical high-speed diagnostic presented in the first part of this thesis (see Chapter 3). There, electrical conductivities have been derived from plasma temperatures. These conductivities can be used in principle to calculate current densities if the electric field distribution throughout the arc is known. The latter can be estimated by measurements of the overall arc voltage and voltage drops on the plasma sheaths. Since these measurements yield only a rough estimation of the electric field distribution, a direct comparison of the electrical conductivity and the current density was performed. This was done by normalizing the distributions of current density and electrical conductivity. Since current density is a linear function of the electrical conductivity ($j = \sigma E$) agreement of normalized distributions shows also agreement of both distributions without normalization. Measurements with Hall-effect devices can be compared with measurements with the optical high-speed diagnostics where experimental parameters were the same. Thus, Figure 4.11 shows a comparison of a 150 A arc which has been investigated with both introduced diagnostics. This comparison allows an independent validation of both newly developed plasma diagnostics since profiles obtained from 4 mm and 1 mm below the cathode agree very well.

4.6 Discussion of a general method for arbitrary non-intrusive current density measurements utilizing Hall probes

The experimental results shown in section 4.4 follow from the simplified approach introduced in section 4.2.2. The simplifications made there are the Gaussian profile for j_z and the axial symmetry which might be fulfilled in the majority of cases. Now, a way to measure the current density distribution applying the new approach without these simplifications will be discussed. First the assumption of axial symmetry will be kept and subsequently generalized. The main question resulting from section 4.2.1 is what kind of cross sections should be measured in order to determine the spatial distribution of current. Since $\frac{1}{\mu_0} \oint_{\text{contour}} \vec{B} \cdot d\vec{s}$ yields the current enclosed by the particular cross section, the task is

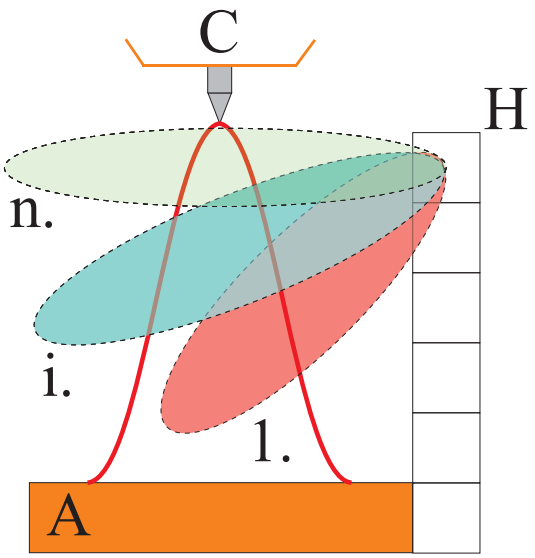

Figure 4.12: Tilted cross sections: cross section 1 encloses only part of I_0, cross sections i, n enclose entire current. H: Hall-effect devices, C: cathode, A: anode.

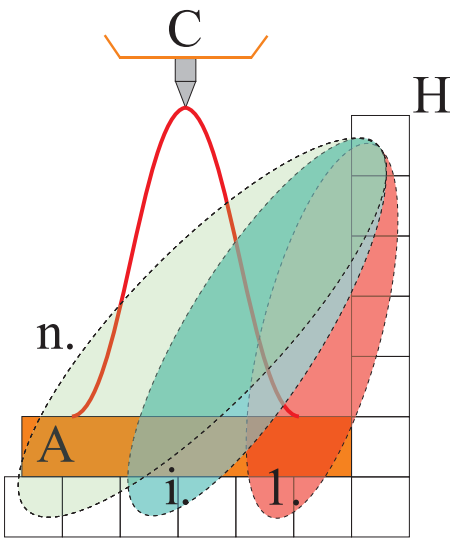

Figure 4.13: Hall-effect devices under the anode allow to measure cross sections enclosing different parts of I_0. H: Hall-effect devices, C: cathode, A: anode.

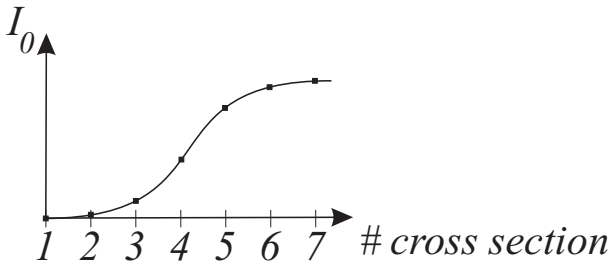

Figure 4.14: Increase of the enclosed current I_0 from cross section 1 to 7.

to find cross sections that do not enclose the entire current. This was achieved by arranging the Hall-effect devices so that the finite, horizontal cross sections in the simplified approach enclose only part of the total current. Another possibility is to obtain tilted cross sections from the measurement volume by placing Hall-effect devices on discrete positions around closed loops containing the current or part of it. In Figure 4.12, cross section i. and n. enclose the entire current I_0. Cross section 1. encloses only part of I_0 but two practical problems occur if one attempts to measure this cross section. First, a few Hall-effect devices have to be placed inside the plasma. Second, if these Hall-effect devices survive, e.g. by means of adequate shielding, this technique is not anymore *non-intrusive*. A better approach is to place Hall-effect devices beyond the plasma, namely under the anode. In the case of axial symmetry of $\vec{j}$ it is sufficient to measure $\vec{B}(r,\theta,z)$ along a vertical axis parallel to the z-axis and on the r-axis under the anode as shown in Figure 4.13. This allows to calculate the contour integral over $\vec{B}$ for n cross sections. Note that without assuming that $B_r = B_z = 0$, which was discussed in section 4.2.2, the measurement of B_θ is not enough to calculate contour integrals along tilted cross sections. Plotting the solution of each integral over cross sections 1. to n., shows the increase of the current density inside the arc (Figure 4.14). This approach can be generalized to any non-symmetric current density distribution by measuring $\vec{B}(r,\theta,z)$ also for different angles θ, so that the tilted cross sections can also be rotated around the z-axis. Rotating the cross sections dissects

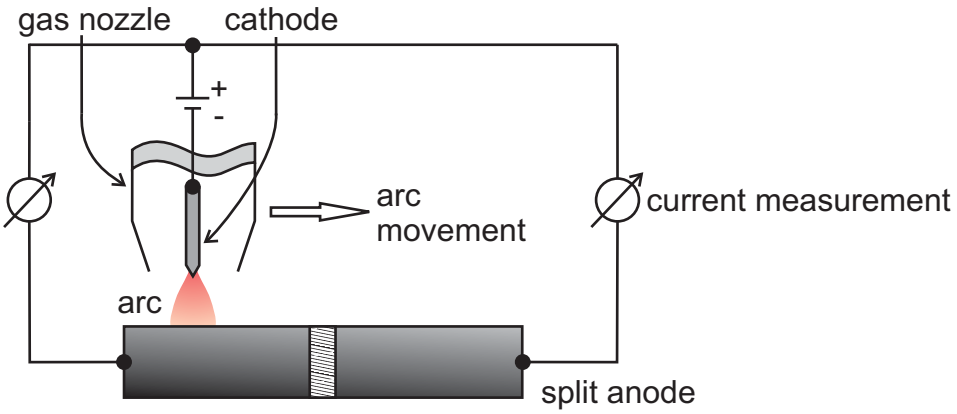

Figure 4.15: Schematic of the experimental setup developed by Nestor [74].

the arc in arbitrary surfaces. Intersecting cross sections divide the enclosed currents into parts flowing through a known surface area. The remaining current through each intersection divided by its surface area yields the corresponding current density. However, while the setup with e.g. 10 Hall-effect devices measuring one-dimensional magnetic flux densities in an axially symmetric case is doable, a three-dimensional plasma would require the setup of at least four times more Hall-effect devices which measure three-dimensional magnetic flux densities.

4.7 From current density measurements in free burning arcs to possible diagnostics of current phenomena in gas metal arcs

The diagnostic for current density measurements in free burning arcs makes use of magnetic flux density measurements which can be used to reconstruct current density distributions. The described simplified approach employs a physical model for the current density distribution in axial direction. This has been justified by the physical processes occurring in free burning arcs. A straight forward application of this approach for more complex plasma compositions which can be found e.g. in gas metal arcs is not possible in general due to the lack of information about the physical phenomena at work. More precisely, if the function of the current density profile in axial direction cannot be described by a single free variable, a closed loop integration of magnetic flux densities is not sufficient to solve the equation for one cross section through the plasma. Thus another idea that could be used to gather information on the distribution of current near the cathode of a gas metal arc will be outlined in what follows.

Principle of the measurement

Another method to measure the current density near the anode of a free burning arc has been developed by Nestor [74]. This method consists of dividing the electric current by a non-melting split anode over which an axially symmetric free burning arc is moved (see Figure 4.15). The measurement of the current through one of the anode segments as a

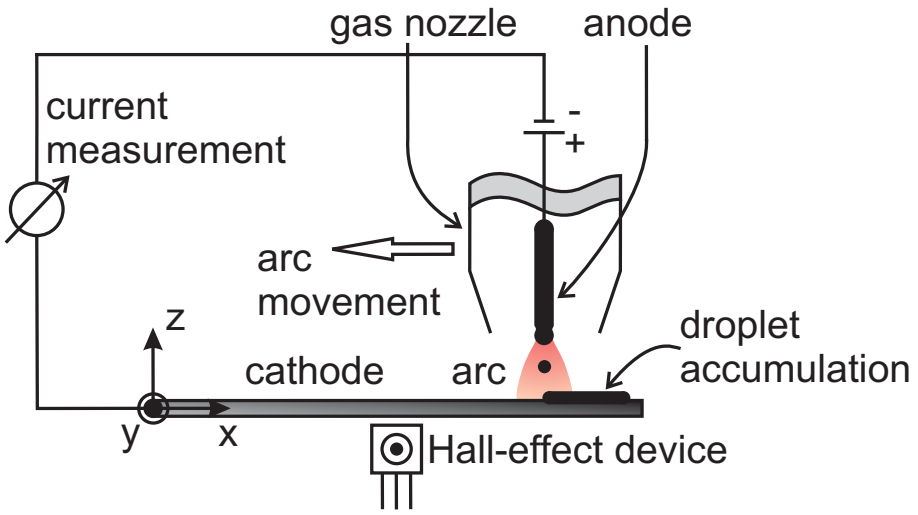

Figure 4.16: Illustrative sketch of the magnetic flux density measurements below the cathode of a gas metal arc process (side view). Here the arc is moved from the right to the left side.

function of arc position allows the calculation of the current density. Current density measurements in gas metal arcs are more challenging due to the material transfer through the plasma and process dynamics, especially if pulsed currents are involved. Thus, the utilization of the method proposed by Nestor is not possible for gas metal arcs, because in this case a split cathode would be immediately short-circuited by the metal droplets traveling through the plasma. (In gas metal arcs the base electrode is usually used as cathode. This is to increase the heat transfer to the melting wire due to the additional energy delivered to the anode by electrons.) Based on a combination of Nestor's method and the proposed generalized Hall-probe method (described in section 4.6) the idea involves a non-intrusive measurement of magnetic flux densities utilizing Hall probes. Instead of using a split electrode to detect a changing current, the magnetic flux density evolution underneath an unbroken electrode is measured. Hence the current distribution inside the cathode of a gas metal arc can be analyzed by observation of differences in the magnetic flux densities when experimental parameters are changed. The main idea is to linearly move the gas metal arc as shown in Figure 4.16. Here, the current flows through the arc into the cathode and from there, parallel to the x-axis, towards a single connection on the left side. Evaluating the overall current I_0 through the cathode as a function of $I_0(x)$, a continuous increase of this current should be visible. This is due to the spatial expansion of the arc which adds continuously to the cathode current as I_0 is evaluated along the x-axis (see Figure 4.17). Thus, a Hall-effect device which measures the component orthogonal to the x-axis and which is moved along the x-axis $B_y(x, y = \text{const})$ would measure an increase of magnetic flux density if moved from right to left and a decrease if moved from left to right. While in Nestor's method current densities can be deduced directly from current measurements, here the structure and formation of a magnetic field which is produced by a current density distribution has to be taken into account: A magnetic flux density produced by an electric current is the superposition of all B-vectors resulting from every current vector. However the magnetic flux density decreases approximately proportionally to $1/r$ with distance from a current carrying metal sheet. Hence a local measurement of magnetic flux density is influenced mainly by current flowing close to the Hall-effect sensor.

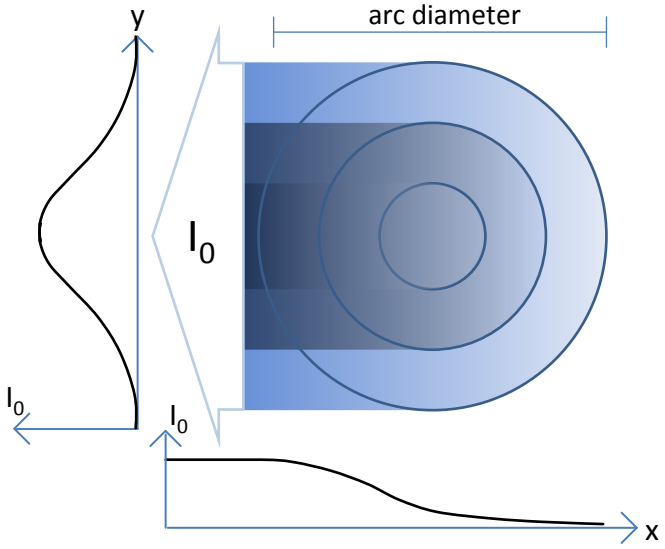

Figure 4.17: Interpretation of increasing current flowing through cathode (top view). Darker colors represent higher current densities.

Magnetic flux density measurements in the vicinity of a current carrying Aluminium sheet

In order to demonstrate how such a magnetic flux density distribution is evolving, a set of experiments has been carried out. These show that it is possible to map a changing current density distribution using this setup. In first experiments magnetic flux densities have been created by running a continuous current through an Aluminium sheet which is connected to a DC power supply at two sides. Two cables carrying a current of 30 A were connected to the central axis of the metal sheet and are separated by 70 mm. A schematic of this setup is shown in Figure 4.18 together with the expected magnetic flux density distributions along three different y-coordinates (1, 2 and 3). With this mockup it is possible to make detailed measurements of the magnetic flux density distribution in the vicinity of the Aluminium sheet. The mockup simulates in a simple way the magnetic field distribution in the vicinity of the cathode of a gas metal arc. One supply cable represents the conduction through the gas metal arc and the other provides the path for the return current. The magnetic flux density underneath the cathode was measured using a $1\,\mathrm{mm}^2$ mesh in the xy-plane, about 14 mm below the Aluminium sheet. A Hall-effect device capable of three-dimensional high-resolution ($< 7\,\mathrm{nT}$ resolution) magnetic flux density measurements was employed (Honeywell HMR2300). After a calibration measurement to account for the earth's magnetic field, each component of $\vec{B}(x,y,z)$ resulting from the current through the Aluminium sheet was measured. The results are shown in Figure 4.19 where the red arrows qualitatively indicate possible current paths. From these measurements it can be seen that changes in the current density which especially occur near the connectors can be mapped very well although the distance of the Hall-effect devices was quite large with respect to the Aluminium sheet (14 mm). These measurements show that a localized measurement of a current vector with Hall-effect devices is possible. However a certain 'blurring' due to the superposition of B-vectors from current vectors which are further away need to be taken into account in any kind of future evaluation. Figure 4.19 also shows that the x- and z-components of the magnetic flux density on the x-axis ($B_{x,z}(x, y = 0, z = -14\,\mathrm{mm})$) which connects the two supply lines is negligible small. Since

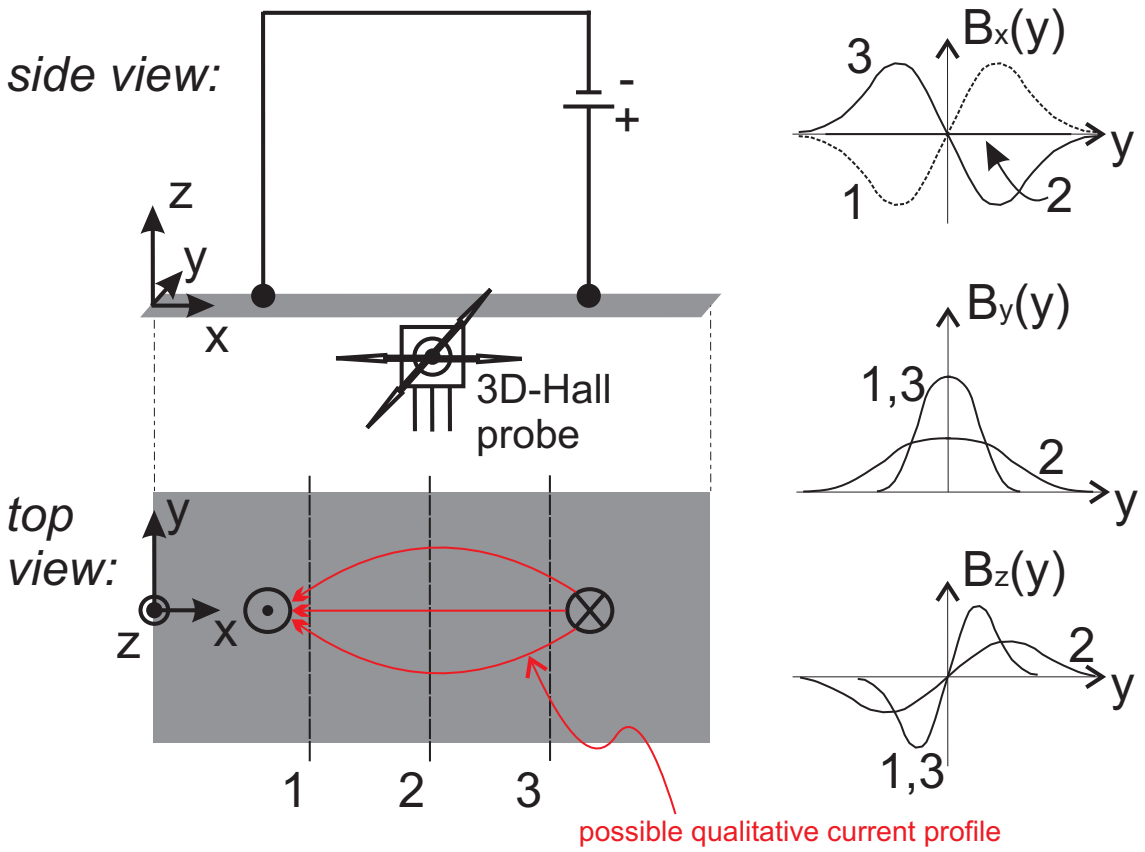

Figure 4.18: Sketch of the mockup to investigate magnetic flux density distributions in the vicinity of a current carrying metal sheet and expected magnetic flux densities along different y-coordinates (1, 2 and 3).

the visible symmetries of the magnetic field distribution can be expected to be similar in gas metal arcs it would be sufficient to measure the y-component of the magnetic flux density along the x-axis: $B_y(x, y = 0)$ in order to investigate how the distribution of current is evolving in the cathode of a gas metal arc.

Magnetic flux density measurements in the vicinity of the cathode of a gas metal arc

In order to apply this technology to a pulsed gas metal arc, changes need to be made because the previously used Hall-effect device HMR2300 is too slow (154 samples per second). Thus a fast linear Hall-effect sensor with PWM output and a sampling rate of 2000 Hz (Micronas HAL 2850) was utilized for magnetic flux density measurements. Additionally, during these measurements the overall current of the plasma process was measured and the process was monitored with a high-speed camera (PCO.1200s for Al/Ar arcs and PCO.dimax for Fe/Ar arcs). Thus the reproducibility of the pulsed process could be ensured between each current pulse by comparison of the arc shape and overall current. Subsequently performed experiments make use of an Aluminium/Argon arc and an Iron/Argon arc. A photograph showing the gas metal arc setup with a Hall-effect device underneath the cathode is depicted in Figure 4.20. The magnetic flux density measurement is performed 3 mm below the cathode. In first experiments the arc is moved from the right to the left. Thus the Hall-effect device starts measuring from a position close to the current carrying part of the cathode (see Figure 4.16). High-speed images of the arcs

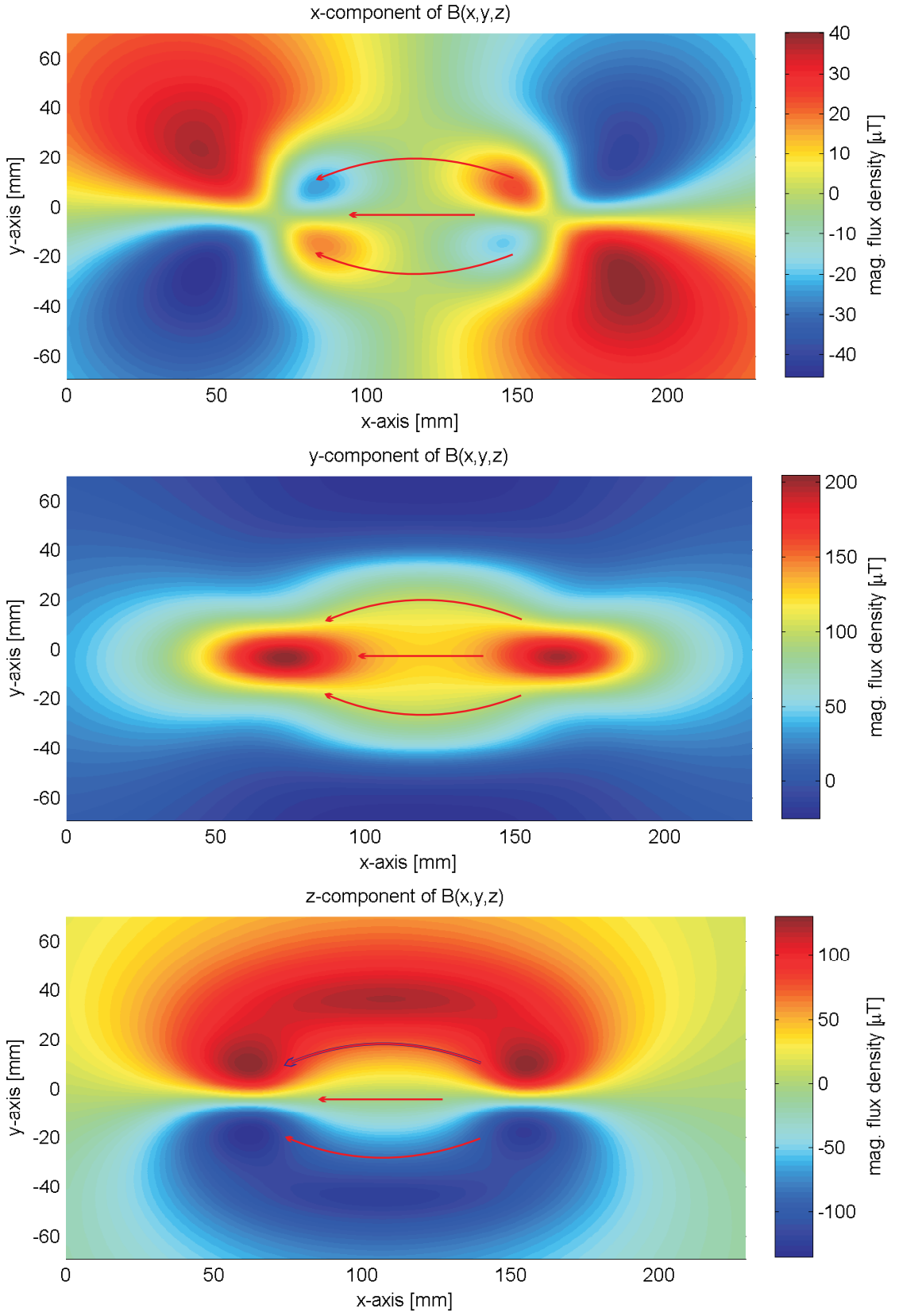

Figure 4.19: Measured high-resolution magnetic flux densities in the vicinity of a current carrying Aluminium sheet: $B_x(x,y)$ (top), $B_y(x,y)$ (center) and $B_z(x,y)$ (bottom). The red arrows qualitatively indicate possible current paths. Note that the measurement of B_z is slightly shifted to the left with respect to the x-axis in comparison to the B_x and B_y measurements. This is because the position of the chip measuring B_z is shifted in the chassis of the Hall-effect device.

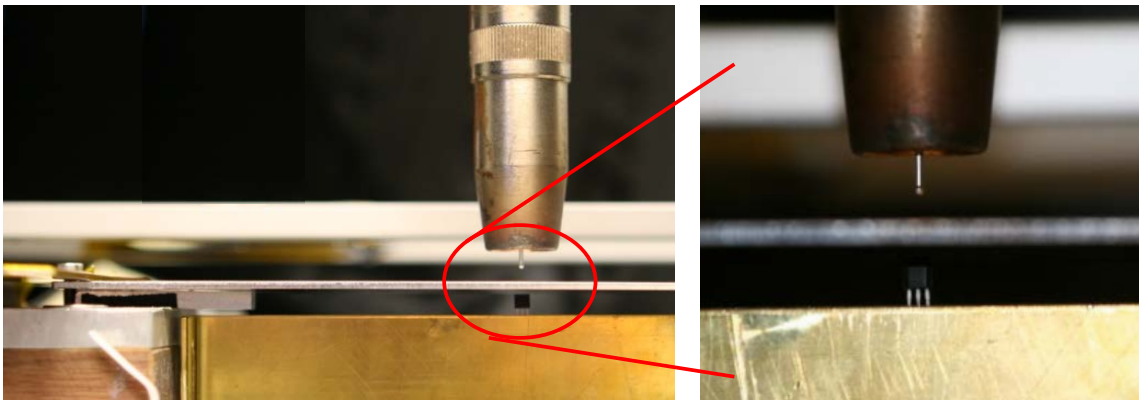

Figure 4.20: Photograph of the experimental setup. The current from the arc is guided through the cathode towards a single connection on the left side.

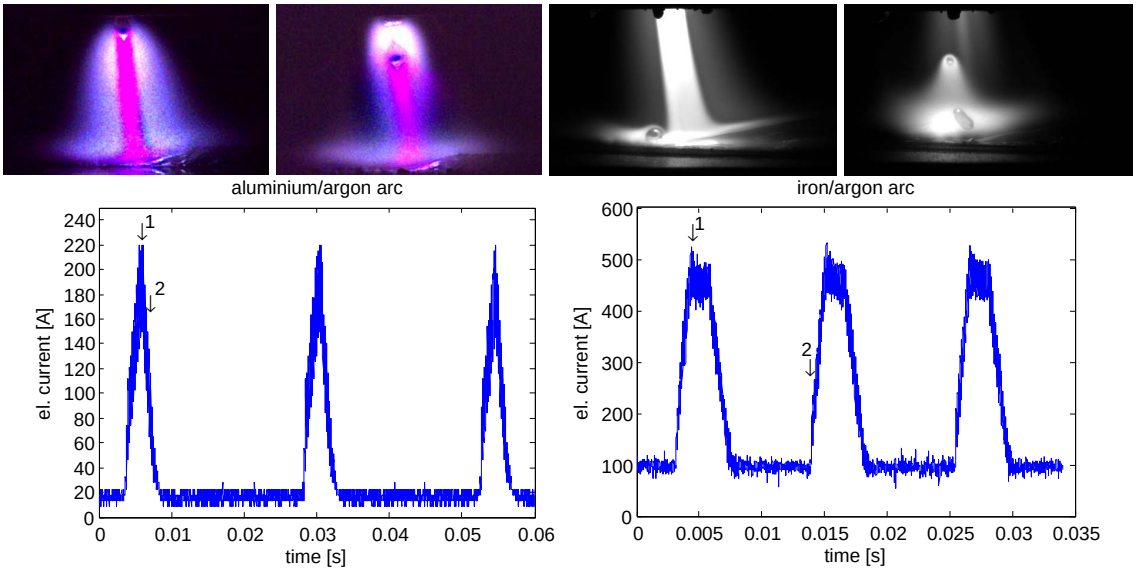

Figure 4.21: High-speed images of gas metal arcs before (1) and after (2) droplet detachment (top) and measured overall currents of Aluminium/Argon arc (left) and Iron/Argon arc (right).

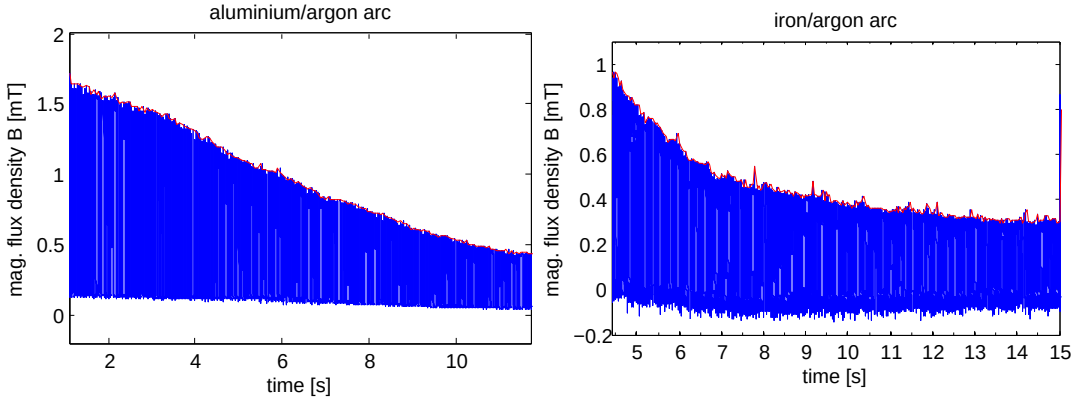

Figure 4.22: Measurement of the magnetic flux densities ($B_y(t)$: blue curves - alternating due to pulsed current) below the cathode during experiments with Aluminium/Argon arcs (left) and Iron/Argon arcs (right). Red curves: envelope of alternating magnetic flux densities. The plots display the magnetic flux densities measured from the moment when the arcs are ignited.

showing the high current phase are displayed together with measured overall currents in Figure 4.21. The images show an Aluminium/Argon arc (left) and an Iron/Argon arc (right) before and after the droplet detachment at the indicated moments. In both cases the confined central region of the arcs with a high metal vapor concentration and the surrounding plasma containing mainly Argon is clearly visible [72]. Figure 4.22 shows the corresponding axial distribution of the magnetic flux densities for both cases. The blue curve shows the changing B-field during each current pulse while the red curve shows the envelope of the magnetic fields measured during the high current phase. As expected a continuous decrease of the magnetic flux density is visible as the arc moves over the Hall-effect device: At the beginning of the measurement the Hall-effect device measures the entire current through the cathode resulting in a high magnetic flux density. While the arc moves over the Hall-effect device the cathode experiences a decreasing current density at the position where the Hall-effect device is located. This leads to the shown decrease of magnetic flux density for the Ar/Al arc and the Fe/Ar arc. Note that the envelopes shown in Figure 4.22 display different absolute values of the magnetic flux density. The values for the Al/Ar arc are in the range of 1.6 mT which is higher than those for the Fe/Ar arc which are in the range of 1 mT although the applied pulsed current was higher in the latter case. This is due to the relative permeability of the steel cathode which shields magnetic fields.

Reproducibility of the measurements and exchange of the direction of arc movement

To investigate further how the magnetic flux density and thus the current density is affected if experimental parameters are changed as well as to show the reproducibility of these measurements another set of experiments was carried out. The previously performed experiment with the Al/Ar arc has been repeated 12 times. Afterwards the direction of the arc movement has been changed towards the right so that the Hall-effect device starts measuring from a position away from the current carrying part of the cathode. A sketch of this experimental setup illustrating the reversed arc movement is depicted in Figure 4.23. This experiment has also been repeated 12 times. Two measurement results are shown in Figure 4.24 where the left graph shows the arc movement from right to left. Here the current flows from the arc towards the ground cable through a cold cathode. In the second case where the arc moves from left to right (right graph) the current flows through the part of the cathode which has been already modified by the material transferred from the melted wire to the cathode. Comparing the two graphs of Figure 4.24 a difference in the B-field distribution is visible. This may be explained by the following hypothesis: The temperature of the cathode is elevated to levels around the melting point of steel in regions where the arc already transferred droplets to the cathode. Thus the electrical resistivity should be also elevated close to those areas where the droplets were deposited. In conclusion the current density distribution should be affected by the direction of arc movement. This can be seen in the right graph of Figure 4.24 where the magnetic flux density is decreasing after 5 s. During this time interval the arc is moving over the location of the Hall-effect device. The decrease of magnetic flux density can be explained by a spreading of the current density in areas of lower cathode temperature and thus lower resistivity. Thus the flattening of the current density results in a decrease of magnetic flux density on the x-axis. The reproducibility of this behavior is shown in Figure 4.25 which displays the curves of all 12 experiments for each direction of moving arcs. In future experiments

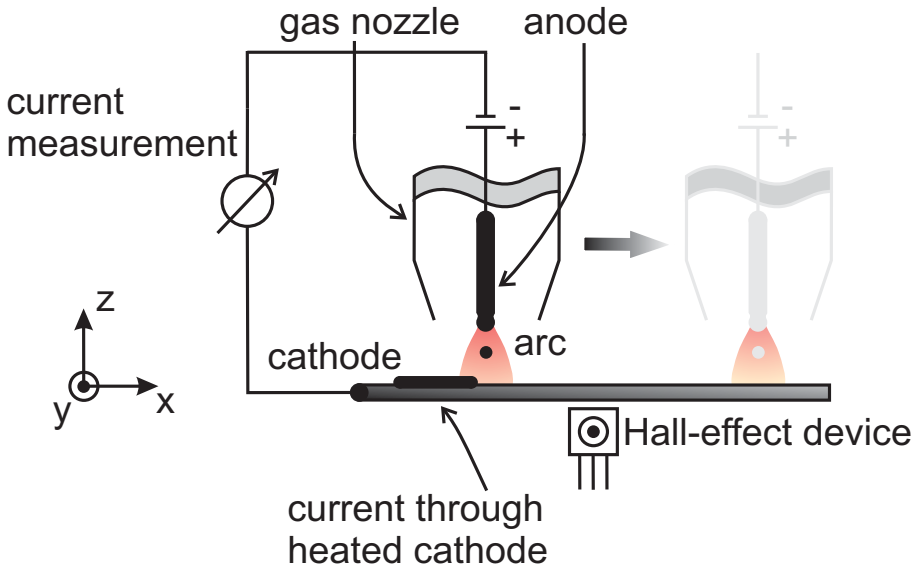

Figure 4.23: Schematic of the magnetic flux density measurements below the cathode of a gas metal arc process (side view). Here the arc is moved from the left to the right side.

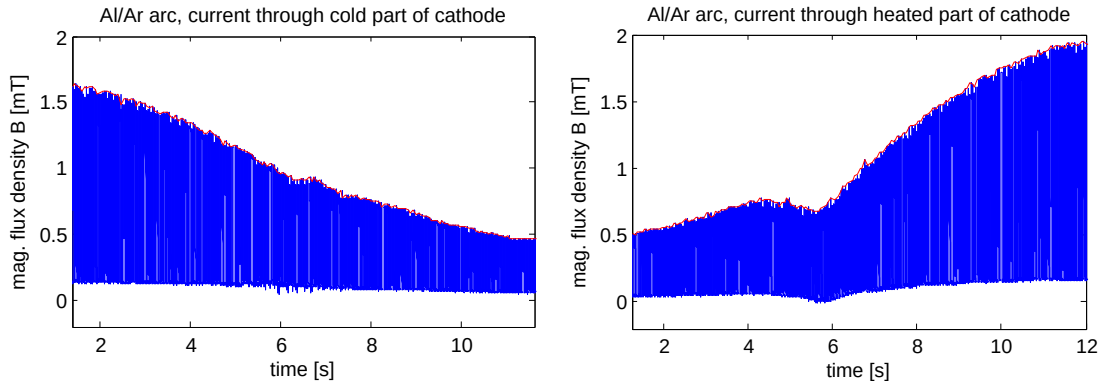

Figure 4.24: Measurement of the magnetic flux densities ($B_y(t)$) below the cathode during experiments with Aluminium/Argon arcs. Shown is the changing B-field during each current pulse (blue) and the B-field present during the high current phase (red). The plots display the magnetic flux densities measured from the moment when the arcs are ignited.

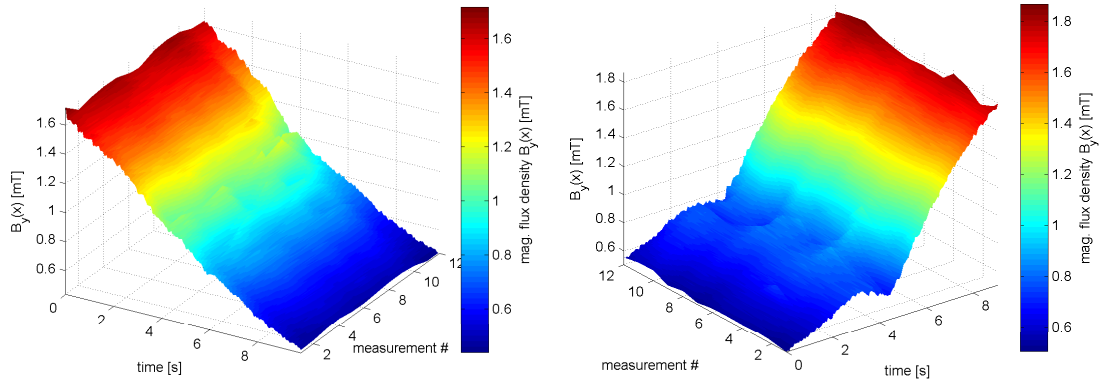

Figure 4.25: Series of measurements of the magnetic flux densities ($B_y(t)$) below the cathode during experiments with Aluminium/Argon arcs. The left graph results from arcs moved from the right to the left and the right graph results from arcs moved from left to right.

this phenomenon could be further investigated also for different materials. Further, the corresponding impact of the droplets on morphological changes occurring in the cathode could be analyzed. Here differences in morphology could be visible if the current is more spread over the cathode as it seems to be the case if the arc is moving from the left to the right side. A resulting lower current density would contribute less to the ohmic heating of the cathode and thus may impact the seam and bead geometry of the modified metal.

PART 3

Chapter 5

An *in situ* diagnostic to measure thermophysical droplet properties and droplet temperature in gas metal arcs

5.1 Introduction

‘Thermophysical properties of high temperature melts such as surface tension, viscosity, density as well as bulk temperature are of major interest e.g. for industrial welding processes and the modeling of such processes. These properties influence the droplet formation, the droplet detachment and the fluid flow in the weld pool which is crucial for understanding the formation of the welding seam as well as bead geometry. Since surface tension was recognized an important thermophysical property of materials, different methods have been developed to determine its value for a variety of geometries and materials. These methods can be grouped in non-contact and contact methods. The latter are widely used for liquids in a room temperature regime where the fluid can be brought in contact with a solid of known properties and geometry. These methods are based either on the deformation of a bulk fluid where a solid of known geometry is immersed, like the Wilhelmy plate or the Du Noüy Ring method [76], or on the deformation of a spherical droplet that is attached to a plate or a capillary, e.g. the sessile drop [54], pendant drop [2, 21] or maximum bubble pressure method [90]. The non-contact methods are based on the oscillation of a liquid droplet about its sphere. Surface tension σ can be determined due to the natural frequency ($\omega = 2\pi f$) of these oscillations as introduced by Lord Rayleigh [87]:

$$\sigma = \frac{3}{4\pi} \frac{\omega^2 M}{l\,(l-1)\,(l+2)}, \tag{5.1}$$

where M is the mass of the liquid and $l \in \mathbb{N} \setminus \{0,1\}$ is the oscillation mode number. The frequency corresponding to $l = 2$ is called the Rayleigh frequency. While $l = 1$ corresponds to the droplet translation, oscillation modes for $l > 2$ can be neglected if the droplet radius is smaller than the capillary length $l_c = \sqrt{\sigma/(\rho g)}$, where ρ is the droplet density and g the gravitational force [18, 71]. In addition to this, the oscillations are periodic if the radius is considerably larger than the characteristic radius $R^* = \eta^2/(\sigma\rho)$, where η is the viscosity of the droplet [8, 18]. Droplets which have been analyzed in this work fulfill these criteria for a periodic oscillation in the Rayleigh frequency. The advantage of these techniques is that surface tension of fluids which are normally solid at room temperature can be analyzed up to their boiling points by utilization of different heating mechanisms such as laser beams [36], electromagnetic fields [35] induction heating [44] or thermal plasmas [71]. However, the values for surface tension of liquid metals and their alloys obtained by these methods show partly considerable deviations from the results presented by different authors. Comparisons of different studies are shown for liquid Aluminium [36] Copper [53, 68], Gold [53], Iron [33, 104, 79], Nickel [33, 37], Ruthenium [52], Silicon [35, 45] and others.

These oscillating drop methods can be grouped in microgravity, levitated drop and free falling drop methods. Microgravity methods (10^{-6} g) performed in space [48, 82] or on parabola flights [46] are known to be very accurate due to the absence of external force fields but are limited with respect to availability. The levitated drop methods vary in the type of levitation. Electromagnetic [27, 28] or electrostatic [52, 81] levitation is suitable for conducting materials while aerodynamic [70] or acoustic [66] levitation can also be employed e.g. for ceramics or aqueous solutions. A combination of different levitation methods is also possible [80]. A disadvantage of the levitation methods is the perturbation of the drop oscillation by the levitating force field whereby the characteristic oscillation frequency splits into different frequency peaks. Mathematical corrections for this circumstance have been suggested by Cummings and Blackburn [20]. These corrections are not necessary for free-fall oscillating drop methods where an initial deformation results in a damped oscillation of a free falling drop due to internal restoring forces. In that case equation 5.1 can be employed to calculate surface tension. In addition the viscosity of the oscillating droplets can be determined by the non-contact methods. The dynamic viscosity η of free falling droplets with radius R can be related to the damping constant Γ [57]:

$$\eta = \frac{3M}{20\pi R}\Gamma. \tag{5.2}$$

While these setups are challenging due to the experimental realization of a containerless facility for heating and controlling the liquid drops, a different situation can be found in gas metal arcs. The research presented here makes use of the natural oscillations of liquid metal droplets occurring during the material transfer of a pulsed gas metal arc process. This approach is advantageous because by doing this, material properties like surface tension can be measured directly during the process of gas metal arcs without interference with the process itself. Hence there is no need for an indirect method e.g. by simulation or pyrometric temperature measurements which are compared with reference data for temperature-dependent surface tension.

In pulsed gas metal arcs a continuously supplied metal wire is melted by an electric arc which is generated between the wire tip (here set as anode) and a metal sheet (set as cathode). Depending on the electric voltage drop along the arc and the wire feed rate, the arc length can be adjusted. If the arc is long enough and sufficient energy is brought into the wire, droplets are formed due to various forces but are especially influenced by the surface tension of the molten tip. As shown in Figure 5.1, these forces include [91]:

- external mechanical forces (1), (2),
- electromagnetic forces (*pinch* effect) (3), (5), (10),
- forces resulting from evaporation of liquid metal (6),
- restoring forces resulting from surface tension (7),
- gravitational forces (8),
- external magnetic forces (9), (12),
- forces resulting from fluid flow of gases, plasma and metal vapours (4), (11), (13).

While traveling to the cathode these droplets experience a damped oscillation which is excited by the initial detachment from the wire tip (see Figures 5.1 and 5.2). Hence such a metal droplet detaches like a droplet from a water tap by building a shrinking

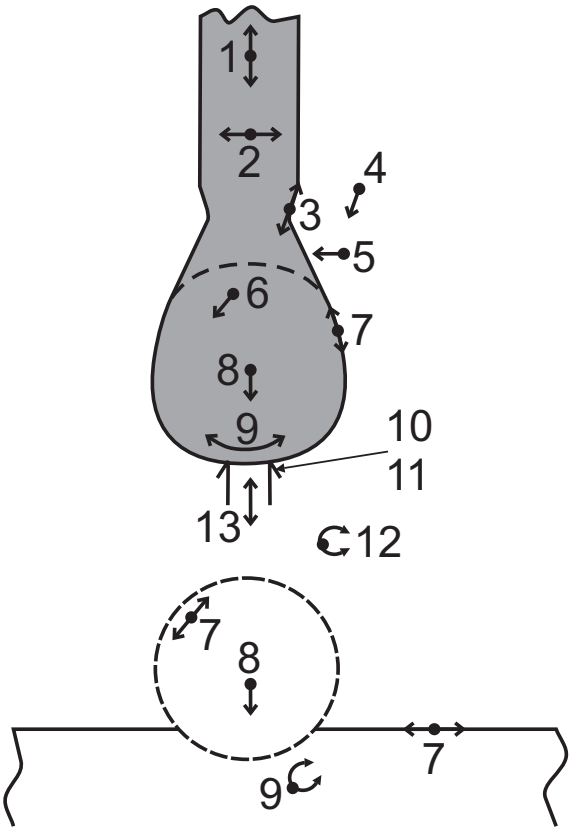

Figure 5.1: Forces during material transfer in gas metal arcs [91].

bridge to the liquid wire tip while moving downwards until the bridge brakes [61, 85, 25]. Residual liquid metal from the bridge accelerates back to the wire tip and the falling droplet due to surface tension. When this residual metal is absorbed, a damped oscillation is induced in the droplets (section 5.4) and the liquid wire tip due to internal restoring forces (indicated in Figure 5.1: (7)). In order to enhance the pinch-effect to enhance droplet detachment the pulsed gas metal arcs employ peak currents in the range of a few hundred Amperes. The main droplets generated have diameters in the mm-range and often show complex surface waves in addition to the oscillation induced by the initial detachment (Figure 5.2, 1-8). Aside from this, these droplets perform very few, if at all one complete oscillation until they reach the cathode. Multiple droplet oscillations are necessary to measure viscosity and are desirable to minimize uncertainties in surface tension measurements. Hence these primary droplets are hardly applicable for the study of surface-controlled oscillations. Depending on the control process of the power supply, more than one droplet is detached. In addition to the primary droplet one or more smaller droplets can be formed from the liquid wire tip. These so-called satellite droplets detach either from the liquid wire tip or are formed from the metal bridge created in between the primary droplet and the liquid wire tip (Figure 5.2, 7-15). Depending on where they are created, the satellite droplets show different translational motion. In some cases they are re-absorbed by the wire tip or the primary droplet or they levitate for a certain time in the free space while performing damped oscillations. Because of the smaller diameter compared to the primary droplet, these oscillations are almost perfect about a sphere (detaching droplet in Figure 5.2, 14-16) and thus suitable for investigation of surface-controlled oscillations.

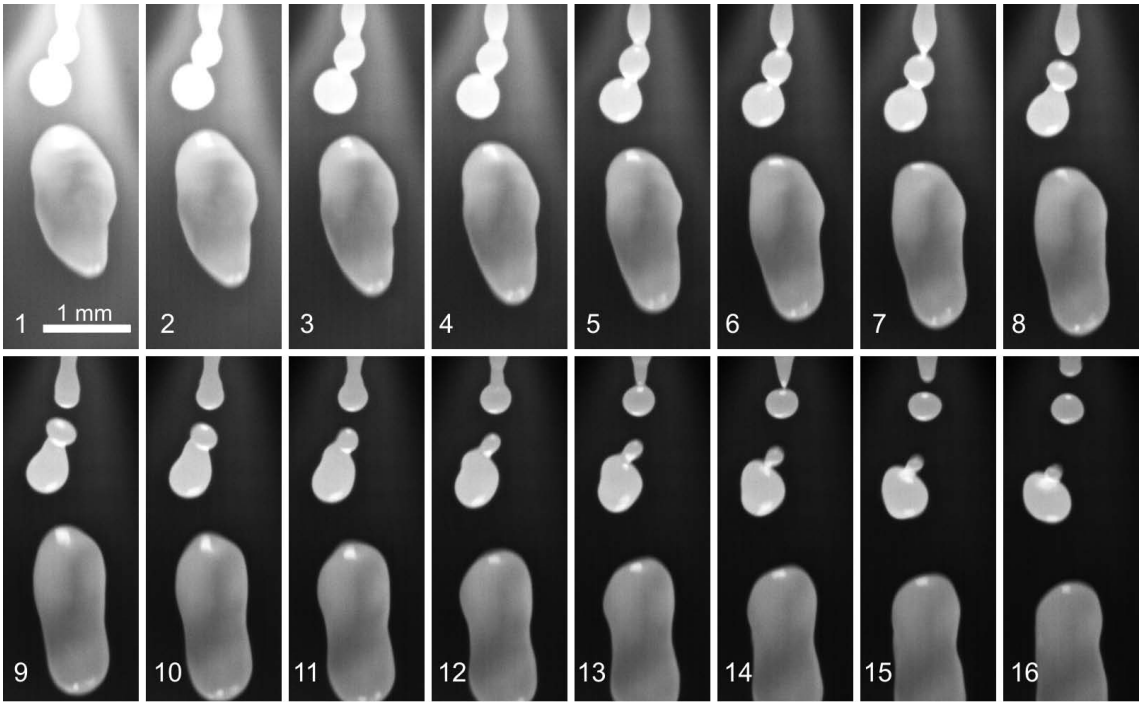

Figure 5.2: Detachment of droplets: A primary droplet is followed by satellite droplets.

The research presented here is based on several improvements with regard to work previously performed on the determination of surface tension in a gas metal arc process [99, 98]. The developed approach is based on a direct imaging technique using frame rates up to 30000 fps in combination with image processing algorithms to extract the oscillating movement of the edge contour of the liquid droplets. The edge contour is subsequently used for time and frequency domain studies along different dimensions of the droplets as well as volume calculations. Also the effect of temperature on density was incorporated in a simple model yielding surface tension, temperature and density of the droplets. This is advantageous since estimation of the density would result in large uncertainties of the derived parameters if the droplet mass is calculated from the high-speed images. (In this case the droplet mass would be calculated using the estimated density and the droplet volume which can be calculated with the known image magnification and assuming axial symmetry.) In this work a pure Iron wire was utilized as metal with a high density gradient with respect to temperature. In addition modifications to the cathode setup were made to enable the direct determination of droplet mass. This was achieved by employing a donut shaped cathode where the liquid droplets fall through the center and quench in a water basin. The droplets were analyzed subsequently yielding the accurate mass that is needed for surface tension measurements if the density is not known. The novel research presented here also shows the determination of viscosity by calculating the damping of droplet oscillations along different axes of a droplet.

In this work two cases of droplet formation are considered. First droplets that are surrounded by plasma are studied (see Figure 5.3, left) and subsequently droplets that are separated from the main plasma column are analyzed employing the donut cathode setup (see Figure 5.3, right). Numerous experiments have been performed in both cases in which the general behavior of the droplets was shown to be highly reproducible.' [6]

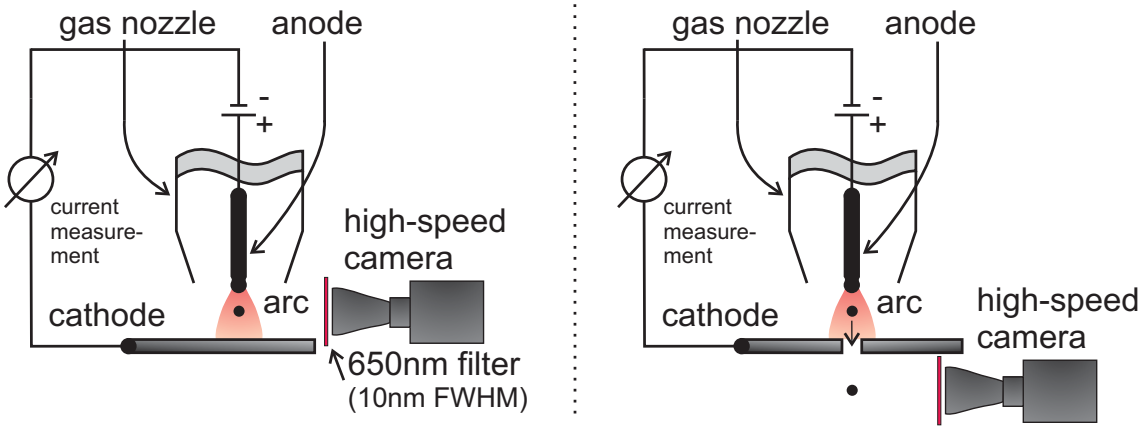

Figure 5.3: Schematic of the employed experimental setups.

5.2 Experimental setup to visualize droplets in a gas metal arc

'The droplets were visualized by directly recording the gas metal arc (see section 2) with a 12 bit monochrome high-speed camera (PCO.dimax). Since most high-speed cameras can be adjusted in frame rate and resolution, one faces the difficulty of finding an optimum between a high frame rate and a high image resolution for the evaluation, because increasing one property results in reduction of the other. For this work an optimum frame rate has been found that is in between 20000 fps and 30000 fps which corresponds to a pixel number of $240x600$ and $240x400$, respectively. With the utilized camera higher frame rates are possible with a reduced number of pixels. A high resolution is necessary in order to extract the exact edge contour of the droplets which in turn is used to calculate surface tension via the oscillation frequency and viscosity via the damping of oscillations. A high resolution is especially important to measure the sometimes small damping constants of a droplet oscillation. An additional macro lens was utilized together with a macro-planar objective (Zeiss T* 2/100mm ZF) yielding a spatial resolution of $6-8\,\mu$m/pixel. This spatial resolution was determined by calibrating a test image with the wire electrode which has a well-defined diameter.

Another challenge that occurs when recording the droplets is the strong plasma emission in the visible spectrum. In order to suppress this radiation which is dominated by lines, a dichroic optical bandpass filter was inserted in the optical path. With a central wavelength of 650 nm and a FWHM of 10 nm most of the plasma emission of both, Argon and Iron, can be suppressed due to the low amount of line radiation in this spectral window (see Figure 5.3). It is easier to implement than e.g. backlighting or shadowgraphy techniques which have been used previously for visualizing droplets in gas metal arcs. This setup enables direct and detailed observations of liquid Iron droplets which are surrounded by highly radiating plasma and thus allows for accurate measurements of the edge contour by the subsequently described image processing technique.

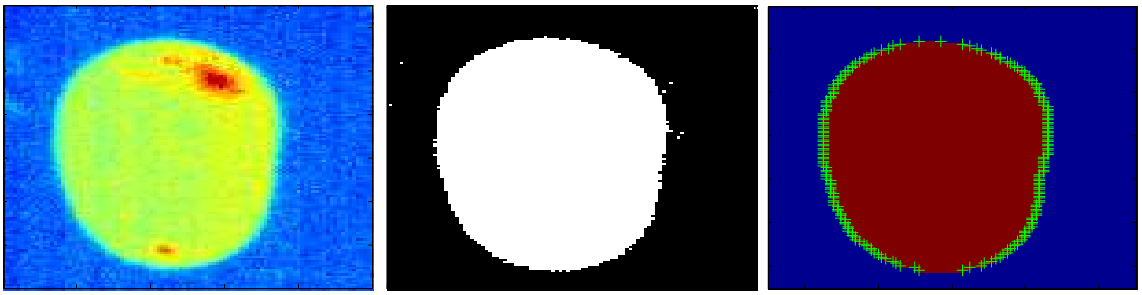

Figure 5.4: a) False color photography of a droplet (left). b) Image after setting a threshold (center). c) Image after morphological erosion and dilation with resulting edge contour (right).

5.3 Image processing, data evaluation and determination of droplet mass for high temperature melts

5.3.1 Image processing and data evaluation by thresholding, morphological erosion and dilation and conversion to a binary image

A raw image of the just described optical setup is displayed in Figure 5.4 a). The false color representation emphasizes the changes of the original 12 bit gray scale values near the droplet edge. The preprocessing of these images which was carried out before critical droplet dimensions were extracted is divided in three steps:

- thresholding,
- morphological erosion and dilation
- conversion to a binary image

In the first step, pixels that exceed a set threshold value are set to the maximum intensity value of 2^{12} (see Figure 5.4 b)). This threshold was determined as a maximum background noise of the surrounding medium. Particles in the micrometer length scales which appear in some images as well as small regions of remaining plasma radiation as can be seen from Figure 5.4 b) are eliminated in the second step: Here morphological erosion and dilation was performed with a disc employing a radius of $40\,\mu$m. In the last step the images are binarized utilizing a threshold value of 0.5×2^{12}. Then regions of interest (ROI) were defined enclosing only the droplets which are analyzed. The ROIs of the binary images were scanned line-by-line for low-high and high-low transitions to extract the edge contour of the droplets. A digitized droplet with resulting edge contour (green) is displayed in Figure 5.4 c). Finally edge contour values are stored in a matrix in order to extract the horizontal droplet radii a and the vertical radii b of each droplet which are subsequently used for time and frequency domain studies.

5.3.2 Determination of droplet mass and density

As can be seen from equations 5.1 and 5.2, the droplet mass M (or droplet density $\rho = M/V$) is one of the parameters which has to be known in order to calculate surface tension and viscosity. In previously performed experiments the surface tension of liquid Aluminium droplets in gas metal arcs has been estimated [99]. For this the droplet density

Figure 5.5: Nozzle of gas metal arc with donut cathode.

of Aluminium was estimated to have a constant value although the authors note that the density of Aluminium decreases with increasing temperature. This leads together with the uncertainty in frequency and droplet volume to an uncertainty of 30% of the therein reported values for surface tension. While the density gradient of liquid Aluminium as a function of temperature is relatively small with a value of $0.311\,\mathrm{kg\,m^{-3}\,K^{-1}}$ [3], metals with larger gradients would yield even higher uncertainties. In this work liquid Iron droplets with a density gradient of $0.926\,\mathrm{kg\,m^{-3}\,K^{-1}}$ [3] (which is three times larger than that of aluminum) were analyzed. Hence it is necessary to take the temperature influence on the density into account. This goal has been accomplished in this work by developing two approaches which are subsequently discussed.

Approach 1: Measurement of solidified droplet parameters

In principle there are two ways to determine the mass of a solid spherical droplet. First, the mass can be measured with a precision microbalance. Second, if there is no such balance in place, which was the case in the present work, the diameter d of the spherical droplet can be measured and the mass can be calculated using the known room temperature density:

$$M = \rho V = \rho \frac{4}{3} \left(\frac{d}{2} \right)^3 \pi, \quad \rho = \rho_{RT}\,(\mathrm{at}\,20^{\circ}\mathrm{C}). \tag{5.3}$$

Note that the measurement of the diameter has to be very accurate in order to minimize uncertainties induced by error propagation through the third power in equation 5.3. In order to be able to perform such a measurement, the liquid droplets have to be extracted from the plasma process. This was done by using a 2 mm thick copper plate as a cathode through which a hole was drilled so that the droplets can fall through and quench in a water basin which is placed underneath (see Figure 5.5). In this way, the solidified droplets can be assigned to the images acquired by statistical analysis and subsequently measured. Note that sorting the droplets by size and thus relating them to the high-speed images is much easier if only few droplets are collected within one experiment. In order to obtain a high accuracy of the droplet diameter measurements, two methods have been implemented which allow also an independent comparison of results: First the solidified droplets are analyzed with a Carl Zeiss stereo microscope (SteREO Discovery.V12). The diameters were measured employing a calibrated microscope image with a known magnification. The resulting accuracy of the thus obtained droplet diameters was $4\,\mu$m which was limited mainly due to the optical resolution (see blurry edges in Figure 5.14. Another possibility to measure the droplet diameters is by utilizing a micrometer. Since the maximum resolution of a standard micrometer is around $10\,\mu$m a modified caliper was

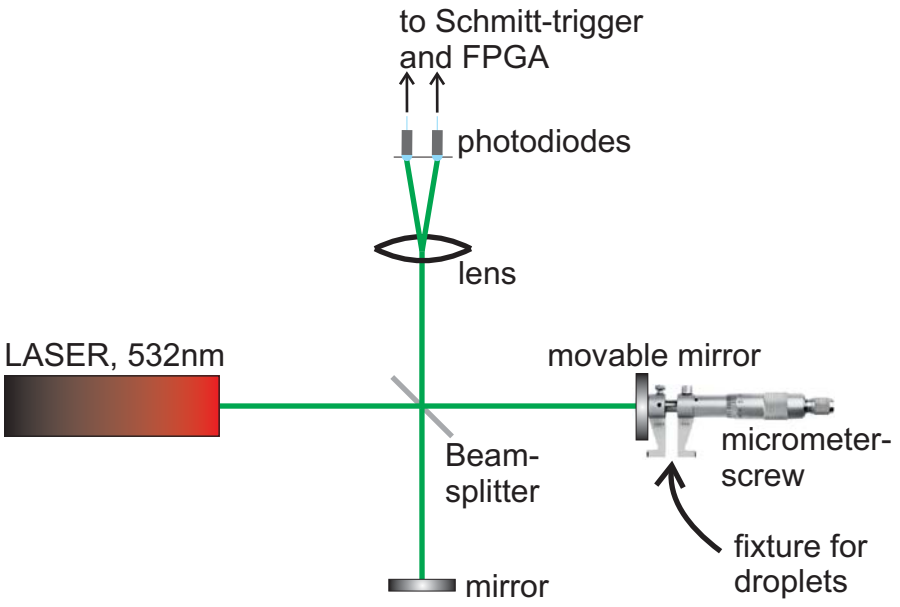

Figure 5.6: Schematic of the Michelson Interferometer to measure solidified droplet diameters.

developed in this work. A Michelson Interferometer (MI) was arranged on a table that is free of vibrations. Then the movable jaw of a micrometer was connected to the movable mirror of the MI (see Figure 5.6). The interference fringes were detected with two fast photodiodes. These were separated by a small distance to detect different phases of the interferogram and thus allow to distinguish between positive and negative movements of the movable mirror. The analog voltage from the photodiodes was digitized using a Schmitt trigger and signal processed with a Field Programmable Gate Array (FPGA) which was programmed to compute the fringecount and the corresponding relative displacement of the micrometer. Employing a laser with a wavelength of 532 nm a theoretical resolution of 266 nm is possible for the measurement of droplet diameters. During each measurement the droplet position was changed more than 10 times and the standard deviation of the diameter which was usually in the range of 1 μm was used for the error propagation (see section 5.5).

Approach 2: Solving a system of linear thermophysical equations

The second approach to determine the droplet mass and droplet density (liquid) that was developed in this work is described subsequently. It enables *in situ* measurements of these parameters and thus *in situ* measurements of surface tension and viscosity. The approach is based on the linear temperature dependency of both surface tension and density. Hence a modified Rayleigh formula (equation 5.4) was employed together with the *surface tension – temperature* equation 5.5 and *density – temperature* equation 5.6 for liquid Iron [3] to built and solve a system of three linearly independent equations:

$$\sigma = 0.5 \cdot \pi^2 f^2 \rho R_0^3, \tag{5.4}$$

$$\sigma = c_3 + c_4 \left(T - T_{\mathrm{ref}}\right), \tag{5.5}$$

$$\rho = c_1 - c_2 \left(T - T_{\mathrm{ref}}\right), \tag{5.6}$$

where $c_1 = 7034.96\,\mathrm{kg\,m^{-3}}$, $c_2 = 0.926\,\mathrm{kg\,m^{-3}\,K^{-1}}$, $c_3 = 1.92\,\mathrm{N\,m^{-1}}$, $c_4 = -3.97 \cdot 10^{-4}\,\mathrm{N\,m^{-1}\,K^{-1}}$ are material constants, $T_{\mathrm{ref}} = 1811.0\,\mathrm{K}$ is the melting point of Iron and R_0 is the radius of the spherical droplets. The latter was measured *in situ* from the high-speed images as-

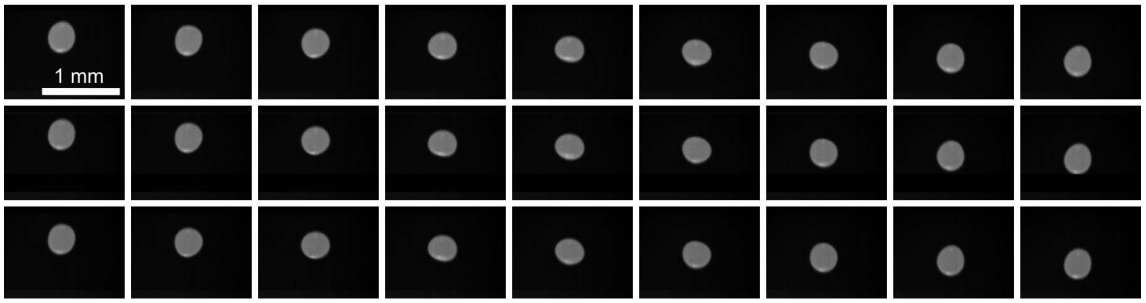

Figure 5.7: Oscillation of liquid Iron droplet (Emission at 650 nm).

suming axially symmetric droplet oscillations. Here the product of volume with density additionally yields the unknown droplet mass. The use of reference data is a drawback of this technique since values for $c_{1,2,3,4}$ and T_{ref} have to be present in literature. On the other hand *in situ* surface tension and viscosity measurements can be performed in an industrial gas metal arc process without the otherwise time consuming collection of droplets for which changes to the electrode configuration are needed. The inclusion of the temperature dependency of the liquid droplet density for surface tension and viscosity measurements was accomplished for the first time and has been published in [6]. This is advantageous especially for materials which have high density gradients - like Iron, since estimation of the density would yield large uncertainties in the calculation of surface tension and viscosity.

5.4 Time- and frequency study of free falling droplets and results of thermophysical droplet parameters and droplet temperature

First, experiments without modifications to the cathode will be discussed. These make use of the *in situ* approach by solving a system of linear thermophysical equations (5.4, 5.5 and 5.6). An image sequence showing a sample droplet is displayed in Figure 5.7. Here every fourth image is shown from the original high-speed sequence which was obtained with a frame rate of 22700 fps. Vertical and horizontal radii were calculated from the droplet edge contours and are displayed in Figure 5.8. The negative gradient in the radii which can be noted from Figure 5.8 will be discussed later. A Fast Fourier Transformation (FFT) was employed to calculate oscillation frequencies of both radii. The result is displayed in Figure 5.9. The frequency corresponding to the maximum of the FFT was substituted in equation 5.4 and the system of equations was solved for the second oscillation mode $(l = 2)$. The resulting values for surface tension σ, density ρ and temperature T yield:

$$\sigma = 1.46 \pm 0.15\,\mathrm{N\,m^{-1}} \tag{5.7}$$

$$\rho = 5960 \pm 350\,\mathrm{kg\,m^{-3}} \tag{5.8}$$

$$T = 2970 \pm 380\,\mathrm{K} \tag{5.9}$$

The given uncertainties result from the error propagation calculations discussed in section 5.5.

As noted before, the radii shown in Figure 5.8 display a negative gradient. This can be ascribed to evaporation of the droplet which makes sense because first, the droplet is

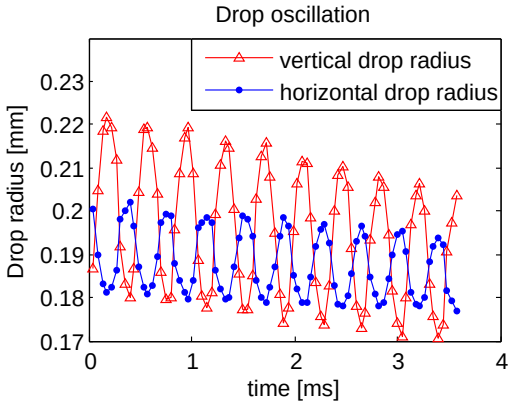

Figure 5.8: Radii of the oscillating Iron droplet in vertical and horizontal direction.

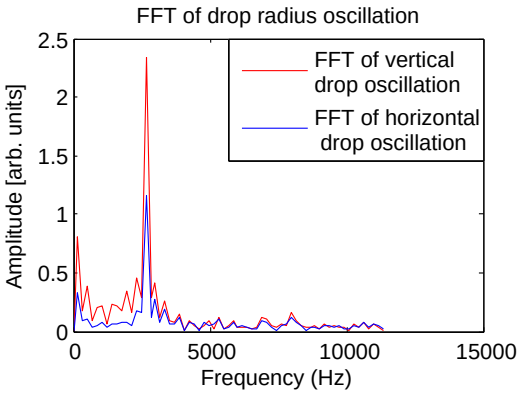

Figure 5.9: FFT of droplet oscillation in vertical and horizontal direction.

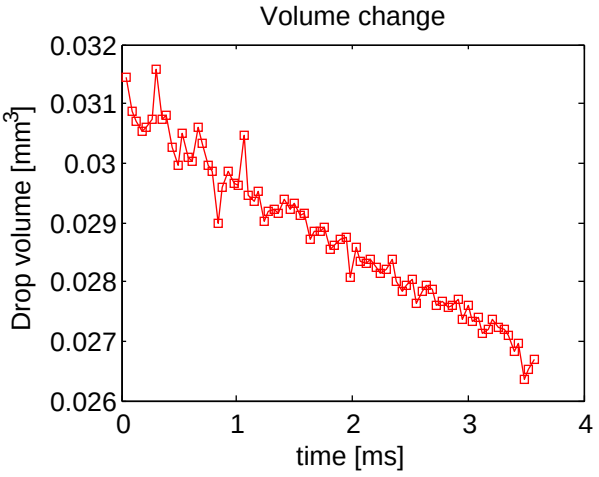

Figure 5.10: Volume change showing evaporation during droplet oscillation.

surrounded by plasma and second, the calculated droplet temperature of $2970 \pm 380\,\mathrm{K}$ is in the vicinity of the boiling point of liquid Iron. In order to support this hypothesis, the droplet volume and volume change with time was calculated. Therefor the radii a and b were employed to calculate ellipsoids with volume V:

$$V = \frac{4}{3}\pi \cdot a^2 \cdot b. \tag{5.10}$$

The resulting droplet volume is plotted versus time in Figure 5.10 and clearly displays the reduction of volume. As seen from Figure 5.10 the volume changes by $0.005\,\mathrm{mm}^3$ within $3.5\,\mathrm{ms}$. The power that is necessary to evaporate $0.005\,\mathrm{mm}^3$ Iron in $3.5\,\mathrm{ms}$ will be estimated in what follows. Assuming a droplet temperature of $3110\,\mathrm{K}$ (which is in the vicinity of the measured $2970\,\mathrm{K}$ and for which an enthalpy of vaporization is given in literature) the droplet density yields $5832\,\mathrm{kg\,m^{-3}}$ according to equation 5.6. With an enthalpy of vaporization of $349\,\mathrm{kJ\,mol^{-1}} = 6.25\,\mathrm{kJ\,g^{-1}}$ [22] the resulting necessary energy yields $0.18\,\mathrm{J}$. This corresponds to a power of $51\,\mathrm{W}$. In order to verify if this power can be provided by the plasma, the power which is radiating on the droplet will be estimated in what follows by assuming a black body radiation of the plasma which surrounds the droplet and a plasma temperature in the range of 7000 to $8000\,\mathrm{K}$ in the arc center [89]. By application of

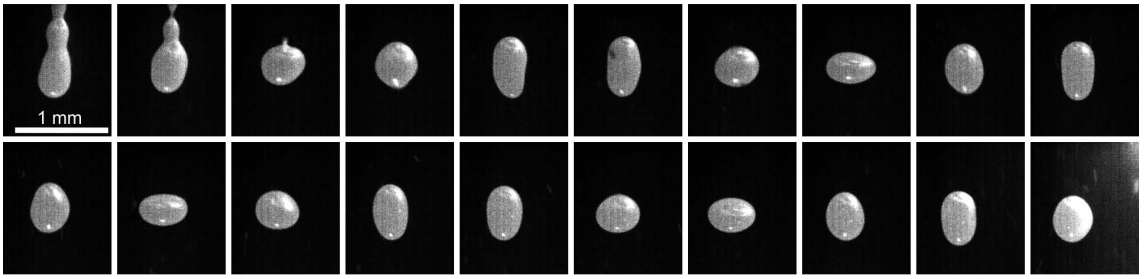

Figure 5.11: Formation and oscillation of liquid Iron droplet beneath cathode.

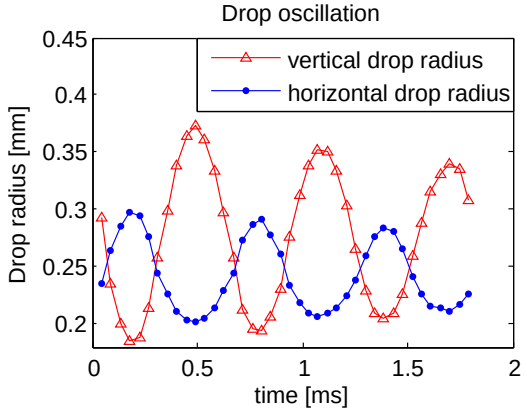

Figure 5.12: Radii of the oscillating Iron droplet in vertical and horizontal direction.

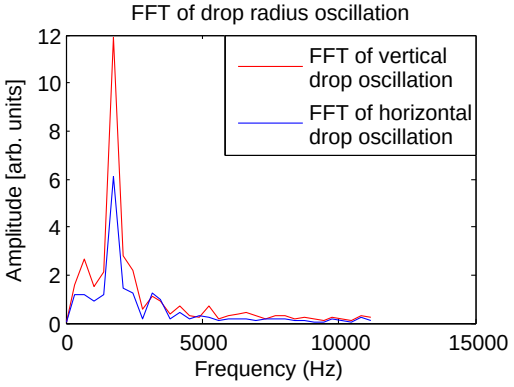

Figure 5.13: FFT of droplet oscillation in vertical and horizontal direction.

the Stefan-Boltzmann law, the radiating power on a droplet with 0.2 mm diameter yields a value in between 70 W to 120 W which is in the same order of magnitude as the power necessary for evaporation. Furthermore, an additional heating of the droplet can be provided by convection which was not considered in this evaluation. Another theoretical explanation of the decrease in droplet volume could be cooling of the droplet. However, a volume change which was observed for the analyzed droplet would correspond to a droplet temperature decrease of more than 1000 K. What contradicts a possible cooling of a droplet is that the observed volumes stay constant for droplets that have been separated from the main plasma column (see e.g. Figure 5.12). If the decrease in droplet size had resulted from droplet cooling it would have been even more visible in the radii of liquid droplets that have been extracted from the main plasma. However, a straightforward calculation of viscosity applying Lamb's equation is not possible due to the decrease in the overall radii depicted in Figure 5.8. Hence the subsequently described experimental results make use of the donut cathode setup. Here the droplets fall through and are recorded during free fall below the cathode (see Figure 5.3, right).

Figure 5.11 shows an image sequence of such droplet. On the first three images the detachment of the droplet from the wire is visible. This process occurs already under the cathode where almost no more plasma is present. The edge contour was extracted as described in section 5.3.1 and the resulting time evolution of the vertical and horizontal droplet radii is depicted in Figure 5.12. The droplet oscillation frequency shown as a maximum in the displayed spectrum of Figure 5.13 was first substituted into the system of equations (5.4, 5.5 and 5.6) which was solved and yields *in situ* paramters for droplet mass, surface tension, temperature and density as shown in the first row of Table 5.1.

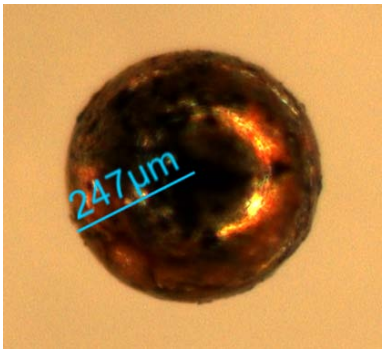

Figure 5.14: Microscope image of solidified droplet.

Method of evaluation	Droplet mass [mg]	Surface tension [$\mathrm{N\,m^{-1}}$]	Temperature [K]	Density (liquid) [$\mathrm{kg\,m^{-3}}$]
Sys. of eq.	0.48 ± 0.04	1.7 ± 0.2	2300 ± 300	6600 ± 300
Droplet diam. via microscope	0.497 ± 0.006	1.79 ± 0.04	2100 ± 100	6730 ± 90
Droplet diam. via mod. caliper	0.510 ± 0.002	1.83 ± 0.02	2040 ± 50	6830 ± 50

Table 5.1: Comparison of results from droplet mass, surface tension, temperature and density of a liquid Iron droplet with different methods of evaluation.

The droplet shown in Figure 5.11 has been captured in a water basin which was placed underneath the cathode. The solidified, almost perfectly spherical droplet was analyzed subsequently yielding the room temperature diameter. In this work possible oxidation of the droplet and a volume change associated with such oxidation during the solidification process was not considered. A microscope image of the solidified droplet is shown in Figure 5.14. The droplet diameter was calculated from the calibrated microscope image yielding a mean diameter of $494\,\mu\mathrm{m}$ with an uncertainty of $4\,\mu\mathrm{m}$ which results mainly from blurry edges. Employing a room temperature density of $7874\,\mathrm{kg\,m^{-3}}$ the droplet mass results to $0.497\,\mathrm{mg}$. A second evaluation of the droplet diameter was carried out with the previously described micrometer which is based on a Michelson Interferometer (section 5.3.1). Here the mean diameter yields a value of $498.4\,\mu\mathrm{m}$ with a standard deviation of $1.1\,\mu\mathrm{m}$. The standard deviation was calculated from 10 measurements of the droplet diameter in which the droplet position was always changed between two measurements. The thus obtained standard deviation of $1.1\,\mu\mathrm{m}$ is different from the theoretically possible resolution of the measurement setup of $266\,\mathrm{nm}$ because of a small asphericity of the droplet. Thus the value of $1.1\,\mu\mathrm{m}$ was utilized for the error propagation described in section 5.5. With a mean diameter of $498.4\,\mu\mathrm{m}$ a droplet mass of $0.510\,\mathrm{mg}$ has been determined. The resulting values for the liquid droplet density, surface tension and temperature are shown in the second and third row of Table 5.1. Values of temperatures and densities given in Table 5.1 were calculated based on equations 5.5 and 5.6 and their uncertainties were calculated by error propagation of the upper and lower bounds of surface tension. The latter were calculated in turn including the resolution of the high-speed camera, the blurring induced uncertainty of the microscope image and the standard deviation of the diameters measured with the modified micrometer, respectively, as well as the uncertainty in the frequency measurement.

The viscosities of the droplets that were generated with the donut shaped cathode setup

Method of evaluation	Viscosity [mPa s] (vertical oscillation) related temperature interval [K]	Viscosity [mPa s] (horizontal oscillation) related temperature interval [K]
Sys. of eq.	9 ± 2 $[1500, 1860]$	3.2 ± 0.5 $[2070, 2370]$
Droplet diam. via microscope	8 ± 2 $[1540, 1920]$	2.9 ± 0.3 $[2150, 2450]$
Droplet diam. via mod. caliper	8 ± 2 $[1530, 1910]$	2.9 ± 0.3 $[2150, 2450]$

Table 5.2: Comparison of results for viscosity from vertical and horizontal droplet oscillations with different methods of evaluation. Viscosities derived from the vertical oscillation are too high due to initial modulated damping as described by Prosperetti [86] while measurement variations of the damping of horizontal oscillations can be caused by measurement uncertainties.

were also investigated employing Lamb's equation 5.2. Therefor a non-linear least squares fit was employed to fit the oscillation envelope y (e.g. visible in Figure 5.12):

$$y \propto \exp(-\Gamma t), \tag{5.11}$$

where Γ is the damping constant of the oscillation. Uncertainties of this measurement were calculated through error propagation employing the 68.3% confidence intervals of the fit procedure as well as the uncertainty in the measured droplet radii. The resulting values for viscosities measured with the different methods of evaluation and vertical and horizontal droplet oscillation, respectively, is shown in Table 5.2. The corresponding temperature intervals were calculated employing the following *viscosity-temperature* correlation:

$$\log_{10}\left(\eta/\eta^0\right) = -c_5 + \frac{c_6}{T}, \text{ [3]} \tag{5.12}$$

where $\eta^0 = 1\,\mathrm{mPa\,s}$, $c_5 = 0.7209$ and $c_6 = 2694.95\,\mathrm{K}$. The viscosities for the vertical oscillation are too high to be plausible. Prosperetti gave a possible explanation for this reproducible behavior [86]: The initial detachment from the wire tip as it can be seen from Figure 5.7, pictures 1,2,3 can lead to additional damping of the vertical oscillation. Hence such a damped oscillation approaches only asymptotically the behavior of a damped harmonic oscillation. As a result the damping constants of consecutive oscillation amplitudes may differ and converge with time towards a constant value. Thus, differences in damping constants between the two consecutive oscillation amplitudes shown in Figure 5.12 have been evaluated for the vertical and horizontal oscillation. The damping constants of the vertical oscillation differ by 40% which results in overestimation of values for the vertical oscillation displayed in Table 5.2. In contrast to this, the damping constants of the horizontal oscillation differ by 10% which can be mainly ascribed to measurement uncertainties of the exact oscillation amplitudes. Instead of evaluating every single oscillation, the employed non-linear least squares fit of the oscillation envelope allows for averaging of differences of damping constants from consecutive oscillation amplitudes. Additionally, the fit procedure allows the determination of measurement uncertainties through error propagation of the fit-related confidence intervals. Finally, it is worth mentioning that, in the case of the horizontal oscillation, the viscosity related temperature intervals shown in Table 5.2 match very well with the surface tension related temperatures shown in Table 5.1.

5.5 Sources of error and analysis of uncertainties

The errors which arise from uncertainties which are inherent to every measurement are described in what follows. One of such errors occurs due to the discrete spatial resolution of the high-speed images. The implied discretization error for the droplet which was surrounded by plasma is $\sigma_{x,1} = 8\,\mu$m and $\sigma_{x,1} = 6\,\mu$m for the droplet which originated below the cathode separated from the plasma. The noise of the employed electronic equipment (e.g. high-speed camera) was neglected as well as possible overestimations of the droplet surface area due to the brightness of the droplets since there were no areas of overexposure during the measurements. A residual error arising due to a possible droplet movement along the observed line-of-sight and a resulting magnification of the droplets was neglected because of the small overall traveling distances of the droplets. Uncertainties due to blurry edges while measuring the droplet diameter with the microscope have been taken into account and yield a value of $\sigma_{x,2} = 4\,\mu$m. The standard deviation of the alternative measurement of the solidified droplet diameter with the modified Michelson Interferometer was $\sigma_{x,2} = 1.1\,\mu$m which was due to a small asphericity of the solidified droplet. Impurities of the Iron and shielding gas as well as possible oxidation of droplets were neglected for evaluations making use of reference data. However, for calculations that do not utilize reference data, the obtained values for surface tension, viscosity and related parameters are correct – that is true also if droplets are oxidized or already reacted with surfactants if these values do not change during the image acquisition with the high-speed camera. Porosity which droplets might have gained during the solidification process was neglected in this work. Such porosities would affect the room temperature density of Iron which was employed to calculate the droplet mass. Alternatively, the mass of porous droplets can be determined utilizing a precision microbalance in future studies. Constants used in equations 5.5 and 5.6 were employed without upper and lower limits and assumed to be valid in the temperature range experienced by the droplets. A possible electrical charge accumulation on the droplets which travel through the plasma and the resulting influence on the analysis have been neglected. Because of the high thermal conductivity of the droplets the droplet temperature was assumed to be uniform. An important result from previous investigations is that droplet rotation and/or external forces acting on them would result in a splitting of the Rayleigh frequency towards more frequencies [20, 26]. The influence of droplet rotation or external forces on surface tension, viscosity and related parameters can be neglected in this work since no such frequency splitting is visible in Figures 5.9 and 5.13 [67, 68, 71] (within the considered uncertainties in frequency measurements). This assumption can be substantiated for though the droplets are surrounded by plasma during the *in situ* measurements (thus presumably exposed to higher shear forces) and extracted from the plasma in the experiments with the donut cathode (thus presumably exposed to less shear forces), there is always only one frequency peak observed in the oscillation spectra. The uncertainties in measured oscillation frequencies yield $\sigma_{x,3} = 0.6\%$ for the droplet surrounded by plasma and $\sigma_{x,3} = 1\%$ for the droplet originated under the cathode (half of the time interval between the frames divided by the droplet observation time). The error arising from the determination of damping constants from the non-linear least squares fit of the oscillation envelope which was employed to determine viscosity was also taken into account. The related standard deviation of the damping constant of the vertical droplet oscillation was $\sigma_{x,4} = 36.8\frac{1}{s}$ and $\sigma_{x,4} = 6.5\frac{1}{s}$ for the horizontal droplet oscillation. The described errors due to spatial image resolutions, measurements of droplet diameters, oscillation frequencies and damping

constants were assumed to be uncorrelated. Hence the following calculation of an error σ_A was employed by error propagation:

$$\sigma_A = \sum_i \left| \frac{\partial A}{\partial x_i} \right| \sigma_{x,i}, \tag{5.13}$$

where $A = f(x_1, x_2, ..., x_n)$ and x_i is the quantity to be measured with an uncertainty $\sigma_{x,i}$. Values for droplet masses, densities, surface tensions, viscosities and temperatures which are listed e.g. in Tables 5.1 and 5.2 are written in the form $A \pm \sigma_A$.' [6]

Chapter 6

Conclusion and Outlook

In this work three diagnostics have been developed in order to characterize multi dimensional and transient plasma processes. First, a fundamental configuration of a transferred Argon arc has been studied. Then the degree of complexity has been increased by applying pulsed currents, which cause transient phenomena (part 1 and 2). Further, the analysis of liquefied metal droplets moving through an arc column towards a cathode under transient conditions has been performed and their impact on the distribution of current in the cathode has been shown (part 2 and 3).

In the first part of this thesis a non-intrusive optical plasma diagnostic has been introduced which is based on the visualization of the object of interest in two spectral bands by means of high-speed imaging and subsequent analysis of images obtained. An experimental setup has been developed which allows imaging of these spectral bands simultaneously on a single camera chip by the use of interference filters and a set of mirrors. Utilization of a high-speed camera allows the determination of three-dimensional plasma densities, temperatures and conductivities with a high temporal resolution. The evaluation method involves a matching of simulated emission coefficients with Abel-inverted measured emission coefficients. To accomplish this, two different types of Abel inversion algorithms have been developed. One is based on spline functionals which have been described in literature. The other makes use of an implied physical model which allows for an analytic inversion of intensity profiles. The obtained results have been justified by a thorough analysis of error sources as well as the comparison to stationary measurements with a classical spectrometer. The latter have been evaluated by four independent methods including a single line and line ratio method, the Fowler-Milne method as well as the quadratic Stark broadening of an atomic transition line. It has been shown that resulting plasma temperatures agree very well within those methods and within the results obtained with the high-speed diagnostic. Moreover, it has been shown that the high-speed diagnostic provides an additional advantage by enabling the simultaneous evaluation of two spectral intervals: For the described experimental parameters a departure from *single-temperature LTE* towards a *two-temperature LTE* would still yield correct electron temperatures. The sensitivity of the experimental approach and the capability to determine the quantitative electrode attachment of an arc have been shown by the analysis of a dc pulsed process. While the utilization of a classical spectrometer only allows to collect a signal in a certain plane, the camera based high-speed setup allows to directly image the whole arc. Thus transient multi-dimensional processes can be studied in one cycle of a measurement. In contrast to this, classical spectroscopy relies on the reproducibility of the studied process to get a map of arc properties because several measurements of different planes need to be performed. The boundary condition of an axially symmetric arc could be omitted by evaluating measurement results with a generalized Abel inversion procedure [56]. Thus elliptically symmetric density distributions could be reconstructed. Alternatively, collection and filtering of radiation from different directions would enable an entirely tomographic approach [58]. Also different gas mixtures used in industrial processes may be analyzed in future by changing the central wavelength of one or both spectral filters. In this way the

plasma temperature can be first obtained by analyzing only transition lines of for example Argon. The *local* three-dimensional gas composition could be obtained by measurement of local emission coefficients of atomic lines of other gas species utilizing different sets of filters. This could be achieved either in a reproducible process and by performing consecutive experiments or by duplication of the experimental setup and simultaneously measuring transition lines of different atomic species.

The electrical conductivities measured of a stationary free burning arc have also been compared to current density distributions which have been measured by the diagnostic introduced in the second part of this thesis. The agreement of these results enables an independent validation of the spectral three-dimensional high-speed diagnostic and the diagnostic of current density distributions. By utilization of Hall-effect sensors, the latter allows a reconstruction of current density distributions by evaluating current carrying cross sections of a free burning arc. This was achieved by experimentally integrating the magnetic flux density distribution along the circumference of each cross section and solving Ampere's circuital law for a Gaussian distributed axially symmetric current density. The Gaussian distribution has been justified by assuming a radial diffusion profile with electrical conductivity as approximately constant diffusion parameter. Additionally, a generalized approach for arbitrary current density distributions has been described. Current densities in pulsed arcs may be measured in future experiments if Hall-effect devices are employed which provide a high sensitivity and time resolution like the utilized digital Hall-sensor HAL2850 (which provides a acquisition rate of 2 kHz). Preliminary magnetic flux density measurements have been made in a dc pulsed gas metal arc process where the influence of the cathode temperature on the distribution of current has been shown experimentally. At last magnetic flux densities have been measured in the vicinity of the current carrying part of a cold electrode. But by changing the direction of the arc movement with respect to the cathode, magnetic flux densities have been measured also in the vicinity of the current carrying part of a hot electrode. This current carrying part is heated by the arc as well as by the liquid metal droplets which cumulate on the cathode surface. The clearly visible and reproducible change in the magnetic flux density distribution near the hot cathode suggests the redistribution of current due to the increased resistivity of the heated metal areas. From these magnetic flux density measurements, also current density distributions may be reconstructed in future evaluations by the following procedure: First, a simulation of current density functionals with a limited number of variables could be performed. The functionals should be chosen based on several assumptions about the current density distribution in gas metal arcs. These assumptions could for example distinguish between a current carrying and a non-current carrying metal vapor core of the arc. Then, magnetic flux densities may be calculated from the different current density distributions. Finally an optimization of the variables from the current density functionals may be performed until a best fit of measured and calculated magnetic flux densities is reached. Thus it would be possible to test hypotheses like a current minimum in the arc core which contains metal vapor by observing differences in the resulting calculated and measured magnetic flux densities. Another possibility for an evaluation would be to validate current density simulations of gas metal arcs that have been published recently (see for example [92]). Magnetic flux densities resulting from these simulated current densities could be calculated and compared with measured ones.

Presence of liquid metal droplets in the arc is crucial from a phenomenological point of view. Indeed, such droplets and the arc intensively interact with each other. In the hot plasma environment droplets undergo heating and evaporation consuming energy from

the arc, which result in a change of plasma composition and thermophysical properties. Moreover, as shown in part 2, presence of droplets affects current transfer not only through the arc itself, but also inside the electrode. In order to investigate the thermophysical properties of these liquid metal droplets, an *in situ* diagnostic has been introduced in the third part of this thesis. The diagnostic makes use of high-speed optical measurement of intrinsic droplet oscillations. The developed image processing algorithm allows to accurately extracting the edge contour of the oscillating droplets. Different experimental and theoretical approaches have been developed to determine the droplet mass and thus to include the effect of temperature on droplet density. The droplet mass was obtained either by *in situ* evaluations utilizing reference data or alternatively by capturing and analyzing solidified droplets. The latter approach uses the measurement of the droplet diameter with different methods and subsequent translation in droplet volume and droplet mass. The uncertainties involved in this approach are caused by possible droplet oxidation or the increase of porosity during the solidification process which may affect the assumed room-temperature droplet density. These uncertainties can be avoided in future experiments: By utilization of a precision microbalance which was not available during this work, the droplet mass can be accurately determined. The subsequently performed frequency analysis of the oscillating droplet shape yields accurate results of surface tension (with $\pm 1\%$ accuracy). Droplet viscosity was obtained by accurately measuring the damping of the droplet oscillation. Here special care was taken since oscillations may deviate from the least damped normal mode of a harmonic oscillation. In those cases an overestimation of viscosity is inherent in the evaluation procedure. As shown, this can be avoided by ensuring that the damping rate of consecutive oscillations already converged to a constant value. Droplet temperatures have been calculated independently from the obtained surface tension and viscosity data. The agreement of calculated temperatures allows for an independent validation of the introduced plasma diagnostic. The thorough analysis and inclusion of error sources by error propagation calculations enables accurate measurements of thermophysical droplet properties like density, surface tension and viscosity in gas metal arcs. One practical limitation of the diagnostic is the droplet size. Liquid iron droplets which have been analyzed in this work had diameters in the range of $0.5\,\mathrm{mm}$. Droplets which are too big perform only few oscillations and are often prone to additional surface waves which interfere with the evaluation. Droplets which are too small oscillate perfectly around a sphere but oscillation frequencies increase to values far above hundreds of kHz where available high-speed cameras offer too slow repetition rates. In future experiments the introduced diagnostic could be applied to any process where metal droplets are formed and perform damped harmonic oscillations, e.g. industrial welding, cutting or spraying processes.

In future, further development of the introduced plasma diagnostics and further comparison of the results obtained by each diagnostic should be possible. That way the spectral three-dimensional high-speed diagnostic could be applied on gas metal arcs. A possible scenario for an experimental procedure which would accomplish this will be outlined in what follows. In a first step it may be assumed that the arc core and the surrounding plasma sheath can be divided into a region of pure metal plasma (Fe, Al, etc.) and a region of pure nobel gas (Ar, He, etc.), respectively. This is reasonable as it is visible from the images of Al/Ar and Fe/Ar arcs where the Argon plasma and the metal vapor core are clearly delimitable [72]. Metal vapor is concentrated within a narrow region at the arc center. Hence the temperature of the Argon plasma which surrounds this metal core may be measured by the diagnostic introduced. Therefore the Argon plasma temperature

could be measured at areas where no metal vapor is in the line-of-sight. Then it would be possible to eliminate the emission of Argon which arises in the line-of-sight of the metal vapor core. This is possible because local emission coefficients of Argon plasma are resulting from the employed Abel inversion. Thus, further assuming axial symmetry, the emission coefficients of the volume elements in front and behind the metal vapor core can be subtracted from the radiation of the metal vapor. Finally the remaining metal plasma core can be analyzed by the same procedures introduced in the first part of this thesis by utilization of appropriate filters for the corresponding metals. The Saha equation and the plasma composition calculations should be solved for the metal plasma instead of Argon. A further sophistication of this approach could include transport phenomena inside the gas metal arc [refs INP]. With this approach it would be possible to determine spatially and temporally resolved plasma densities and temperatures in gas metal arcs. This could be compared to current density measurements in gas metal arcs utilizing Hall-effect devices. The results obtained by the *in situ* diagnostic for thermophysical droplet properties could be used to study heat transfer mechanisms inside the plasma. As shown in section 5.4, the droplets which are surrounded by plasma are continuously evaporating very small amounts of metal vapor (around $0.0015\,\mathrm{mm}^3/\mathrm{ms}$). Employing the enthalpy of vaporization the necessary power for this evaporation can be calculated. Since the evaporation is a result of the surrounding plasma, this power is provided by the plasma and allows to study the heat transfer of the plasma towards the droplets. The delivered power could be for example divided into a part of radiative power and a part of convective power. The latter could be estimated for example by additional knowledge of the plasma velocity which in turn could be determined for example by laser scattering [59, 43, 69]. In a first step the radiative power could be assumed to be dissipated by a black body and thus the Stephan-Boltzmann law would be applied to calculate radiation transport. Alternatively more sophisticated models of radiation transport could be employed [39, 102]. Finally, plasma temperatures of gas metal arcs which are obtained by the previously described improved optical high-speed diagnostic or current densities measured with an improved magnetic flux density diagnostic may be included in those evaluations of heat transfer mechanisms.

Appendix A

Estimation of electrical conductivity

An electrical current density $\vec{j}_{el} = -en_e\vec{v}_{e,\text{drift}}$ is a result of electrons moving with a drift velocity $\vec{v}_{e,\text{drift}}$ in an electric field $\vec{E}$. This drift velocity is limited by the electrical conductivity σ_{el} of the current carrying matter, in this case the plasma:

$$\vec{j}_{el} = \sigma_{el}\vec{E}. \tag{A.1}$$

The movement of the electrons in the plasma can be described by the following equation which is the sum over all forces F:

$$m_e\frac{d\vec{v}_{e,\text{drift}}}{dt} = \sum_i F_i = -e\vec{E} - \gamma\vec{v}_{e,\text{drift}}, \tag{A.2}$$

where γ is a constant which is described by the characteristic impact timescale τ_{impact} which is the average time between two electron impacts:

$$\frac{\gamma}{m_e} = \frac{1}{\tau_{\text{impact}}} \approx n_{\text{scat}}\sigma_{\text{scat}}v_{e,th} \approx v_{e,th}\sum_{i=0}^{N} n_{A,i}\sigma_{e-A_i}, \tag{A.3}$$

where σ_{e-A_i} is the cross section for the reduction in momentum of the electrons due to scattering with atomic species A_i. Note that equation A.3 is only valid if $|\vec{v}_{e,\text{drift}}| \ll |\vec{v}_{e,th}|$, where $v_{e,th} \approx \sqrt{\frac{k_B T_e}{m_e}}$ is the thermal velocity of the electrons. In a stationary state $\frac{d\vec{v}_{e,\text{drift}}}{dt} = 0$ it follows from equation A.2:

$$\vec{v}_{e,\text{drift}} \approx \frac{-e\vec{E}}{\gamma} \approx \frac{-e\vec{E}\tau_{\text{impact}}}{m_e}. \tag{A.4}$$

Hence the current density $\vec{j}_{el}$ yields the electrical conductivity σ_{el}:

$$\vec{j}_{el} = -en_e\vec{v}_{e,\text{drift}} \approx \underbrace{\frac{e^2 n_e \tau_{\text{impact}}}{m_e}}_{\sigma_{el}}\vec{E}. \tag{A.5}$$

The cross sections σ_{e-A_i} can be calculated by the average of the scatterd fraction of momentum $1-\cos\chi$ over all possible velocities and over all possible scattering angles. The latter yields

$$\int_{b_{\min}}^{b_{\max}} (1-\cos\chi)\,2\pi b db \approx \pi\left(\frac{q_1 q_2}{4\pi\varepsilon_0}\right)^2\left(\frac{1}{\mu v_{\text{rel}}^2/2}\right)^2 \int_{b_{\min}\approx\frac{q_1q_2}{4\pi\varepsilon_0}\frac{1}{\mu v_{\text{rel}}^2/2}}^{b_{\max}\approx\lambda_D} \frac{1}{b}db, \tag{A.6}$$

where $\chi \approx \frac{q_1 q_2}{4\pi\varepsilon_0}\frac{1}{\mu v_{\text{rel}}^2/2}\frac{1}{b}$, $\mu = \frac{m_1 m_2}{m_1+m_2}$ is the reduced mass and v_{rel} is the relative velocity between the two charges q_1 and q_2. The average over all velocities of the expression in equation A.6 yields

$$\pi\left(\frac{q_1 q_2}{4\pi\varepsilon_0}\right)^2\left\langle\left(\frac{1}{\mu v_{\text{rel}}^2/2}\right)^2 \int_{b_{\min}=\frac{q_1q_2}{4\pi\varepsilon_0}\frac{1}{\mu v_{\text{rel}}^2/2}}^{b_{\max}=\lambda_D} \frac{1}{b}db\right\rangle \overset{\left\langle\frac{1}{2}\mu v_{\text{rel}}^2\right\rangle\approx k_B T_e}{\approx} \pi\left(\frac{q_1 q_2}{4\pi\varepsilon_0}\frac{1}{k_B T_e}\right)^2 \ln\left(\frac{\lambda_D}{\lambda_L}\right), \tag{A.7}$$

where $\lambda_L = \frac{e^2}{4\pi\varepsilon_0}\frac{1}{k_B T_e}$ is the Landau length which results from the equilibrium between potential energy $\frac{e^2}{4\pi\varepsilon_0}\frac{1}{\lambda_L}$ due to the Coulomb force and thermal energy $k_B T_e$. Thus it follows for the cross sections:

$$\sigma_{e-A_i} \approx i^2 \pi \lambda_L^2 \ln\left(\frac{\lambda_D}{\lambda_L}\right) \qquad , i > 1 \tag{A.8}$$

$$\sigma_{e-A_0} \approx a_0^2 \pi \qquad , a_0 \approx 1.06\text{Å the covalent atom radius} \tag{A.9}$$

and finally for the electrical conductivity:

$$\sigma_{el} \approx \frac{e^2 n_e}{m_e}\left[\sqrt{\frac{k_B T_e}{m_e}}\left(n_{A,0}\sigma_{e-A_0} + \sum_{i=1}^{N} n_{A,i} i^2 \pi \lambda_L^2 \ln\left(\frac{\lambda_D}{\lambda_L}\right)\right)\right]^{-1}. \tag{A.10}$$

This derivation of the electrical conductivity yields a good estimation of the order of magnitude, however values calculated in this study make use of the derivations shown in [15].

Appendix B

Error propagation in non-linear least squares

The datasets $\vec{x}$ and $\vec{y}$ of size N are fitted by the model $F(\vec{x},\vec{p}) = \vec{y}$ with parameters $\vec{p}$ of size P. The least squares problem is written as:

$$\min S = \min \sum_{i=0}^{N-1} (y_i - F(x_i,\vec{p}))^2 . \tag{B.1}$$

The condition on minimum of S is given by the system of equations:

$$\frac{\partial S}{\partial p_j} = 2 \sum_{i=0}^{N-1} \left.\frac{\partial F}{\partial p_j}\right|_i \cdot (y_i - F(x_i,\vec{p})) = 0 \quad j = 0 \ldots P-1 \tag{B.2}$$

This can be written in matrix form as (in the vicinity of $\vec{p}_0$: $F = F(p_0) + \partial F/\partial p \Delta\vec{p} = F(p_0) + J\Delta\vec{p}$)

$$J^T \left[\vec{y} - F(x,\vec{p}_0)\right] - J^T J \cdot \Delta\vec{p} = 0 \tag{B.3}$$

where J is the jacobian matrix [NxP] of the model (N rows and P columns). An iterative approach to optimal parameters is given by the solution of equation:

$$J^T J \cdot \Delta\vec{p} = J^T \left[\vec{y} - F(x,\vec{p}_0)\right] \tag{B.4}$$

This system of linear equations is solved by the QR decomposition of the matrix J, where the matrix Q is orthogonal ($Q^T Q = I$) and R is upper triangular. This leads to the transformation:

$$R^T R \cdot \Delta\vec{p} = R^T Q^T \left[\vec{y} - F(x,\vec{p}_0)\right] \tag{B.5}$$

or

$$R \cdot \Delta\vec{p} = Q^T \left[\vec{y} - F(x,\vec{p}_0)\right] . \tag{B.6}$$

The change in the fitted parameter δp_i is given by

$$\delta p_i = \sum_j \frac{\delta p_i}{\delta y_j} \delta y_j \tag{B.7}$$

The covariance matrix can be written in the terms of errors of data

$$C_{nk} = \sum_{i,j} \frac{\delta p_n}{\delta y_i} \frac{\delta p_k}{\delta y_j} \delta y_i \delta y_j \tag{B.8}$$

for uncorrelated data $\delta y_i \delta y_j = \sigma_i^2 \delta_{ij}$ giving

$$C_{nk} = \sum_i \frac{\delta p_n}{\delta y_i} \frac{\delta p_k}{\delta y_i} \sigma_i^2 . \tag{B.9}$$

When computing the covariance matrix for unweighted data, i.e. data with unknown errors, the weight factors $1/\sigma_i^2$ in this sum are replaced by the single estimate σ^2, which is the computed variance of the residuals about the bestfit model, $\sigma^2 = \sum_i (y_i - F(\vec{p}, x_i))^2/(N - P)$. This is referred to as the variance - covariance matrix. The covariance matrix is given by the $P \times P$ matrix $R^T R$. The variance of parameter p_i is given by the element $\{R^T R\}_{ii}$. The standard deviation is given by the square root of variance multiplied with the value of residual on the set of optimal parameters $\vec{p}^*$:

$$\delta p_i = \sqrt{\{R^T R\}_{ii} \cdot \sigma^2}. \tag{B.10}$$

Bibliography

[1] AMPÈRE, A.-M. : *Théorie des phénomènes électro-dynamiques, uniquement déduite de l'expérience*. Paris : Méquignon-Marvis, 1826

[2] ANDREAS, J. ; HAUSER, E. ; TUCKER, W. : Boundary tension by pendant drops. In: *J. Phys. Chem.* 42 (1938), 1001-1019. http://dx.doi.org/10.1021/j100903a002

[3] ASSAEL, M. ; KAKOSIMOS, K. ; BANISH, R. ; BRILLO, J. ; EGRY, I. ; BROOKS, R. ; QUESTED, P. ; MILLS, K. ; NAGASHIMA, A. ; SATO, Y. ; WAKEHAM, W. : Reference data for the density and viscosity of liquid aluminum and liquid iron. In: *J. Phys. Chem. Ref. Data* 35 (2006), 285-300. http://dx.doi.org/10.1063/1.2149380

[4] BACHMANN, B. ; KOZAKOV, R. ; GÖTT, G. ; EKKERT, K. ; BACHMANN, J.-P. ; MARQUES, J.-L. ; SCHÖPP, H. ; UHRLANDT, D. ; SCHEIN, J. : High-speed three-dimensional plasma temperature determination of axially symmetric free burning arcs. In: *J. Phys. D: Appl. Phys.* 46 (2013), 125203. http://dx.doi.org/10.1088/0022-3727/46/12/125203

[5] BACHMANN, B. ; SIEWERT, E. ; SCHEIN, J. : Chapter 2: Development of innovative diagnostics for characterization of material transfer and plasma properties in tungsten inert gas welding (TIG) and gas metal arc welding (GMAW). In: *Arc welding - Physics and capabilities of gas metal arc welding*, S. 18–33

[6] BACHMANN, B. ; SIEWERT, E. ; SCHEIN, J. : *In situ* droplet surface tension and viscosity measurements in gas metal arc welding. In: *J. Phys. D: Appl. Phys.* 45 (2012), 175202. http://dx.doi.org/10.1088/0022-3727/45/17/175202

[7] BAEVA, M. ; KOZAKOV, R. ; GORCHAKOV, S. ; UHRLANDT, D. : Two-temperature chemically non-equilibrium modelling of transferred arcs. In: *Plasma Sources Sci. Technol.* 21 (2012), 055027. http://stacks.iop.org/0963-0252/21/i=5/a=055027

[8] BARBÉ, J. ; PARAYRE, C. ; DANIEL, M. ; PAPOULAR, M. ; KERNEVEZ, N. : High-Temperature Containerless Viscosity Measurement by Gas-Film Levitation. In: *Int. J. Thermophys.,* 20 (1999), 1071-1083. http://dx.doi.org/10.1023/A:1022698619162

[9] BARTELS, H. : Eine neue Methode zur Temperaturmessung an hochtemperierten Bogensäulen I. Teil. In: *Z. Phys.* 127 (1950), 243-273. http://dx.doi.org/10.1007/BF01338590

[10] BARTELS, H. : Eine neue Methode zur Temperaturmessung an hochtemperierten Bogensäulen II. Teil. In: *Z. Phys.* 128 (1950), 546-574. http://dx.doi.org/10.1007/BF01330037

[11] BARTH, C. : Determination of the local current density by means of tangential Thomson scattering: Experimental setup, feasibility test, and preliminary observations. In: *Rev. Sci. Instrum.* 60 (1989), 2673-2679. http://dx.doi.org/10.1063/1.1140692

[12] BARTLET, T. : *Industrial Control Electronics*. Delmar Cengage Learning, 2006

[13] BENIAMINY, I. ; DEUTSCH, M. : ABEL: Stable, high accuracy program for the inversion of Abel's integral equation. In: *Comput. Phys. Commun.* 27 (1982), 415-422. http://dx.doi.org/10.1016/0010-4655(82)90102-3

[14] BIOT, J.-B. ; SAVART, N.-P.-A. : Note sur le magnétisme de la pile de Volta. In: *Annales de chimie et de physique* (1820)

[15] BOULOS, M. ; FAUCHAIS, P. ; PFENDER, E. : *Thermal plasmas: fundamentals and applications*. New York : Plenum Press, 1994

[16] BROWER, D. ; DING, W. ; TERRY, S. : Measurement of the Current-Density Profile and Plasma Dynamics in the Reversed-Field Pinch. In: *Phys. Rev. Lett.* 88 (2002), 185005. http://dx.doi.org/10.1103/PhysRevLett.88.185005

[17] CALKER, J. ; FISCHER, D. : Über den Einsatz von Spline-Funktionen zur Glättung von Meßwerten bei der Abel-Inversion. In: *Ann. Phys.* 488 (1976), 191-198. http://dx.doi.org/10.1002/andp.19764880305

[18] CHANDRASEKHAR, S. : *Hydrodynamic and Hydromagnetic Stability*. Oxford : Clarendon Press, 1961

[19] CRAM, L. E. ; POLADIAN, L. ; ROUMELIOTIS, G. : Departures from equilibrium in a free-burning argon arc. In: *J. Phys. D: Appl. Phys.* 21 (1988), 418-425. http://stacks.iop.org/0022-3727/21/i=3/a=007

[20] CUMMINGS, D. ; BLACKBURN, D. : Oscillations of magnetically levitated aspherical droplets. In: *J. Fluid. Mech.* 224 (1991), 395-416. http://dx.doi.org/10.1017/S0022112091001817

[21] DAVIS, J. ; BARTELL, F. : Determination of Suface Tension of Molten Materials - Adaptation of the Pendant Drop Method. In: *Anal. Chem.* 20 (1948), 1182-1185. http://dx.doi.org/10.1021/ac60024a015

[22] DESAI, P. : Thermodynamic properties of iron and silicon. In: *J. Phys. Chem. Ref. Data* 15 (1986), 967-983. http://dx.doi.org/10.1063/1.555761

[23] DEUTSCH, M. ; BENIAMINY, I. : Inversion of Abel's integral equation for experimental data. In: *J. Appl. Phys.* 54 (1983), 137-143. http://dx.doi.org/10.1063/1.331739

[24] DRELLISHAK, K. S. ; KNOPP, C. F. ; CAMBEL, A. B.: Partition Functions and Thermodynamic Properties of Argon Plasma. In: *Phys. Fluids* 6 (1963), 1280-1288. http://dx.doi.org/10.1063/1.1706896

[25] EGGERS, J. ; VILLERMAUX, E. : Physics of liquid jets. In: *Rep. Prog. Phys.* 71 (2008), 036601. http://stacks.iop.org/0034-4885/71/i=3/a=036601

[26] EGRY, I. ; GIFFARD, H. ; SCHNEIDER, S. : The oscillating drop technique revisited. In: *Meas. Sci. Technol.* 16 (2005), 426-431. http://stacks.iop.org/0957-0233/16/i=2/a=013

[27] EGRY, I. ; LANGEN, M. ; LOHÖFER, G. : Measurements of thermophysical properties of liquid metals relevant to Marangoni effects. In: *Phil. Trans. R. Soc. Lond.* 356 (1998), 845-856. http://dx.doi.org/10.1098/rsta.1998.0191

[28] EGRY, I. ; LOHOEFER, G. ; JACOBS, G. : Surface tension of liquid metals: results from measurements on ground and in space. In: *Phys. Rev. Lett.* 75 (1995), 4043-4046. http://dx.doi.org/10.1103/PhysRevLett.75.4043

[29] FARMER, A. J. D. ; HADDAD, G. N.: Local thermodynamic equilibrium in free-burning arcs in argon. In: *Appl. Phys. Lett.* 45 (1984), 24-25. http://dx.doi.org/10.1063/1.94990

[30] FARMER, A. J. D. ; HADDAD, G. N.: Rayleigh scattering images in the free burning-argon arc. In: *J. Phys. D: Appl. Phys.* 21 (1988), 426-431. http://stacks.iop.org/0022-3727/21/i=3/a=008

[31] FOWLER, R. H. ; MILNE, E. A.: The intensities of absorption lines in stellar spectra, and the temperatures and pressures in the reversing layers of stars. In: *Mon. Not. R. Astron. Soc.* 83 (1923), 403-424. http://articles.adsabs.harvard.edu/full/1923MNRAS..83..403F

[32] FOWLER, R. H. ; MILNE, E. A.: The maxima of absorption lines in stellar spectra (second paper). In: *Mon. Not. R. Astron. Soc.* 84 (1924), 499-515. http://articles.adsabs.harvard.edu/full/1924MNRAS..84..499F

[33] FRASER, M. ; LU, W. ; HAMIELEC, A. : Surface tension measurements on pure liquid iron and nickel by an oscillating drop technique. In: *Metall. Mater. Trans.* 2 (1971), 817-823. http://dx.doi.org/10.1007/BF02662741

[34] FRIE, W. : Zur Auswertung der Abelschen Integralgleichung. In: *Ann. Phys.* 465 (1963), 332-339. http://dx.doi.org/10.1002/andp.19634650510

[35] FUJII, H. ; MATSUMOTO, T. ; IZUTANI, S. : Surface tension of molten silicon measured by microgravity oscillating drop method and improved sessile drop method. In: *Acta Mater.* 54 (2006), 1221-1225. http://dx.doi.org/10.1016/j.actamat.2005.10.058

[36] GLORIEUX, B. ; MILLOT, F. ; RIFFLET, J. : Surface tension of liquid alumina from contactless techniques. In: *Int. J. Thermophys.* 23 (2002), 1249-1257. http://dx.doi.org/10.1023/A:1019848405502

[37] GLORIEUX, B. ; SABOUNGI, M. ; MILLOT, F. ; ENDERBY, J. ; RIFFLET, J.-C. : Aerodynamic levitation: an approach to microgravity. In: *AIP Conf. Proc.* 552 (2001), 316-324. http://dx.doi.org/10.1063/1.1357941

[38] GOLDSTON, R. ; RUTHERFORD, P. : *Introduction to Plasma Physics*. IOP Publishing Ltd, 1995

[39] GOLUBOVSKII, Y. ; GORCHAKOV, S. ; LOFFHAGEN, D. ; UHRLANDT, D. : Influence of the resonance radiation transport on plasma parameters. In: *Eur. Phys. J.: Appl. Phys.* 37 (2007), 101-104. http://dx.doi.org/10.1051/epjap:2006150

[40] GORENFLO, R. ; KOVETZ, Y. : Solution of an Abel-type integral equation in the presence of noise by quadratic programming. In: *Numer. Math.* 8 (1966), 392-406. http://dx.doi.org/10.1007/BF02162982

[41] GREGORI, G. ; SCHEIN, J. ; SCHWENDINGER, P. ; KORTSHAGEN, U. ; HEBERLEIN, J. ; PFENDER, E. : Thomson scattering measurements in atmospheric plasma

jets. In: *Phys. Rev. E* 59 (1999), 2286-2291. http://dx.doi.org/10.1103/PhysRevE.59.2286

[42] GRIEM, H. R.: *Principles of Plasma Spectroscopy* . Cambridge University Press, 1997

[43] HARVEY-THOMPSON, A. : Velocity and temperature measurements of Z pinch plasmas using optical Thomson scattering. In: *2011 Abstracts IEEE Int. Conf. on Plasma Science (ICOPS)*

[44] HAUMESSER, P. ; BANCILLON, J. ; DANIEL, M. ; PEREZ, M. ; GARANDET, J.-P. : High-temperature contactless viscosity measurements by the gas-film levitation technique: application to oxide and metallic glasses. In: *Rev. Sci. Instrum.* 73 (2002), 3275-3285. http://dx.doi.org/10.1063/1.1499756

[45] HIBIYA, T. ; K, K. M. ; OZAWA, S. : Oxygen partial pressure dependence of surface tension and its temperature coefficient for metallic melts: a discussion from the viewpoint of solubility and adsorption of oxygen. In: *J. Mater. Sci.* 45 (2010), 1986-1992. http://dx.doi.org/10.1007/s10853-009-4107-2

[46] HIGUCHI, K. ; FECHT, H. ; WUNDERLICH, R. : Surface tension and viscosity of the Ni-based superalloy CMSX-4 measured by the oscillating drop method in parabolic flight experiments. In: *Adv. Eng. Mater.* 9 (2007), 349-354. http://dx.doi.org/10.1002/adem.200600277

[47] HLÍNA, J. ; ŠONSKÝ, J. : Time-resolved tomographic measurements of temperatures in a thermal plasma jet. In: *J. Phys. D: Appl. Phys.* 43 (2010), 055202. http://dx.doi.org/10.1088/0022-3727/43/5/055202

[48] HOLT, R. ; TIAN, Y. ; JANKOVSKY, J. ; APFEL, R. : Surface-controlled drop oscillations in space. In: *J. Acoust. Soc. Am.* 102 (1997), 3802-3805. http://dx.doi.org/10.1121/1.420405

[49] HSU, K. ; ETEMADI, K. ; PFENDER, E. : Study of the free-burning high-intensity argon arc. In: *J. Appl. Phys.* 54 (1983), 1293-1301. http://dx.doi.org/10.1063/1.332195

[50] HUDDLESTONE, R. ; LEONARD, S. : *Plasma diagnostic techniques*. New York : Academic Press, 1965

[51] HUTCHINSON, I. : Introduction to Plasma Physics. http://silas.psfc.mit.edu/introplasma/

[52] ISHIKAWA, T. ; PARADIS, P. ; ITAMI, T. ; YODA, S. : Non-contact thermophysical property measurements of refractory metals using an electrostatic levitator. In: *Meas. Sci. Technol.* 16 (2005), 443-451. http://stacks.iop.org/0957-0233/16/i=2/a=016

[53] KEENE, B. ; MILLS, K. ; KASAMA, A. ; MCLEAN, A. ; MILLER, W. : Comparison of surface tension measurements using the levitated droplet method. In: *Metall. Mater. Trans.* 17 (1986), 159-162. http://dx.doi.org/10.1007/BF02670828

[54] KINGERY, W. ; HUMENIK, M. : Surface tension at elevated temperatures: I. Furnace and method for use of the sessile drop method; surface tension of silicon, iron and nickel. In: *J. Phys. Chem.* 57 (1953), 359-363. http://dx.doi.org/10.1021/j150504a026

[55] KRAMIDA, A. ; RALCHENKO, Y. ; READER, J. ; TEAM, N. A.: *NIST Atomic Spectra Database (ver. 5.0)*. http://www.nist.gov/pml/data/asd.cfm. Version: 2012

[56] KREYE, W. ; HEMSKY, J. ; ANDREWS, M. : A simple numerical method for a modified Abel inversion in which the density can be approximated by elliptical symmetry. In: *J. Phys. D: Appl. Phys.* 26 (1993), 1836-1842. http://dx.doi.org/10.1088/0022-3727/26/11/003

[57] LAMB, H. : *Hydrodynamics, 6th ed.* New York : Dover, 1945

[58] LANDES, K. : Diagnostics in plasma spraying techniques. In: *Surf. Coat. Technol.* 201 (2006), 1948-1954. http://dx.doi.org/10.1016/j.surfcoat.2006.04.036

[59] LANGE, S. ; SIEBER, M. ; FORSTER, G. ; MARQUÉS-LÓPEZ, J.-L. ; SCHEIN, J. ; K"AHLER, C. : Velocity Diagnostics for Gas Velocity Distributions in Cold Gas and Plasma Spraying Using Non-Resonant Laser Scattering. In: *J. Therm. Spray Technol.* 20 (2011), 12-20. http://dx.doi.org/10.1007/s11666-010-9554-4

[60] LARENZ, R. : Über ein Verfahren zur Messung sehr hoher Temperaturen in nahezu durchlässigen Bogensäulen. In: *Z. Phys.* 129 (1951), 327-342. http://dx.doi.org/10.1007/BF01327487

[61] LENARD, P. : Ueber die Schwingungen fallender Tropfen. In: *Ann. Phys.* 266 (1887), 209-243. http://dx.doi.org/10.1002/andp.18872660202

[62] LOWKE, J. ; MORROW, R. ; HAIDAR, J. : A simplified unified theory of arcs and their electrodes. In: *J. Phys. D: Appl. Phys.* 30 (1997), 2033-2042. http://dx.doi.org/10.1088/0022-3727/30/14/011

[63] MA, S. ; GAO, H. ; WU, L. ; ZHENG, S. : Time and spatially resolved spectroscopic measurement of temperatures in a free-burning arc by monochromatic imaging. In: *Meas. Sci. Technol.* 19 (2008), 105602. http://dx.doi.org/10.1088/0957-0233/19/10/105602

[64] MA, S. ; GAO, H. ; ZHANG, G. ; WU, L. : A versatile analytical expression for the inverse abel transform applied to experimental data with noise. In: *Appl. Spectrosc.* 62 (2008), 701-707. http://dx.doi.org/10.1366/000370208784658084

[65] MARCO, F. ; SEGRE, S. : The polarization of an e.m. wave propagating in a plasma with magnetic shear. The measurement of poloidal magnetic field in a Tokamak. In: *Plasma Phys.* 14 (1972), 245-252. http://dx.doi.org/10.1088/0032-1028/14/3/002

[66] MARSTON, P. ; APFEL, R. : Acoustically forced shape oscillation of hydrocarbon drops levitated in water. In: *J. Colloid. Interface Sci.* 68 (1979), 280-286. http://dx.doi.org/10.1016/0021-9797(79)90281-9

[67] MATSUMOTO, T. ; FUJII, H. ; UEDA, T. ; KAMAI, M. ; NOGI, K. : Oscillating drop method using a falling droplet. In: *Rev. Sci. Instrum.* 75 (2004), 1219-1221. http://dx.doi.org/10.1063/1.1711149

[68] MATSUMOTO, T. ; FUJII, H. ; UEDA, T. ; KAMAI, M. ; NOGI, K. : Measurement of surface tension of molten copper using the free-fall oscillating drop method. In: *Meas.*

Sci. Technol. 16 (2005), 432-437. http://stacks.iop.org/0957-0233/16/i=2/a=014

[69] MEIDEN, H. van d.: Collective Thomson scattering for ion temperature and velocity measurements on Magnum-PSI: a feasibility study. In: *Plasma Phys. Control. Fusion* 52 (2010), 045009. http://dx.doi.org/10.1088/0741-3335/52/4/045009

[70] MILLOT, F. ; RIFFLET, J. ; WILLE, G. ; SAROU-KANIAN, V. ; GLORIEUX, B. : Analysis of surface tension from aerodynamic levitation of liquids. In: *J. Am. Ceram. Soc.* 85 (2002), 187-192. http://dx.doi.org/10.1111/j.1151-2916.2002.tb00064.x

[71] MORADIAN, A. ; MOSTAGHIMI, J. : Measurement of surface tension, viscosity, and density at high temperatures by free-fall drop oscillation. In: *Metall. Mater. Trans.* 39 (2008), 280-290. http://dx.doi.org/10.1007/s11663-007-9120-8

[72] MURPHY, A. : The effects of metal vapour in arc welding. In: *J. Phys. D: Appl. Phys.* 43 (2010), 434001. http://dx.doi.org/10.1088/0022-3727/43/43/434001

[73] MURPHY, A. ; TANAKA, M. ; TASHIRO, S. ; SATO, T. ; LOWKE, J. : A computational investigation of the effectiveness of different shielding gas mixtures for arc welding. In: *J. Phys. D: Appl. Phys.* 42 (2009), 115205. http://dx.doi.org/10.1088/0022-3727/42/11/115205

[74] NESTOR, O. : Intensity and Current Density Distributions at the Anode of High Current, Inert Gas Arcs. In: *J. Appl. Phys.* 33 (1962), 1638-1648. http://dx.doi.org/10.1063/1.1728803

[75] NICKEL, G. H.: Elementary derivation of the Saha equation. In: *Am. J. Phys* 48 (1980), 448-450. http://dx.doi.org/10.1119/1.12002

[76] NOÜY, P. du: An interfacial tensiometer for universal use. In: *J. Gen. Physiol.* 7 (1925), 625-631. http://dx.doi.org/10.1085/jgp.7.5.625

[77] OH, D.-S. ; KIM, Y.-S. ; CHO, S.-M. : Derivation of current density distribution by arc pressure measurement in GTA welding. In: *Sci. Technol. Weld. Joi.* 10 (2005), 442-446. http://dx.doi.org/10.1179/174329305X44116

[78] OLSEN, H. N.: The electric arc as a light source for quantitative spectroscopy. In: *J. Quant. Spectrosc. Radiat. Transfer* 3 (1963), 305-333. http://dx.doi.org/10.1016/0022-4073(63)90015-3

[79] OZAWA, S. ; SUZUKI, S. ; HIBIYA, T. ; FUKUYAMA, H. : Influence of oxygen partial pressure on surface tension and its temperature coefficient of molten iron. In: *J. Appl. Phys.* 109 (2011), 014902. http://dx.doi.org/10.1063/1.3527917

[80] PARADIS, P. ; ISHIKAWA, T. ; YODA, S. : Non-contact property measurements of liquid and supercooled ceramics with a hybrid electrostatic-aerodynamic levitation furnace. In: *Meas. Sci. Technol.* 16 (2005), 452-456. http://stacks.iop.org/0957-0233/16/i=2/a=017

[81] PARADIS, P. ; YU, J. ; ISHIKAWA, T. ; YODA, S. : Property measurements and so-

lidification studies by electrostatic levitation. In: *Ann. N.Y. Acad. Sci.* 1027 (2004), 464-473. http://dx.doi.org/10.1196/annals.1324.037

[82] PASSERONE, A. : Twenty years of surface tension measurements in space. In: *Microgravity Sci. Technol.* 23 (2011), 101-111. http://dx.doi.org/10.1007/s12217-010-9198-5

[83] PAUL, R. K.: Novel approach to Abel inversion. In: *Rev. Sci. Instrum.* 78 (2007), 093701 1-5. http://dx.doi.org/10.1063/1.2777159

[84] PELLERIN, S. ; MUSIOL, K. ; POKRZYWKA, B. ; CHAPELLE, J. : Stark width of $4p'\left[\frac{1}{2}\right] - 4s\left[\frac{3}{2}\right]^o$ Ar I transition (696.543 nm). In: *J. Phys. B: At. Mol. Phys.* 29 (1996), 3911-3924. http://stacks.iop.org/0953-4075/29/i=17/a=014

[85] PEREGRINE, D. ; SHOKER, G. ; SYMON, A. : The bifurcation of liquid bridges. In: *J. Fluid. Mech.* 212 (1990), 25-39. http://dx.doi.org/10.1017/S0022112090001835

[86] PROSPERETTI, A. : Free oscillations of drops and bubbles: the initial-value problem. In: *J. Fluid. Mech.* 100 (1980), 333-347. http://dx.doi.org/10.1017/S0022112080001188

[87] RAYLEIGH: On the capillary phenomena of jets. In: *Proc. R. Soc. Lond.* 29 (1879), 71-97. http://dx.doi.org/10.1098/rspl.1879.0015

[88] ROUFFET, M. ; CRESSAULT, Y. ; GLEIZES, A. ; HLINA, J. : Thermal plasma diagnostic methods based on the analysis of large spectral regions of plasma radiation. In: *J. Phys. D: Appl. Phys.* 41 (2008), 125204. http://dx.doi.org/10.1088/0022-3727/41/12/125204

[89] ROUFFET, M. ; WENDT, M. ; GOETT, G. ; KOZAKOV, R. ; SCHOEPP, H. ; WELTMANN, K. ; UHRLANDT, D. : Spectroscopic investigation of the high-current phase of a pulsed GMAW process. In: *J. Phys. D: Appl. Phys.* 43 (2010), 434003. http://stacks.iop.org/0022-3727/43/i=43/a=434003

[90] SAUERWALD, F. ; SCHMIDT, B. ; PELKA, F. : Die Oberflächenspannung geschmolzener Metalle und Legierungen. V. Die Oberflächenspannung von Fe-C-Legierungen, $Hg_5Tl_2NaHg_2$, ihre zeitliche Veränderung bei Thallium und die Oberflächenspannung von Schlacken. In: *Z. Anorg. Allg. Chem.* 223 (1935), 84-90. http://dx.doi.org/10.1002/zaac.19352230108

[91] SCHELLHASE, M. : *Der Schweisslichtbogen: Ein technologisches Werkzeug*. DVS Media, 1985

[92] SCHNICK, M. ; FUESSEL, U. ; HERTEL, M. ; HAESSLER, M. ; SPILLE-KOHOFF, A. ; MURPHY, A. : Modelling of gas-metal arc welding taking into account metal vapour. In: *J. Phys. D: Appl. Phys.* 43 (2010), 434008. http://dx.doi.org/10.1088/0022-3727/43/43/434008

[93] SHEN, W. ; DEXTER, R. ; PRAGER, S. : Current-density fluctuations and ambipolarity of transport. In: *Phys. Rev. Lett.* 68 (1992), 1319-1322. http://dx.doi.org/10.1103/PhysRevLett.68.1319

[94] SHKAROFSKY, I. : Evaluation of multipole moments over the current density in a

tokamak with magnetic probes. In: *Phys. Fluids* 25 (1982), 89-96. http://dx.doi.org/10.1063/1.863632

[95] SNYDER, S. ; REYNOLDS, L. ; FINCKE, J. ; LASSAHN, G. ; GRANDY, J. ; REPETTI, T. : Electron-temperature and electron-density profiles in an atmospheric-pressure argon plasma jet. In: *Phys. Rev. E* 50 (1994), 519-525. http://dx.doi.org/10.1103/PhysRevE.50.519

[96] SOLTWISCH, H. : Current density measurements in Tokamak devices. In: *Plasma Phys. Control. Fusion* 34 (1992), 1669-1698. http://dx.doi.org/10.1088/0741-3335/34/12/001

[97] SPITZER, L. ; HÄRM, R. : Transport Phenomena in a Completely Ionized Gas. In: *Phys. Rev.* 89 (1953), 977-981. http://dx.doi.org/10.1103/PhysRev.89.977

[98] SUBRAMANIAM, S. ; WHITE, D. : Effect of shield gas composition on surface tension of steel droplets in a gas-metal-arc welding arc. In: *Metall. Mater. Trans.* 32 (2001), 313-318. http://dx.doi.org/10.1007/s11663-001-0054-2

[99] SUBRAMANIAM, S. ; WHITE, D. ; SCHOLL, D. ; WEBER, W. : In situ optical measurement of liquid drop surface tension in gas metal arc welding. In: *J. Phys. D: Appl. Phys.* 31 (1998), 1963-1967. http://stacks.iop.org/0022-3727/31/i=16/a=004

[100] TANAKA, M. ; SAWATO, H. ; TASHIRO, S. ; NAKATA, K. ; YAMAMOTO, E. ; YAMAZAKI, K. ; SUZUKI, K. : Measurements and Visualizations of 2D Temperature of Arc Plasma from a Monochromator with High-speed Video Camera. In: *IIW Singapore 2009* IIW Doc.212- 1145-09 (2009)

[101] TON, H. : Physical properties of the plasma-MIG welding arc. In: *J. Phys. D: Appl. Phys.* 8 (1975), 922-933. http://dx.doi.org/10.1088/0022-3727/8/8/006

[102] WENDT, M. : Net emission coefficients of argon iron plasmas with electron Stark widths scaled to experiments. In: *J. Phys. D: Appl. Phys.* 44 (2011), 125201. http://dx.doi.org/10.1088/0022-3727/44/12/125201

[103] WIESE, W. : Spectroscopic diagnostics of low temperature plasmas: techniques and required data. In: *Spectrochim. Acta B* 46B (1991), 831-841. http://dx.doi.org/10.1016/0584-8547(91)80084-G

[104] WILLE, G. ; MILLOT, F. ; RIFFELT, J. : Thermophysical properties of containerless liquid iron up to 2500 K. In: *Int. J. Thermophys.* 23 (2002), 1197-1206. http://dx.doi.org/10.1023/A:1019888119614

[105] ZELDOVICH, Y. ; RAIZER, Y. : *Physics of Shock Waves and High-Temperature Hydrodynamic Phenomena*. New York : Academic Press, 2002

[106] ZHANG, G. ; XIONG, J. ; HU, Y. : Spectroscopic diagnostics of temperatures for a non-axisymmetric coupling arc by monochromatic imaging. In: *Meas. Sci. Technol.* 21 (2010), 105502. http://dx.doi.org/10.1088/0957-0233/21/10/105502

[107] ZIELIŃSKA, S. ; MUSIOŁ, K. ; DZIERŻĘGA, K. ; PELLERIN, S. ; VALENSI, F. ; IZARRA, C. de ; BRIAND, F. : Investigations of GMAW plasma by optical emission spectroscopy. In: *Plasma Sources Sci. Technol.* 16 (2007), 832-838. http://stacks.iop.org/0963-0252/16/i=4/a=019